Karlsruher Institut für Technologie

Strongly Interacting Dark Sectors in the Early Universe and at the LHC

Zur Erlangung des akademischen Grades eines

DOKTORS DER NATURWISSENSCHAFTEN (DR. RER. NAT.)

von der KIT-Fakultät für Physik
des Karlsruher Instituts für Technologie (KIT)

genehmigte

DISSERTATION

von

M.Sc. Nicoline Krogh Hemme

aus Denmark

Referent: Felix Kahlhoefer

Korreferent: Michael Kraemer

Tag der mündlichen Prüfung: 07. November 2025

Eidesstattliche Versicherung gemäß § 13 Absatz 2 Ziffer 3 der Promotionsordnung des Karlsruher Instituts für Technologie (KIT) für die KIT-Fakultät für Physik:

1. Bei der eingereichten Dissertation zu dem Thema

   Strongly Interacting Dark Sector in the Early Universe and at the LHC

   handelt es sich um meine eigenständig erbrachte Leistung.

2. Ich habe nur die angegebenen Quellen und Hilfsmittel benutzt und mich keiner unzulässigen Hilfe Dritter bedient. Insbesondere habe ich wörtlich oder sinngemäß aus anderen Werken übernommene Inhalte als solche kenntlich gemacht.

3. Die Arbeit oder Teile davon habe ich bislang nicht an einer Hochschule des In- oder Auslands als Bestandteil einer Prüfungs- oder Qualifikationsleistung vorgelegt.

4. Die Richtigkeit der vorstehenden Erklärungen bestätige ich.

5. Die Bedeutung der eidesstattlichen Versicherung und die strafrechtlichen Folgen einer unrichtigen oder unvollständigen eidesstattlichen Versicherung sind mir bekannt.

Ich versichere an Eides statt, dass ich nach bestem Wissen die reine Wahrheit erklärt und nichts verschwiegen habe.

Karlsruhe, den 27. November 2025

. . . . . .

(Nicoline Krogh Hemme)

Abstract

Our understanding of the Universe, its fundamental constituents and its evolution, has significantly advanced over the past century. Nonetheless, big mysteries remain unsolved. One of the most pressing questions in modern physics is the nature of dark matter. Despite compelling evidence from astrophysical and cosmological observations, and extensive experimental efforts to detect it, the nature of dark matter continues to elude us. This has sparked interest in a plethora of new theoretical models, exploring new particles with distinct phenomena that could have evaded detection thus far. In this thesis, we dive into a class of such models, where dark matter resides in a confined hidden sector with feeble interactions with the Standard Model. Specifically, we study an $SU(N_{c_D})$ gauge theory with N_{f_D} light dark quarks. At low energies, this theory confines, giving rise to a spectrum of dark mesons. Among these, the two lightest - dark pions and dark rho mesons - play a central role. The dark pion can be stable, making it a compelling dark matter candidate. Meanwhile, a relatively light dark rho meson significantly influences the model's dark matter phenomenology through two key mechanisms. First, the light dark rho meson opens up the $3\pi_D \to \pi_D\rho_D$ annihilation process, which we find to be the dominant process setting the dark matter relic abundance. This favors dark pion masses on the order of a few hundred MeV, while ensuring that self-interaction strengths remain below the upper limits imposed by Bullet Cluster constraints. Second, the dark rho meson becomes kinematically unable to decay within the dark sector. If feeble interactions with the Standard Model exist, it can decay into visible particles with a significant lifetime. The latter leads to new distinct experimental signatures, such as dark showers and displaced vertices at accelerator experiments. We project the sensitivity of current and future displaced vertex searches, such as at the NA62, SHiP and Belle II, to probe the parameter space of this model. Our findings suggest that a substantial portion of the parameter space, up to dark rho masses of a few GeV, could be explored in the near future. Finally, we consider more broadly the dark shower signatures at LHC collider experiments. As LHC is currently the highest energy collider, it is in many ways a prime candidate to search for new physics beyond the Standard Model. However, it is clear that this type of model is difficult to probe in traditional searches at the LHC. An example of this is the dark shower event known as semi-visible jets, which is characterised by large missing energy aligned closely with a Standard Model jet. Such an event is typically expected to arise due to misreconstructed jets, and hence any signal of this type is usually discarded. Dedicated dark sector searches, which may record such types of events, are very few, and often unsatisfactory in their theoretical treatment of the model. We therefore highlight the need for reinterpreting LHC searches, that will help us probe even more of the parameter space of these types of models. While many searches look for new physics in general, and may not focus on whether they include a viable dark matter candidate, this aspect is essential when aiming to discover dark matter. Consequently, models that do offer such relic density targets, like the one examined in this thesis, are particularly compelling in this context. They hold significant promise for either discovery or placing meaningful constraints through upcoming experimental efforts.

Zusammenfassung

Unser Verständnis des Universums - seiner fundamentalen Bestandteile und seiner Entwicklung - hat sich im vergangenen Jahrhundert erheblich weiterentwickelt. Dennoch bleiben große Rätsel ungelöst. Eine der drängendsten Fragen der modernen Physik ist die Natur der Dunklen Materie. Trotz überzeugender Hinweise aus astrophysikalischen und kosmologischen Beobachtungen sowie umfangreicher experimenteller Bemühungen, sie direkt nachzuweisen, bleibt die wahre Natur der Dunklen Materie weiterhin unbekannt. Diese Unsicherheit hat das Interesse an einer Vielzahl neuer theoretischer Modelle geweckt, die neue Teilchen mit besonderen Eigenschaften untersuchen, die bisher der Detektion entgangen sein könnten. In dieser Arbeit widmen wir uns einer Klasse solcher Modelle, in denen die Dunkle Materie in einem abgeschlossenen, verborgenen Sektor existiert, der nur schwach mit dem Standardmodell wechselwirkt. Konkret untersuchen wir eine $SU(N_{c_D})$ Eichfeldtheorie mit N_{f_D} leichten dunklen Quarks. Bei niedrigen Energien führt diese Theorie zur Confinement und damit zur Entstehung eines Spektrums dunkler Mesonen. Die beiden leichtesten unter ihnen - dunkle Pionen und dunkle Rho-Mesonen - spielen eine zentrale Rolle. Das dunkle Pion kann stabil sein und stellt somit einen vielversprechenden Kandidaten für Dunkle Materie dar. Gleichzeitig beeinflusst ein relativ leichtes dunkles Rho-Meson die Phänomenologie der Dunklen Materie in diesem Modell auf zwei entscheidende Arten. Erstens ermöglicht das leichte dunkle Rho-Meson den Annihilationsprozess $3\pi_D \to \pi_D\rho_D$, den wir als dominanten Mechanismus zur Festlegung der Reliktdichte der Dunklen Materie identifizieren. Dies bevorzugt dunkle Pionenmassen in der Größenordnung von einigen hundert MeV, wobei die Stärke der Selbstwechselwirkungen unterhalb der durch Beobachtungen des Bullet Clusters gesetzten Obergrenze bleibt. Zweitens kann das dunkle Rho-Meson kinematisch nicht mehr innerhalb des dunklen Sektors zerfallen. Falls schwache Wechselwirkungen mit dem Standardmodell existieren, kann es mit einer signifikanten Lebensdauer in sichtbare Teilchen zerfallen. Dies führt zu neuen, charakteristischen experimentellen Signaturen, wie dunklen Schauern und Displaced Vertices in Beschleunigerexperimenten. Wir untersuchen die Sensitivität aktueller und zukünftiger Suchen nach Displaced Vertices - etwa bei NA62, SHiP und Belle II - zur Erkundung des Parameterraums dieses Modells. Unsere Ergebnisse zeigen, dass ein beträchtlicher Teil des Parameterraums bis zu dunklen Rho-Massen von einigen GeV in naher Zukunft zugänglich sein könnte. Abschließend betrachten wir die Signaturen dunkler Schauern in Experimenten am LHC. Da der LHC derzeit der Teilchenbeschleuniger mit der höchsten Energie ist, bietet er in vielerlei Hinsicht eine hervorragende Möglichkeit, nach neuer Physik jenseits des Standardmodells zu suchen. Allerdings ist klar, dass diese Art von Modell in traditionellen LHC-Suchen schwer zugänglich ist. Ein Beispiel dafür ist das sogenannte „Dark Shower"-Ereignis, bekannt als halb-sichtbare Jets, das sich durch viel fehlenden Transversalimpuls auszeichnet, die eng mit einem Jet des Standardmodells ausgerichtet ist. Solche Ereignisse werden typischerweise als Folge falsch rekonstruierter Jets interpretiert und daher meist verworfen. Spezielle Suchen im dunklen Sektor, die solche Ereignisse erfassen könnten, sind sehr selten und oft unzureichend in ihrer theoretischen Behandlung des Modells. Daher betonen wir die Notwendigkeit, LHC-Suchen neu zu interpretieren, um einen größeren Teil des Parameterraums dieser Modelle untersuchen zu können. Während viele Suchen allgemein nach neuer Physik Ausschau halten und nicht unbedingt darauf achten, ob ein Modell einen geeigneten Kandidaten für dunkle Materie enthält, ist dieser Aspekt entscheidend, wenn es darum geht, dunkle Materie zu entdecken. Modelle, die solche Kandidaten mit korrekter Reliktdichte beinhalten - wie das in dieser Arbeit untersuchte - sind in diesem Zusammenhang besonders vielversprechend. Sie bieten großes Potenzial für Entdeckungen oder für das Setzen bedeutender Einschränkungen durch zukünftige Experimente.

List of Publications

I here list the published and currently unpublished works that form the basis of this thesis, and note my contributions to each of them.

- *Dark matter relic density in strongly interacting dark sectors with light vector mesons* [1]. This paper was done in collaboration with Elias Bernreuther, Felix Kahlhoefer and Suchita Kulkarni. The work makes up the core of Chapter 5. I derived the Boltzmann equation for the novel interaction $3\pi_D \to \pi_D \rho_D$, and developed the numerical code to solve the Boltzmann equation across all relevant processes. I carried out the relic density calculations and established constraints on both the kinetic mixing and the self-interaction cross section. Additionally, I generated the plots featured in the publication. I contributed to discussions of the theoretical model and how to handle the fundamental parameters. I contributed to writing the paper, with a focus on the sections describing the Boltzmann equation, the relic density calculations and the results.

- *Sub-GeV dark matter and multi-decay signatures from dark showers at beam-dump experiments* [2]. This paper was written in collaboration with Elias Bernreuther, Felix Kahlhoefer, Suchita Kulkarni and Maksym Ovchynnikov. The work makes up the core of Chapter 6. I developed and validated the rescaling procedure to extend the Pythia 8 Hidden Valley module to lower masses. I performed many additional tests and validations of our parameter choices, both in Pythia 8 and MadGraph. I also generated the Monte Carlo events used in this analysis, and contributed to cross-checks and collaborative discussions that lead to the final results. I contributed to the paper with several plots as well as writing a section on the model set up and details on the Monte Carlo simulations.

- *Reinterpreting LHC data for dark shower searches* (work in progress). This paper is being done in collaboration with Felix Kahlhoefer, Benjamin Fuks, Mark Goodsell, Sukanya Sinha, Thomas Wojtkowski and Marie-Helene Genest. The work makes up the core of Chapter 7. My contribution to this work is focused on reinterpreting the CMS-EXO-19-020 analysis. I have been in touch with the CMS collaboration to understand the details of their analysis, performed Monte Carlo simulations of the signal model, and implemented the analysis in MadAnalysis 5. I have also performed a thorough validation of the implementation, which has shown great agreement with the official CMS results. This analysis will be one of five that will be recasted in the paper. The paper will study a consistent model of dark showers, following the work of Ref. [3]. My contribution to the writing of the paper will focus on the section describing the CMS-EXO-19-020 analysis and the recasting of it in MadAnalysis 5.

Preface

This thesis is based on research that I have done during my doctoral studies at Karlsruhe Institute of Technology (KIT). I would like to gratefully acknowledge the following contributions from collaborators that have been integrated into this work:

- The FeynCalc calculations of the matrix element in Chapter 5 were performed by Elias Bernreuther.
- The analysis of the proposed Belle II search in Chapter 6 was performed by Elias Bernreuther.
- The `SensCalc`/`EventCalc` calculations in Chapter 6 was performed by Maksym Ovchynnikov, also including the dark-photon-like production probabilities.
- The statistical procedure of the CMS-EXO-19-020 analysis in Chapter 7 was coded by Felix Kahlhoefer.

I also want to acknowledge:

- The CRC TRR 257 "Particle Physics Phenomenology after the Higgs Discovery" for funding my PhD position, and for providing an exciting research environment.
- The CMS collaboration for providing the necessary information to validate my recasting of the CMS-EXO-19-020 analysis in Chapter 7.
- The use of generative AI tools, specifically ChatGPT, to assist in improving the language and grammar of this thesis. I have used these tools responsibly and critically, ensuring that the final content reflects my own understanding and voice.

Acknowledgements

I would like to express my sincere gratitude to everyone who has supported me throughout my PhD journey. In particular, I would like to state my thanks to some people that have meant a lot to me during this time.

I want to thank my supervisor, Felix Kahlhoefer, for his invaluable guidance. There is no doubt that I have been exceptionally fortunate to work with such a talented researcher and group leader. As I began my PhD journey, I also began a life in a place that was entirely new to me. Felix has been incredibly supportive and understanding throughout this transition, and his patience gave me an opportunity to find my place here. I also greatly appreciate the opportunities he has offered me to work with wonderful collaborators and to attend interesting conferences and workshops. His encouragement and guidance inspired me and gave me confidence in my work and abilites, and that is a sign of a truly great mentor.

I also want to thank my supervisor, Michael Krämer, for his support and encouragement.

Suchita Kulkarni and Elias Bernreuther have been two of my closest collaborators throughout my PhD. I am very grateful for their support and encouragement. They are both incredibly talented researchers, and I have learned a lot from them. I have always felt comfortable asking them questions, and they have always been willing to help me. In particular, it has been amazing to continue working with Suchita, who was my master thesis supervisor. I am very grateful for her continued support and guidance throughout my PhD, and wish her all the best in her future career and life.

Thank you to Tim Kretz for proofreading parts of this thesis, and for always being ready to help me with physics problems, and providing good jokes and encouragement. I also want to thank him, Maksym Riabokon and Sowmiya Balan for being great office mates.

I am eternally grateful for my once colleagues and now close friends Sowmiya Balan and Kierthika Chathirathas. My PhD journey would not have been the same without them. Especially the last two years have flown by due to the friendship we have built, and all the laughter and fun we have had together. And of course, I also thank you for the many intellectual discussions we've had...

Tak til min mor og far for jeres støtte gennem hele min uddannelse. Mor, tak fordi du har givet mig så meget af din tid og har skabt mange gode minder med mig hernede. Far, tak fordi du altid er klar på telefonen når jeg har brug for dig. Jeg er evigt taknemmelig for jeres kærlighed, og jeg ville ikke være her uden jer.

Finally, I want to thank my partner, Daesung Cho, for his unwavering support and encouragement throughout my PhD journey. As we have gone through similar journeys, side by side, he has inspired me and given me strength. His inputs and perspectives have made me a better researcher and person.

Contents

CHAPTER 1

Introduction

Science at its core is about devoloping hypotheses and testing them against experimental data. From a hypothesis, predictions of the outcomes of experiments can be made. If the predictions agree with the experimental data, the hypothesis is supported, and if not, it is rejected or revised. This is the scientific method. Though it is generally not possible to prove a theory with full certainty, it is often easy to disprove or constrain it if any experiment yields results that contradict the predictions of the theory. Scientific certainty is best approximated by continuously testing the theory against experimental data with ever more precise measurements.

A textbook example of this scientific method is the development of the Standard Model of particle physics. The theory provides a remarkably accurate description of the fundamental particles and their interactions, encapsulating the electromagnetic, weak, and strong forces within a quantum field theory framework. It has been tested and supported through numerous experiments, leading to a high degree of confidence in its predictions. However, it is not without its limitations, as it does not account for all observed phenomena in the Universe.

In this thesis, I will explore one of the most glaring missing pieces of the Standard Model: the existence of dark matter. Despite it being a cornerstone of modern cosmology, dark matter remains elusive, with no direct detection yet achieved. It is well known that dark matter makes up 25% of the universe's energy content, while ordinary matter, explained by the Standard Model, accounts for only 5%. The properties of dark matter are not well known, and to date it has only been indirectly observed through its gravitational effects on visible matter, radiation, and the large-scale structure of the universe.

In the Chapter 2, I will provide an overview of the Standard Model, including its fundamental particles and forces, and discuss its successes and limitations. I will then introduce dark matter and its significance in cosmology in Chapter 3. I will review the current state of dark matter research, including some popular candidates proposed to explain its properties and the ongoing efforts to detect it. Chapter 4 will introduce and elaborate on the theory of a strongly interacting dark sector; a candidate of dark matter that exhibits exciting physics and discovery potential. The phenomenology, cosmological consequences and experimental signatures of this theory will then be explored and studied in Chapters 5-7. Finally, I will conclude with a summary of the findings and their implications for our understanding of dark matter and the universe as a whole in Chapter 8.

CHAPTER 2

The Standard Model

The Standard Model (SM) of particle physics stands as one of the most successful and rigorously tested theories in modern science. It provides a comprehensive framework for understanding the fundamental constituents of matter and the forces that govern their interactions, excluding only gravity. Developed over the latter half of the 20th century, the SM has been validated through countless experiments and observations, making it a cornerstone of contemporary physics.

One of the most remarkable achievements of the SM is its predictive power. It has accurately predicted the existence and properties of particles long before their experimental discovery, the most famous example being the Higgs boson [4, 5]. Additionally, precision measurements at particle colliders have consistently validated the SM's predictions to an extraordinary degree [6, 7], with no significant deviations observed thus far.

In the Section 2.1 we will give an introduction to the SM using a quantum field theoretical perspective. We will discuss the fundamental particles and forces described by the SM, their interactions, and the symmetries that govern them. We will then discuss the low-energy effective field theory known as chiral perturbation theory in Section 2.2.

Despite its triumphs, the SM is not a complete theory of nature. It fails to account for several observed phenomena, and lacks explanations for certain fundamental questions. We will briefly discuss some of the limitations of the SM in Section 2.3.

2.1. Overview of Fundamental Particles and Forces

The Standard Model can be understood on several different levels. One approach is to consider the individual known particles and their properties, as illustrated in Figure 2.1. Fermions are spin 1/2 particles that make up ordinary matter, while bosons are integer spin particles that mediate the forces. The Standard Model includes 6 flavors of quarks or 3 generations (u/d, c/s, t/b), as well as 3 generations of leptons that include both charged leptons and neutral leptons known as neutrinoes (e/ν_e, μ/ν_μ, τ/ν_τ), and the force carriers of three of the four fundamental forces: the electromagnetic force, the weak force, and the strong force.

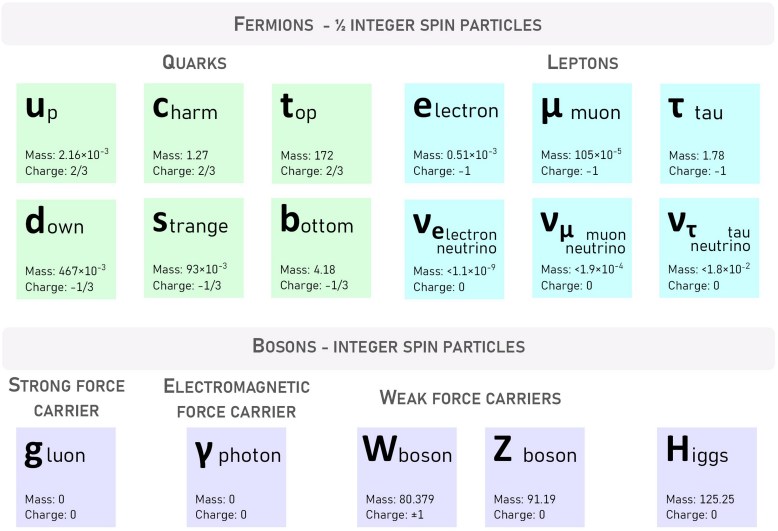

Figure 2.1.: Overview of SM particles and force carriers. The mass is given in units of GeV$\cdot c^2$ and charge is in units of electric charge.

On a more fundamental level, it can be understood using the framework of quantum field theory, where particles are described as matter fields and force carriers as gauge fields. The interactions between these fields are governed by a Lagrangian. The general form of the Standard Model Lagrangian is

$$\mathcal{L}_{SM} = -\frac{1}{4}F_{\mu\nu}F^{\mu\nu} + i\bar{\psi}\gamma^{\mu}D_{\mu}\psi + \bar{\psi}_i y_{ij}\psi_j\phi + \text{h.c.} + |D_{\mu}\phi|^2 - V(\phi) \tag{2.1}$$

where the $F^{\mu\nu}$ is the field strength tensor, D_μ is the covariant derivative, ψ represents the fermion fields, y_{ij} are the Yukawa couplings, and ϕ is the Higgs field and $V(\phi)$ is the Higgs potential. The notation of Equation 2.1 hides a lot of details, which become apparent when explicitly summing over the fields and gauge groups of the Standard Model. The terms involving the Higgs field and potential will not be discussed in detail here, but they are crucial for the generation of mass for the particles through the Higgs mechanism [8, 9].

The Lagrangian may be described through the symmetries under which it is invariant. The symmetries governing the Standard Model are $\mathrm{SU}(3) \times \mathrm{SU}(2) \times \mathrm{U}(1)$. The U(1) symmetry is associated with hypercharge Y, and is closely related to electromagnetic interactions. The SU(2) symmetry is associated with weak isospin I and is closely related to the weak interactions. However, at around ~ 246 GeV, the scale known as electroweak scale, the electromagnetic and weak interactions can no longer be considered as separate. Instead, we must consider them as part of a unified electroweak theory governed by the product of the gauge groups, namely the electroweak symmetry $\mathrm{SU}(2) \times \mathrm{U}(1)$. This symmetry is spontaneously broken by the Higgs mechanism down to the subgroup $\mathrm{U}(1)_{\mathrm{em}}$; the electromagnetic symmetry, leading to the notion of electric charge Q, given by the sum of the third component of the weak isospin and the hypercharge: $Q = T^3 + Y$. Importantly, this mechanism also leads to the identification of two charged massive vector bosons, $W^{\pm}$, two neutral vector bosons; one of which is massive, Z^0 and one is massless, γ, as well as the neutral Higgs boson, H. The interactions between charged leptons and the photon is described by $\mathrm{U}(1)_{\mathrm{em}}$, also known as Quantum Electrodynamics (QED). Weak theory successfully describes the low energy ($E \ll m_{W^{\pm}}$) interactions and decays of leptons mediated by the $W^{\pm}$ and Z^0 bosons.

The SU(3) symmetry is associated with color charge C, which is carried only by quarks and gluons. This theory is known as Quantum Chromodynamics (QCD). As QCD will be

particularly important throughout this work, we will take a closer look at this theory by introducing the QCD Lagrangian here:

$$\mathcal{L}_{QCD} = -\frac{1}{4} G^a_{\mu\nu} G^{\mu\nu}_a + \bar{q}(i\gamma^\mu D_\mu - M_q)q, \tag{2.2}$$

$$G^a_{\mu\nu} = \partial_\mu A^a_\nu - \partial_\nu A^a_\mu - \alpha_s f^{abc} A^b_\mu A^c_\nu, \tag{2.3}$$

$$D_\mu = \partial_\mu + i\alpha_s \frac{\lambda^a}{2} A^a_\mu, \tag{2.4}$$

where a runs from 1 to 8 and A^a_μ make up the 8 gluon fields of SU(3), q are the quark fields, M_q is the quark mass matrix, λ^a are the Gell-Mann matrices and α_s is the strong coupling constant. $G^a_{\mu\nu}$ is called the gluon field strength tensor and D_μ is the covariant derivative.

A crucial distinction to make when discussing the particles and interactions of the Standard Model is at what energy scale we want to make predictions. The Lagrangian in Equation 2.1 (as well as in Equation 2.2) contains terms that diverge at high energies, which has no physical meaning to us. To deal with this, the method of renormalization is used to absorb these infinities into redefinitions of the parameters, for example within the coupling constants.

However, an important consequence of this is that the coupling constants are no longer constant, but instead depend on the energy of the interactions. This is known as the running of the coupling constants and has been verified experimentally [10]. For the U(1), the coupling constant, known as the fine structure constant α, increase as we go towards higher energies (or shorter distances). This means that at low energies we can trust the perturbative expression, as written in the Lagrangian. In principle, there is then an energy scale at which the coupling constants diverge and the perturbative method breaks down. However, this scale is above the electroweak scale, and thus it is not physically relevant.

Returning to QCD, the consequences of the running coupling turn out to be of outmost importance. Unlike the previous case, the strong coupling decreases with increasing energy, a feature known as asymptotic freedom. This means that at high energies, the quarks and gluons can be treated as free particles, and we can trust the description in Equation 2.2. On the other end, at low energies, we find the phenomenon known as confinement. This occurs at energies below a scale called the QCD confinement scale, $\Lambda_{\text{QCD}} \sim 200 - 300$ MeV. Around Λ_{QCD}, the strong coupling constant diverges, at which point the fields entering the Lagrangian can no longer be treated perturbatively. What we observe at low energies is indeed not quarks or gluons, but composite objects made up of quarks and gluons, known as hadrons. Hadrons are always color-neutral, respecting the underlying SU(3) symmetry. The most well-known hadrons are the baryons, which are made up of three quarks of different colors, resulting in color-neutrality, and the mesons, which are made up of a quark and an antiquark. To describe the interactions of these hadrons, we need a low-energy effective field theory. In this work, we use chiral perturbation theory.

2.2. Chiral Perturbation Theory

Chiral perturbation theory (ChPT) is based on the concept of chiral symmetry of the QCD Lagrangian and the breaking thereof - both spontaneously and explicitly. To understand this, we must decompose the quark fields of the QCD Lagrangian in Equation 2.2 into left-handed and right-handed components, q_L, q_R, such that the quark part of the QCD Lagrangian can be written as [11]

$$\mathcal{L}_{\text{quark}} = i\bar{q}_L \bar{\sigma}^\mu D_\mu q_L + i\bar{q}_R \sigma^\mu D_\mu q_R - (\bar{q}_R M q_L + \bar{q_L} M q_R)\,, \tag{2.5}$$

where $\sigma^\mu = (1, \sigma^i)$ and $\bar{\sigma}^\mu = (1, -\sigma^i)$ and σ^i are the Pauli matrices. While quarks in the Standard Model are not massless, it is instructive to approximate them as massless and consider the above Lagrangian in this limit;

$$\mathcal{L}^0_{\text{quark}} = iq_L^\dagger \bar{\sigma}^\mu D_\mu q_L + iq_R^\dagger \sigma^\mu D_\mu q_R. \tag{2.6}$$

Without the mass term, the left-handed and right-handed components of the quark fields transform independently under the $\text{SU}(N_f)_L$ and $\text{SU}(N_f)_R$ subgroups of the $\text{SU}(N_f)$ gauge group, respectively. The transformations

$$q_L \to Lq_L, \quad q_R \to Rq_R, \tag{2.7}$$

with $L, R \in \text{SU}(N_f)$ being global chiral transformations, leave the Lagrangian in Equation 2.6 invariant. This is known as chiral symmetry. The global chiral symmetry group is $\text{SU}(N_f)_L \times \text{SU}(N_f)_R$.

2.2.1. Spontaneous Symmetry Breaking

Before moving on to the more realistic case of massive quarks, we mention an important phenomenon observed in QCD; the *quark condensate*[1]. The formation of the quark condensate means the composite quark fields $\bar{q}q$ acquire a non-zero vacuum expectation value (vev). These fields are defined as $q\bar{q} = \bar{q}_R q_L + \bar{q}_L q_R$, and thus a non-zero vev couples left- and right-handed quarks, such that they can no longer transform independently. The vev can be assigned a value, μ;

$$\langle \bar{q}q \rangle = \mu^3,$$

and it is known that μ^3 has the dimension of $[\text{mass}]^3$ as the quark fields have dimension corresponding to $[\text{mass}]^{\frac{3}{2}}$. Since the only dimensional parameter in the theory is the QCD confinement scale we expect $\mu \sim \Lambda_{QCD}$. An important consequence of the non-zero vacuum expectation value is that the quark condensate is not invariant under the chiral transformations, and therefore the chiral symmetry is spontaneously broken; $\text{SU}(N_f)_L \times \text{SU}(N_f)_R \to \text{SU}(N_f)_V$. Spontaneous symmetry breaking leads to the emergence of massless Goldstone bosons, as stated by Goldstone's theorem [15]. The number of broken generators is $N_f^2 - 1$, therefore according to Goldstone's theorem, we expect $N_f^2 - 1$ massless Goldstone bosons. We do not observe massless Goldstone bosons in nature, but we have not yet considered the effect of massive quarks.

2.2.2. Explicit Symmetry Breaking

The Standard Model has 6 flavors of quark, but we do not want to concern ourselves with all of these, as the heavier quarks are not expected to play a significant role in the low-energy dynamics. Since we are examining the energy regime below confinement, we can restrict ourselves to the quarks with mass $m_q \ll \Lambda_{QCD}$. This will give us $N_f = 2$ or $N_f = 3$, depending on whether we include the strange quark or not, which is lighter than the confinement scale but much heavier than the up and down quarks. For the time being, we will consider the case of $N_f = 2$, which is sufficient to illustrate the consequence of massive quarks on the chiral symmetry.

The quark masses break the chiral symmetry explicitly, as the mass term in the Lagrangian in Equation 2.5 is not invariant under the chiral transformations of Equation 2.7. However,

[1] The existence of the quark condensate is not yet fully understood from first principles, and can be put into question [12]. However, in the absence of the quark condensate, one would expect to observe double parity states. Such states have not been observed. Instead, the predictions based on the quark condensate match observations very well (see for example [13, 14]).

if we can assume that the masses are small (compared to Λ_{QCD}), the deviation from invariance is small, and the Lagrangian can be considered approximately invariant under the chiral transformations, and it is said that there is an approximate chiral symmetry. This approximate chiral symmetry is still broken spontaneously by the quark condensate, but now the Goldstone bosons acquire a small mass proportional to the quark masses and the quark condensate. These Goldstone bosons are referred to as pions, π. The Gell-Mann-Oakes-Renner relation [16] describes this relation and can be written as

$$m_\pi^2 = \frac{\mu^3}{f_\pi^2}(m_u + m_d), \tag{2.8}$$

where we have introduced the dimensional parameter $f_\pi \approx 92$ MeV, known as the pion decay constant. Three such light pions have been observed, and their masses have been experimentally verified to be $m_{\pi^0} \approx 135$ MeV, $m_{\pi^\pm} \approx 140$ MeV [10], consistent with the Gell-Mann-Oakes-Renner relation. The $0, \pm$ subscript refers to the electric charge of the pion, resulting from their respective quark content as the quarks carry electric charge.

If we reconsider the inclusion of the strange quark, i.e. $N_f = 3$, we expect $3^2 - 1 = 8$ Goldstone bosons. Indeed, we observe an additional 5 pseudoscalar mesons that are relatively light, namely the K^0, $\bar{K}^0$, K^+, K^- and η. Their masses are $m_{K^\pm} \approx 494$ MeV, $m_{K^0,\bar{K}^0} \approx 498$ MeV and $m_\eta \approx 548$ MeV. In contrast, we can consider another pseudoscalar meson, the η', which has similar quark content to the η, but is not a Goldstone boson. The η' is significantly heavier than the other pseudoscalar mesons, with a mass of $m_{\eta'} \approx 958$ MeV [10].

2.2.3. The Chiral Lagrangian

The pions, or generally the pseudo Goldstone bosons, can be parametrized as a matrix in the fundamental representation of $SU(2)$, which is given by

$$U(x) = \exp\left(2i\frac{\pi(x)}{f_\pi}\right) = \exp\left(2i\frac{\pi^a(x)\tau^a}{f_\pi}\right), \tag{2.9}$$

where τ^a are the generators of SU(2) and $\pi^a = \pi^1, \pi^2, \pi^3$ are the 3 pions.

Coming back to the objective of formulating a low-energy effective field theory for the confined regime, we can now write down a Lagrangian of the fields in Equation 2.9 that respects the chiral symmetry $\mathrm{SU}(2)_L \times \mathrm{SU}(2)_R$. Under the transformation, the pion fields transform as

$$U \to RUL^\dagger, \tag{2.10}$$

For low-energy dynamics, the most important terms in the Lagrangian are the ones with the lowest mass dimension. This is because higher mass dimension terms are suppressed by powers of E/Λ_{QCD}, where E is the energy scale of the process. Therefore, we can construct the Lagrangian as an expansion in terms of derivatives, $\partial_\mu U$, which have mass dimension 1. Terms with odd number of derivatives are not allowed as they would contain an odd number of Lorentz indices. The next term to consider is then the term with two derivatives, $\mathrm{tr}(\partial_\mu U \partial^\mu U^\dagger)$. This term is invariant under the chiral transformations:

$$\mathrm{tr}(\partial_\mu U \partial^\mu U^\dagger) \to \mathrm{tr}(R\partial_\mu U L^\dagger L \partial^\mu U^\dagger R^\dagger) = \mathrm{tr}(\partial_\mu U \partial^\mu U^\dagger). \tag{2.11}$$

Finally, we need to insert the mass term. If the mass term M transformed as a field as $M \to RML^\dagger$, we find that the term $MU^\dagger + UM^\dagger$ is invariant under the chiral transformations, if M is assumed to transform as $M \to RML^\dagger$. However, the mass term features the quark mass matrix ($M_q = \mathrm{diag}(m_u, m_d)$ for 2 lightest flavors, and $M_q = \mathrm{diag}(m_u, m_d, m_s)$ for 3

lightest flavors), which is a constant matrix and does not transform. This means that the mass term breaks the chiral symmetry explicitly.

We can further examine the mass term by expanding it in terms of the pion fields. The mass term of the Chiral Lagrangian is given by

$$\mathcal{L}_{\text{Ch}} \supset \tfrac{\mu^3}{2}\left[\text{Tr}\left(M_q U^\dagger\right) + \text{h.c.}\right], \tag{2.12}$$

where μ^3 is the quark condensate introduced in Section 2.2.1. The pion field U and the hermitian conjugate can be Taylor expanded to

$$U \simeq 1 + 2i\frac{\pi_D}{f_{\pi_D}} + \frac{1}{2}(2i\tfrac{\pi_D}{f_{\pi_D}})^2 + \tfrac{1}{6}(2i\tfrac{\pi_D}{f_{\pi_D}})^3 \tag{2.13}$$

$$U^\dagger \simeq 1 - 2i\tfrac{\pi_D}{f_{\pi_D}} + \tfrac{1}{2}(2i\tfrac{\pi_D}{f_{\pi_D}})^2 - \tfrac{1}{6}(2i\tfrac{\pi_D}{f_{\pi_D}})^3 \tag{2.14}$$

We expand the mass term to $\mathcal{O}(\pi^4)$, and we get that

$$\begin{aligned}\text{Tr}\left(M_q U^\dagger\right) =& \text{Tr}\left(M_q\left(1 - 2i\tfrac{\pi}{f_{\pi_D}} + \tfrac{1}{2}(2i\tfrac{\pi}{f_{\pi_D}})^2 - \tfrac{1}{6}(2i\tfrac{\pi}{f_{\pi_D}})^3 + \tfrac{1}{24}(2i\tfrac{\pi}{f_{\pi_D}})^4 + ...\right)\right)\\ =& \text{Tr}(M_q) - 2i\tfrac{1}{f_{\pi_D}}\text{Tr}(M_q\pi) - \tfrac{2}{f_{\pi_D}^2}\text{Tr}(M_q\pi^2) + \tfrac{4i}{3f_{\pi_D}^3}\text{Tr}(M_q\pi^3) + \tfrac{2}{3f_{\pi_D}^4}\text{Tr}(M_q\pi^4) + ...\end{aligned} \tag{2.15}$$

while the hermitian conjugate expands to

$$\begin{aligned}\text{Tr}\left(M_q U\right) =& \text{Tr}\left(M_q\left(1 + 2i\tfrac{\pi}{f_{\pi_D}} + \tfrac{1}{2}(2i\tfrac{\pi}{f_{\pi_D}})^2 + \tfrac{1}{6}(2i\tfrac{\pi}{f_{\pi_D}})^3 + \tfrac{1}{24}(2i\tfrac{\pi}{f_{\pi_D}})^4 + ...\right)\right)\\ =& \text{Tr}(M_q) + 2i\tfrac{1}{f_{\pi_D}}\text{Tr}(M_q\pi) - \tfrac{2}{f_{\pi_D}^2}\text{Tr}(M_q\pi^2) - \tfrac{4i}{3f_{\pi_D}^3}\text{Tr}(M_q\pi^3) + \tfrac{2}{3f_{\pi_D}^4}\text{Tr}(M_q\pi^4) + ...\end{aligned} \tag{2.16}$$

Adding these two expansions together, we find that the odd terms cancel out:

$$\text{Tr}\left(M_q U^\dagger\right) + \text{h.c.} = 2\text{Tr}(M_q) - \tfrac{4}{f_{\pi_D}^2}\text{Tr}(M_q\pi^2) + \tfrac{4}{3f_{\pi_D}^4}\text{Tr}(M_q\pi^4) + ... \tag{2.17}$$

The pion mass term is contained in the second term on the right-hand side of Equation 2.17, and we can take the quark mass matrix to be $M_q = \text{diag}(m_u, m_d)$ for $N_f = 2$. The term then becomes

$$\tfrac{2\mu^3}{f_{\pi_D}^2}\text{Tr}\left(M_q\pi^2\right) = \tfrac{2\mu^3}{f_{\pi_D}^2}(m_u + m_d)\text{Tr}(\pi^2). \tag{2.18}$$

We can identify the pion mass as

$$m_\pi^2 = \tfrac{2\mu^3}{f_{\pi_D}^2}(m_u + m_d) \tag{2.19}$$

To summarize, our final Lagrangian, the Chiral Lagrangian to leading order, is

$$\mathcal{L}_{\text{Ch}} = \frac{f_\pi^2}{4}\text{Tr}\left(\partial_\mu U \partial^\mu U^\dagger\right) + \left[\tfrac{\mu^3}{2}\text{Tr}\left(M_q U^\dagger\right) + \text{h.c.}\right]. \tag{2.20}$$

Let us briefly evaluate the validity of this chiral Lagrangian before continuing. We have only included terms of order $\mathcal{O}(p^2)$. These are the leading order terms, but a more accurate description would include derivative terms of arbitrarily high order, i.e. $\mathcal{O}(p^4)$, $\mathcal{O}(p^6)$ and so on. At low energies these contributions are suppressed by powers of E/f_π. Therefore, we naively expect the chiral Lagrangian to be valid at energies below f_π. More detailed studies of these corrections to the Langrangian through loop diagrams have been performed [17], and the scale at which the chiral perturbation theory breaks down, Λ_{CSB}, is found to be

$$\Lambda_{\text{CSB}} \sim 4\pi f_\pi \approx 1.2 \text{ GeV}.$$

2.2.4. Wess-Zumino-Witten term

In constructing a chiral effective theory, we require that the Lagrangian be invariant under chiral transformations. However, there's an important subtlety: while most terms in the effective Lagrangian are locally invariant under these transformations, there exist special terms that are not invariant at the level of the Lagrangian density, but whose integral over spacetime (i.e., the action) is invariant [18].

It was discovered by Wess, Zumino (1971) and Witten (1983) that such a term can be constructed for an $SU(3)_L \times SU(3)_R$ symmetry [19, 20], and hence, these terms are known as Wess-Zumino-Witten (WZW) terms. The WZW term is constructed in such a way that it respects the symmetry of the action, even though it may violate symmetry locally in the Lagrangian.

The WZW Lagrangian to leading order in the pion fields is given by [21]

$$\mathcal{L}_{\text{WZW}} = \frac{2N_C}{15\pi^2 f_\pi^5}\epsilon^{\mu\nu\rho\sigma}\text{Tr}\left(\pi\partial_\mu\pi\partial_\nu\pi\partial_\rho\pi\partial_\sigma\pi\right), \tag{2.21}$$

with a detailed derivation found in the literature such as [18–20]. The WZW term gives rise to a 5-point interaction between the pseudoscalar mesons, and critically, due to the fact that it is totally antisymmetric in the pseudoscalar fields, the term only exists for theories with at least 5 different pseudoscalar mesons, i.e. with $N_f \leq 3$.

2.3. Limitations of the Standard Model

Despite its successes, the SM is not a complete theory of fundamental particles and interactions, and it has numerous limitations in explaining certain phenomena.

Some of these limitations can be thought of as questions of naturalness [22]. For example, the hierarchy problem questions why the Higgs boson mass is so much lighter than the Planck scale, despite quantum corrections up to the Planck scale that should drive it to much higher values. The strong CP problem questions why the strong interaction does not appear to violate the combined symmetry of charge conjugation and parity, despite theoretical expectations that it should. The SM does not provide satisfactory answers to these questions.

Other limitations are more empirical in nature. These are rather glaring omissions in the SM that are known to exist based on observations and experimental tests. To answer these questions, we need to go beyond the SM. These questions include:

Gravity: The SM does not incorporate the force of gravity, which is described by Einstein's theory of General Relativity. Although the SM successfully describes three out of the four fundamental forces of nature, it lacks a quantum description of gravity. This is a major shortcoming, since gravity is a fundamental force - and, historically, it was the first force to be scientifically characterized. Gravity is the weakest of the four fundamental forces, but it is also the most long-range force and dominates the behavior of matter and energy on large scales. A quantum theory of gravity is desired to address several questions, most notably the unification of the four forces and the description of black hole thermodynamics [23]. Various approaches to quantum gravity have been proposed, such as string theory and loop quantum gravity, but a complete and consistent theory has yet to be developed.

Neutrino masses and mixing: The SM predicts that neutrinos are massless, but experiments have shown that they have non-zero - albeit small - masses, and that they can oscillate between different flavors. The SM does not provide a mechanism for generating neutrino masses, and the observed mixing angles are not explained [24]. Several mechanisms have

been proposed, such as the seesaw mechanism, which introduces heavy right-handed neutrinos that can generate small masses for the left-handed neutrinos through a mixing term [10]. Regardless of the specific mechanism, it is clear that the SM alone cannot account for neutrino masses and mixing.

Matter-antimatter asymmetry: The SM does not provide a satisfactory explanation for the observed matter-antimatter asymmetry in the universe. Sakharov's conditions [25] state that for a matter-antimatter asymmetry to arise, there must be baryon number violation, C and CP violation, and departure from thermal equilibrium. The SM does contain processes that violate baryon number, such as sphaleron processes, and it also contains CP violation in the quark sector through the complex phase in the CKM matrix [26]. However, the amount of CP violation in the SM is not sufficient to explain the observed matter-antimatter asymmetry. This suggests that there may be additional sources of CP violation beyond the SM.

Dark energy: Dark energy is an energy component of the Universe, making up about 68% of the total energy density [10]. This energy component has negative pressure, and is thought to be responsible for the accelerated expansion of the Universe. Dark energy is related to the cosmological constant that shows up in in Einstein's equations of General Relativity, representing the energy density of empty space. Not only is the size of the cosmological constant another problem of naturalness [22], recent observations suggest that it may not be a constant after all [27]. Either way, its origin and properties cannot be explained by the SM, and they remain a mystery.

Dark matter: An additional component of the Universe is dark matter, which makes up about 26% of the total energy density [10]. This is less than that of dark energy, but is ~ 6 times more abundant than the ordinary matter explained by the SM. The evidence for dark matter is robust, and it comes from a variety of astrophysical and cosmological observations, such as the rotation curves of galaxies, gravitational lensing, and the cosmic microwave background radiation. These observations suggest that there is a significant amount of matter in the Universe that does not interact with light or other forms of electromagnetic radiation, hence the name. The nature of dark matter is still unknown, but it is thought to be made up of particles that interact only feebly with ordinary matter, making them difficult to detect. However, with technological advancements - in the form of particle experiments with higher energies and detectors with higher sensitivities - we may be able to detect dark matter particles in the future. In addition to technological advancements, theoretical advancements in our understanding of particle physics and cosmology may also help us to identify the nature of dark matter. In particular, new theories may provide new candidates for dark matter, that can be tested experimentally today or in the near future.

In this thesis, we will focus on the question of dark matter.

CHAPTER 3

Beyond the Standard Model - Particle Dark Matter

Extremely little is known about dark matter, despite it's existence having been known since the 1930s [28, 29]. This is partially explained by the fact that the subject of dark matter was not widely studied until the 1970s and 1980s, when more robust evidence began to accumulate [30]. Nonetheless, significant progress has been made in the past few decades, with a multitude of independent observations across different scales and methods, all pointing to the existence of a non-luminous, non-baryonic matter component.

Here we briefly summarize what we *do know* about dark matter [10, 31]:

- It is abundant, constituting about 26% of the total energy content of the Universe.
- It is massive, with a lower bound on its mass being around $m_{\mathrm{b}} \gtrsim 10^{-22}$ eV for bosonic dark matter and $m_{\mathrm{f}} \gtrsim 70$ eV for fermionic dark matter.
- It is stable or with a lifetime longer than the age of the Universe.
- It is electrically neutral, or at least has a very small charge to mass ratio, specifically $3.5 \times 10^{-7} \left(\frac{m_{\mathrm{DM}}}{1\,\mathrm{GeV}}\right)^{0.58}$ for $m_{\mathrm{DM}} > 1\,\mathrm{GeV}$, and of $4.0 \times 10^{-7} \left(\frac{m_{\mathrm{DM}}}{1\,\mathrm{GeV}}\right)^{0.35}$ for $m_{\mathrm{DM}} < 1\,\mathrm{GeV}$.
- It may interact with photons if these interactions are highly suppressed. If dark matter does not carry electric charge, we can constrain it by $\sigma_{\mathrm{DM}-\gamma} \lesssim \mathcal{O}(10^{-33}) \left(\frac{m_{\mathrm{DM}}}{\mathrm{GeV}}\right) \mathrm{cm}^2$.
- Interaction with neutrinoes are non-existent or feeble; $\sigma_{\mathrm{DM}-\nu} \lesssim \mathcal{O}(10^{-32}) \left(\frac{m_{\mathrm{DM}}}{\mathrm{GeV}}\right) \mathrm{cm}^2$.
- If dark matter experiences self-interactions, these must be weak (more details in section 3.2).

In this chapter, we explore the theoretical and experimental landscape of particle dark matter, examining the observational evidence for its existence, some of the most popular candidate models beyond the SM, and the current status of searches and constraints across multiple detection strategies.

3.1. Evidence of dark matter

Multiple, independent pieces of evidence, from galactic to cosmological scales, indicate the presence of a non-luminous, non-baryonic matter component that interacts with the SM primarily, or exclusively, through gravity. Below we list some of the most compelling lines of evidence.

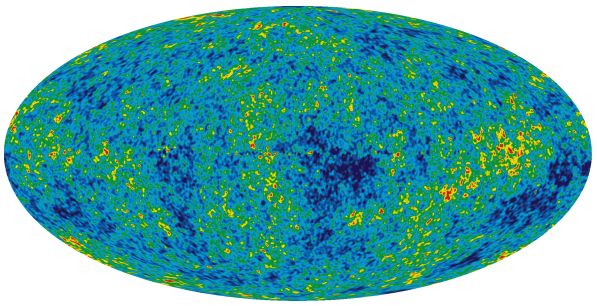

Figure 3.1.: The CMB temperature anisotropies as measured by the WMAP Data. The color scale indicates temperature fluctuations on linear scale from -200 to 200 μK. Credit: NASA/LAMBDA Archive Team [33].

3.1.1. CMB Anisotropies

The Cosmic Microwave Background (CMB) anisotropies provide some of the most compelling evidence for the existence of dark matter, and the most precise measurement of its abundance. The CMB represents a snapshot of the Universe at the time of recombination, when the temperature was approximately $T_{\mathrm{CMB}} = 0.3$ eV. At this epoch, free electrons and protons combined to form neutral hydrogen atoms. As the Universe continued to cool, photons no longer had sufficient energy to ionize hydrogen, allowing them to decouple from matter and travel freely through space.

Crucially, the Universe was not completely isotropic at this time; there were tiny fluctuations in the density and temperature of the matter and radiation on the order of $\delta(T_{\mathrm{CMB}}) \sim 10^{-5}$ [32]. Figure 3.1 shows a map of the CMB temperature anisotropies. These anisotropies have grown since then, and the inhomogeneity of density have served as the seeds for gravitational collapse, leading to the formation of the large-scale structure we observe today.

It turns out that the evolution of these anisotropies is incredibly sensitive to the total matter content of the Universe, including both baryonic and dark matter. Firstly, we expect that baryonic density perturbations grow linearly with the scale factor, $\delta_{\mathrm{baryon}} \propto a_0/a_{\mathrm{CMB}}$, which was about 10^3 times smaller at recombination than today. This means that the perturbations that were of order $\delta(T_{\mathrm{CMB}}) \sim 10^{-5}$ would be $\delta(T_0) \sim 10^{-2}$ today, which is insufficient to explain the formation of galaxies and clusters, for which we need $\delta(T_0) \gg 1$ [32]. This is where dark matter comes in. Since dark matter does not interact with photons, it can start to collapse and form gravitational wells much earlier than baryonic matter. This allows dark matter perturbations to grow significantly larger by the time of recombination, providing the necessary gravitational wells for baryonic matter to fall into after recombination and thus facilitating a more rapid growth of the density perturbations.

Another key aspect is that the presence of dark matter affects the acoustic oscillations in the baryon-photon plasma prior to recombination. The CMB power spectrum, which quantifies the probability that a sky patch of a given angular size maintains a uniform temperature, exhibits a series of acoustic peaks. The positions and heights of these peaks depend on factors such as the total matter density, the baryon density, and the dark matter density [31, 32]. Careful measurements of the CMB power spectrum by experiments such as WMAP and Planck allows inferring the matter content of the Universe with high precision. The results consistently indicate that about 85% of the total matter density is in the form of dark matter, with the remaining 15% being ordinary baryonic matter [10]. This is a key piece of evidence for the existence of dark matter.

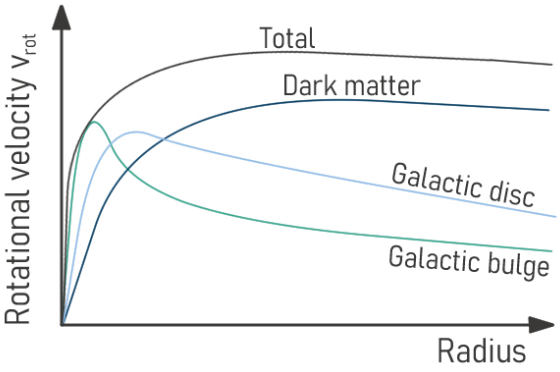

Figure 3.2.: Typical shape of the rotation curve of a spiral galaxy. The total rotation curve (black) corresponds to observations. The galactic disc and galactic bulge represent the visible matter, while the dark matter halo is inferred from the flat rotation curve at large radii. The total rotation curve (black) is the sum of the contributions from the visible and dark matter components. Adapted from Ref. [32].

3.1.2. Galaxy Rotation Curves

On galactic scales, flat rotation curves in spiral galaxies show rotational velocities remaining approximately constant well beyond the luminous stellar disk, implying extended mass distributions inconsistent with baryonic light profiles. This discovery was first made by Vera Rubin and Kent Ford in the 1970s [34], and has since been confirmed in numerous galaxies.

The rotation curve of a galaxy describes how the rotational velocity of stars and gas changes with distance from the galactic center. According to Newtonian mechanics and assuming spherical symmetry, the rotational velocity at a distance r from the center of a mass distribution $M(r)$ is given by

$$v_{\mathrm{rot}}(r) = \sqrt{\frac{GM(r)}{r}}, \tag{3.1}$$

where G is the gravitational constant. For a galaxy where most of the mass is concentrated in the luminous disk, we would expect the rotational velocity to decrease with distance in the outer regions of a galaxy, where the visible mass (stars, gas, dust) drops off. However, observations show that the rotation curves remain flat or even rise slightly at large radii, indicating that there is significantly more mass present than can be accounted for by the luminous matter alone [31]. An illustrative example is shown in Figure 3.2. This discrepancy suggests the presence of an extended halo of dark matter surrounding the galaxy, which provides the additional gravitational pull needed to maintain the observed rotational velocities.

The amount of dark matter inferred from rotation curves is typically several times the mass of the visible matter, leading to mass-to-light ratios that are much higher than what would be expected from baryonic matter alone. This has been observed in hundreds of spiral galaxies [31], and is one of the most direct pieces of evidence for the existence of dark matter [10].

3.1.3. Gravitational lensing

Gravitational lensing, the bending of light by mass, provides another powerful probe of dark matter. The bending of light is described by General Relativity, which predicts that light passing near a massive object will be deflected due to the curvature of spacetime caused by the mass [35]. The amount of deflection depends on the mass distribution of the lensing

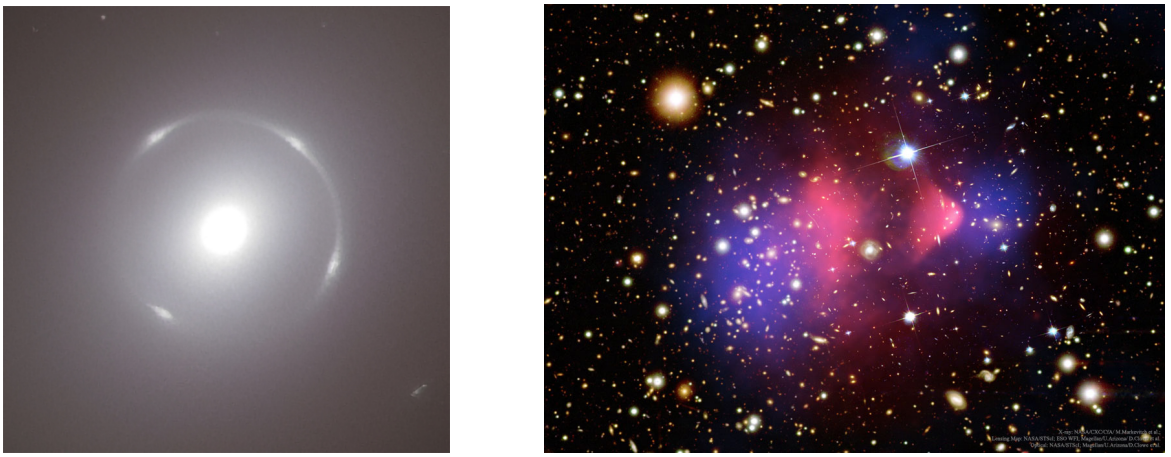

Figure 3.3.: Left: Einstein ring formed by the gravitational lensing of a distant galaxy by the foreground galaxy NGC 6505. Image captured by the Euclid space telescope. Credit: ESA/Euclid/Euclid Consortium/NASA, image processing by J.-C. Cuillandre, G. Anselmi, T. Li [36]. **Right:** Composite image of the Bullet Cluster (1E0657-558). The blue regions represent the total mass distribution as inferred from gravitational lensing, while the pink regions show hot, X-ray-emitting gas observed by the Chandra X-ray Observatory. Credit: NASA/CXC/M.Markevitch et al. [37].

object, and both strong and weak lensing observations reveal mass distributions that cannot be explained by visible matter alone.

Strong gravitational lensing occurs when a massive foreground object, such as a galaxy cluster, bends and magnifies the light from a more distant source like a background galaxy or quasar, producing distinctive features such as multiple images, arcs, or Einstein rings (see left panel of Figure 3.3). By analyzing the lensing geometry and distortions, we can reconstruct the mass distribution of the lensing object independently of its luminosity, revealing a total mass far exceeding what is visible - i.e. evidence for a substantial dark matter component [38]. Strong lensing constraints primarily apply to relatively small radii, limiting insights for the outer halo structure [39].

On the other hand, weak gravitational lensing involves subtle distortions in the shapes of background galaxies due to the gravitational influence of foreground mass distributions [39]. Through these distortions, we can statistically infer the mass distribution of large-scale structures, including galaxy clusters and even the cosmic web. Cosmic shear is the weak lensing effect caused by diffuse structures of matter outside galaxies and clusters, and observations predict a dark matter contribution consistent with CMB results [31].

Another example of weak lensing is provided by merging galaxy clusters, such as the Bullet Cluster, shown in the right panel of Figure 3.3. In this system, two galaxy clusters collided approximately 150 million years ago. If the mass were primarily baryonic matter, we would expect the mass distribution (blue in Figure 3.3) to closely follow the distribution of the X-rays emitted by hot gas (pink in Figure 3.3). However, through weak lensing measurements, we find that the majority of the mass is offset from the hot gas with the hot gas "lagging behind" the galaxies. If, on the other hand, the mass is dominated by dark matter, the galaxies can be approximated to be collisionless, and we now expect the galaxies to interact minimally during the collision, while the hot gas (which constitutes most of the baryonic mass) interacts strongly and slows down. This is indeed what we observe in the Bullet Cluster, and since then many other galaxy collision events [40]. The offset between the two indicates that most of the mass is collisionless and associated with dark matter, rather than baryonic matter.

3.2. Dark matter in cosmology

In the Big Bang Theory, which is the widely accepted theory to describe of the development of the Universe, the Universe began as a hot, dense state and has been expanding and cooling over time. The expansion of the Universe is described by the Friedmann equations and read [10]

$$H^2 \equiv \left(\frac{\dot{a}}{a}\right)^2 = \frac{8\pi G_N \rho}{3} - \frac{k}{a^2} + \frac{\Lambda}{3}, \tag{3.2}$$

and

$$\frac{\ddot{a}}{a} = \frac{\Lambda}{3} - \frac{4\pi G_N}{3}(\rho + 3p), \tag{3.3}$$

where $H(t) = \frac{\dot{a}(t)}{a(t)}$ is the Hubble parameter, a is the scale factor of the Universe, G_N is Newton's gravitational constant, ρ is the energy density of the Universe, k is the curvature parameter, Λ is the cosmological constant, and p is the pressure.

The scale factor $a(t)$ describes the scale of the Universe at time t and is usually set to $a_{t_0} = 1$ today (t_0), and at earlier times $a(t < t_0) < 1$. One of its roles in cosmology is to estimate how distances between objects in the Universe change over time. The scale factor is related to the redshift of light, z, from distant objects via $a = \frac{1}{1+z}$. Therefore, from the observed redshift of light from distant galaxies, we can infer the scale factor at the time the light was emitted. The fact that we observe redshifted light, i.e. $z > 0$, from distant galaxies [41][2] is one of the key pieces of evidence for the expansion of the Universe.

It is worth noting that the Hubble parameter is not constant over time, but rather changes as the Universe expands and cools down. In the early Universe, the expansion rate was much faster than it is today, and it has been slowing down over time. The current value of the Hubble parameter, known as the Hubble constant, is estimated to be around $H_0 \approx 67\text{km} \cdot \text{s}^{-1}\text{Mpc}^{-1}$, although there are ongoing debates about its value, as measurements have yielded different results with a disagreement at 5σ [42, 43]. This is known as the Hubble tension.

The Friedmann equations relate the expansion rate of the Universe to its energy content, including matter, radiation, dark matter and dark energy. The energy density of the Universe can be expressed in terms of the critical density, ρ_c, which is the energy density required for the Universe to be flat ($k = 0$), and this is given by

$$\rho_c = \frac{3H^2}{8\pi G_N}. \tag{3.4}$$

The density parameter, Ω, is defined as the ratio of the actual energy density to the critical density, i.e. $\Omega = \frac{\rho}{\rho_c}$. Current observations suggest that the Universe is very close to flat, with $\Omega_{\text{total}} \approx 1$ [10].

ΛCDM is the standard cosmological model, and posits that along with ordinary baryonic matter and radiation, the Universe is composed of dark energy, Λ, and cold dark matter (CDM), which means that dark matter was non-relativistic when structure formation began. The model has only 6 phenomelogical parameters, which determine the shape of the CMB power spectrum, and thus can be measured by CMB observations to percent-level accuracy [32]. These include the density parameters of the individual components of the Universe, which add up to ≈ 1 following the previous discussions; i.e. today we have baryonic matter

[2] There are a few exceptions to this where $z < 0$ and the light is blueshifted (such as the Andromeda Galaxy), but these are only observed in nearby galaxies that are assumed to move towards us (or us towards them) due to the gravitational pull being stronger than the expansion of the Universe.

($\Omega_b \sim 0.05$), dark matter ($\Omega_{\mathrm{DM}} \sim 0.26$), radiation ($\Omega_r \sim \mathcal{O}(10^{-5})$), and dark energy ($\Omega_\Lambda \sim 0.69$) [10].

Often, the dark matter density parameter is presented in the form $\Omega_{\mathrm{DM}}h^2$, where h is the dimensionless Hubble parameter defined as $h = H_0/(100\mathrm{km} \cdot \mathrm{s}^{-1}\mathrm{Mpc}^{-1})$. This formulation of dark matter abundance eliminates dependence on the Hubble parameter, thereby reducing associated uncertainties. The best current estimate is [10]

$$\Omega_{\mathrm{DM}}h^2 = 0.1200 \pm 0.0012. \tag{3.5}$$

The ΛCDM model has been remarkably successful in explaining a wide range of cosmological observations - not only the aforementioned CMB anisotropies, but also extending to the large-scale structure of the Universe [44–46]. It is the Standard Model equivalent of cosmology, and currently serves as the foundation for our understanding of the cosmological evolution of the Universe. However, similar to the SM of particle physics, it is not without its challenges and limitations, primarily having to do with small-scale structures.

A prominent challenge to the ΛCDM model is known as the core vs cusp problem [47]. ΛCDM simulations predicts that dark-matter dominated galaxies should have a "cuspy" density profile, meaning the density increases sharply towards the center of the halo. Rotation curve measurements of many dwarf galaxies, however, suggest that these galaxies have a "cored" density profiles, where the density remains relatively constant in the central region. Overall, the density of the central regions is also lower than expected from ΛCDM.

A solution to this problem could be self-interacting dark matter (SIDM). SIDM simulations have shown that the self-interactions of dark matter can help redistribute energy and momentum among dark matter particles, leading to the formation of more cored density profiles that are consistent with observations. Therefore, SIDM models are currently an active area of research in the field of dark matter.

While self-interactions of dark matter should be weak, as stated in the beginning of this chapter, they are not restricted to be zero. In fact, we can put an upper limit on the self-interactions of dark matter from merging galaxy systems, such as the Bullet Cluster, although the exact constraints are still debated in the literature. In 2015 Harvey et al. [40] performed a thorough analysis of 72 merging systems, and derived a constraint of $\sigma_{\mathrm{DM}}/m_{\mathrm{DM}} \lesssim 0.47\mathrm{cm}^2/\mathrm{g}$ at 95% confidence level. However, several later studies have questioned this result, generally arguing for weaker constraints. For instance, Robertson et al. [48] found that $\sigma_{\mathrm{DM}}/m_{\mathrm{DM}} \lesssim 1.25\mathrm{cm}^2/\mathrm{g}$ is still consistent with the Bullet Cluster observations, and Wittman et al. [49] argued that more comprehensive data relaxes the constraints further to $\sigma_{\mathrm{DM}}/m_{\mathrm{DM}} \lesssim 2\mathrm{cm}^2/\mathrm{g}$.

3.2.1. Thermal relics and freeze-out

The dark matter component of the ΛCDM model is often assumed to be a thermal relic (or a composition of several thermal relics). This would imply that the dark matter particles were once in thermal equilibrium with the SM particles in the early universe, and that their current abundance is determined by the freeze-out of their interactions as the universe expanded and cooled down.

This is a very appealing scenario, as it generally just requires some form of feeble interaction between the SM and the stable dark matter candidate, and it naturally leads to a dark matter density on the same order of magnitude as the baryonic matter density, despite their vastly different properties. It also provides a framework for predicting the abundance of dark matter based on some of the fundamental properties of the dark matter particles, such as their mass and interactions with SM particles. We will go through the general idea of this

calculation here, but naturally the details will depend on the specific dark matter model under consideration (as we will see later in Chapter 5).

We begin with the assumption that the dark matter particles were once in thermal equilibrium with the SM particles in the early universe. This means that the dark matter particles were being created and annihilated at rates that were much faster than the expansion rate of the universe at the time, i.e. $\Gamma_{\mathrm{SM}\leftrightarrow\mathrm{DM}} \gg H$. During this era, we can describe the number density of dark matter particles using the equilibrium distribution, which is given by the Maxwell-Boltzmann distribution for non-relativistic particles:

$$n_{\mathrm{DM,eq}} = g\left(\frac{m_{\mathrm{DM}}T}{2\pi}\right)^{3/2} e^{-m_{\mathrm{DM}}/T}, \tag{3.6}$$

where g is the number of internal degrees of freedom of the dark matter particle, m_{DM} is the mass of the dark matter particle, and T is the temperature of the universe.

As the Universe expands and cools down, the interaction rates between the dark matter particles and the SM particles will eventually become more infrequent and slower than the expansion rate of the universe, i.e. $\Gamma_{\mathrm{SM}\leftrightarrow\mathrm{DM}} \lesssim H$. At this point, the dark matter particles will "freeze out" of thermal equilibrium, meaning that their number density will no longer be determined by the equilibrium distribution. Instead, their abundance will be set by the freeze-out process.

The evolution of the number density of dark matter particles can be described by the Boltzmann equation, which takes into account both the expansion of the universe and the interactions between the dark matter particles and the SM particles. The changes in the number density of dark matter particles caused by the evolution of the Universe can be described by the Liouville operator, while the changes caused by the DM number-changing processes can be described by a collision term. The Boltzmann equation is then given by the equality of these two terms, $L = C$.

We will not derive the Liouville operator here, as it is standard for the freeze-out process, but refer the interested reader to e.g. [50]. The operator is found to be

$$L = \dot{n}_{\mathrm{DM}} + 3Hn_{\mathrm{DM}}, \tag{3.7}$$

where n_{DM} is the number density of dark matter, meaning that $\dot{n}_{\mathrm{DM}}$ is the change in number density over time (or equivalently over decreasing temperature).

The collision term, C, will depend on the specific interactions between the dark matter particles and the SM particles. It generally takes the form of a difference between the rates of processes that create and destroy dark matter particles. A typical example of the collision term comes about from considering the annihilation of two dark matter particles into 2 SM particles, $\mathrm{DM} + \mathrm{DM} \to \mathrm{SM} + \mathrm{SM}$, and can be written as:

$$C = -\langle\sigma v\rangle(n_{\mathrm{DM}}^2 - n_{\mathrm{DM,eq}}^2), \tag{3.8}$$

where $\langle\sigma v\rangle$ is the thermally averaged cross section times the relative velocity of the dark matter particles.

We then find the Boltzmann equation by setting $L = C$, which gives

$$\dot{n}_{\mathrm{DM}} + 3Hn_{\mathrm{DM}} = -\langle\sigma v\rangle(n_{\mathrm{DM}}^2 - n_{\mathrm{DM,eq}}^2). \tag{3.9}$$

This is a first order differential equation that describes the evolution of the number density of dark matter particles in the expanding universe. It can be solved to find the relic abundance of dark matter particles.

It is often more convenient to rewrite the Boltzmann equation in terms of the dimensionless yield $Y = n/s$, where s is the entropy density. This is because while the number density of particles changes due to the expansion of the Universe, the yield remains constant in the absence of number-changing interactions. This makes it easier to track the evolution of the dark matter abundance over time. Rewriting the Boltzmann equation in terms of the yield, we find

$$\frac{dY}{dx} = \frac{s}{\tilde{H}x}\langle\sigma v\rangle\left((Y^{\mathrm{eq}})^2 - Y^2\right), \tag{3.10}$$

where $x = m/T$ is the dimensionless inverse temperature. The entropy density is given by

$$s = \frac{2\pi^2}{45}h(T)T^3, \tag{3.11}$$

and the modified Hubble rate is given by [51]

$$\tilde{H} = \sqrt{\frac{8\pi^3}{90}g(T)}\frac{T^2}{M_{\mathrm{Pl}}}\left[1 + \frac{1}{3}\frac{\mathrm{d}(\ln\, h(T))}{\mathrm{d}(\ln\, \mathrm{T})}\right]^{-1}. \tag{3.12}$$

We have here introduced the functions $g(T)$ and $h(T)$, that describe the effective number of relativistic degrees of freedom contributing to the energy density and entropy density of the universe, respectively. The functions are temperature-dependent and can change significantly as the universe cools down and different particle species become non-relativistic. Correctly estimating their values across all T during freeze-out is important for accurately calculating the relic abundance of dark matter. Especially at the QCD phase transition around $T \sim 150$ MeV, where quarks and gluons become confined into hadrons, there is a significant change in the number of relativistic degrees of freedom, which can lead to a discontinuity in $g(T)$ if not treated properly. In Ref. [52], the authors provide an updated treatment of $g(T)$ and $h(T)$, taking into account results from lattice QCD simulations and other theoretical developments. We will use their tabulated values in our calculations later in section 5.2.

We can solve Equation 3.10 for dark matter particles numerically from the time of thermal equilibrium to the abundance today. The initial condition for the yield is given by the equilibrium distribution of n. From this, we then calculate the difference over small time steps, until the yield reaches a constant value, Y_∞, which corresponds to the abundance of dark matter particles today.

To express the relic abundance of dark matter in terms of Ω_{DM} we use that the current dark matter density is given by $\rho_{\mathrm{DM}} = m_{\mathrm{DM}}n_{\mathrm{DM}}$, and that the yield today is defined as $Y_\infty = n_{\mathrm{DM}}/s_0$, where s_0 is the entropy density at the present time, measured to be $s_0 \approx 2970\ \mathrm{cm}^{-3}$ [10]. We then find that

$$\Omega_{\mathrm{DM}} = \frac{m_{\mathrm{DM}}Y_\infty s_0}{\rho_c}. \tag{3.13}$$

3.3. Dark matter candidates and dark sectors

There are many proposed candidates for particle dark matter, each with its own unique properties and interactions. Some of the most popular candidates include Weakly Interacting Massive Particles (WIMPs), axions, sterile neutrinoes, and Strongly Interacting Massive Particles (SIMPs).

Further, the idea of dark sectors has gained significant attention in recent years as an extension of the SM that can possibly explain dark matter, while providing answers to some of the questions of the SM and the ΛCDM model, as well as present exciting novel phenomenology. It involves the existence of a hidden sector of particles beyond the SM that has

highly suppressed interactions with the SM, if any. The dark sector may interact with the SM through new, yet undiscovered fundamental forces, known as "portals". These portals can be mediated by new particles, such as dark photons, which can mix with the SM particles and allow for interactions between the two sectors. The dark sector may contain a variety of particles, possibly with large variations in mass and properties - similar to how the SM contains many particles with different masses and interactions. The dark matter candidate in this scenario[3] is assumed to be a stable particle in the dark sector, or a combination of several stable particles.

The landscape of dark matter candidates and dark sector models is vast, if not infinite, and we will not attempt to give a comprehensive review here. In Chapter 4 and beyond we will go into depth with a specific class of dark sector models, where the dark matter candidate is a type of SIMP. Here, we will briefly summarize the WIMP candidate, as it is undoubtedly the most well-studied candidate, as well as the SIMP candidate, which is the focus of this thesis.

3.3.1. WIMPs

WIMPs are a class of dark matter candidates that interact with the SM particles through weak-scale interactions, and have masses in the range of a few GeV to a few TeV. They are assumed to be electrically neutral and color singlets. In the classical WIMP scenario, the dark matter is charged under the $SU(2) \times U(1)$ gauge group of the SM, and thus interacts with the SM particles via the weak force. The couplings to the SM particles are typically of the order of the weak coupling constant, $g \sim 0.6$.

It is generally assumed that WIMPs achieve their relic abundance via the freeze-out mechanism described in subsection 3.2.1, with the dominant process being 2DM $\rightarrow$ 2SM annihilations. Rough estimates, approximating the annihilation cross section by $\sigma \sim g^4/4\pi m_{\mathrm{DM}}^2$, reveal that these weak-scale particles with $g \sim 0.6$ naturally give the correct relic abundance [31]. This is often referred to as the *WIMP miracle*, and has been a major motivation for WIMPs as dark matter candidates, as it gives a rather natural explanation for the observed dark matter abundance.

Another appealing aspect of WIMPs is that they often appear naturally in extensions of the SM that aim to address more of the limitations of the SM. One example is supersymmetry, where the WIMP candidate is often the lightest neutralino, and within this framework, the hierarchy problem can be resolved by WIMPs stabilizing the Higgs mass against large quantum corrections [31].

While WIMPs have been the dominant paradigm for dark matter for several decades, the lack of conclusive evidence from direct detection experiments, indirect detection searches, and collider experiments has motivated the exploration of alternative dark matter candidates [53].

3.3.2. SIMPs

An alternative, less explored, dark matter candidate is the SIMP. This candidate comes from a class of models where the dark matter particles are strongly interacting with each other, but have only feeble interactions with the SM particles, often mediated by portals. They are typically part of a confining hidden sector, initially postulated by Strassler and Zurek in 2006 [54].

An immediate challenge of the SIMP scenario is that with very feeble interactions with the SM, it is not obvious how the dark matter candidate will achieve the correct relic abundance.

[3] A dark sector does not necessarily require a dark matter candidate; in fact, some studies set aside the issue of dark matter entirely to investigate other properties and phenomena associated with the dark sector.

The classic $2\chi_{\rm DM} \to 2{\rm SM}$ annihilations are not efficient enough to reach the relic abundance in these models, and SIMPs end up being overproduced. A solution proposed by Hochberg et al. [55] is that the SIMP candidate can undergo the "*cannibalistic*" process of $3\chi_{\rm DM} \to 2\chi_{\rm DM}$, allowed by the WZW term discussed in subsection 2.2.4. The Boltzmann equation for this process is

$$\dot{n}_{\rm DM} + 3H\, n_{\rm DM} = \langle \sigma v^2 \rangle_{3\to 2} n_{\rm DM}^2 (n_{\rm DM}^{\rm eq} - n_{\rm DM}), \tag{3.14}$$

The thermally averaged cross section $\langle \sigma v^2 \rangle_{3\to 2}$ is given by [56]

$$\langle \sigma v^2 \rangle_{3\to 2} = \frac{5\sqrt{5} N_{c_D}^2 \kappa_{3\to 2} \xi^{10}}{4608 \pi^5 m_{\rm DM}^5 x^2}, \tag{3.15}$$

with

$$\kappa_{3\to 2} = \frac{N_{f_D}(N_{f_D}^2 - 4)}{(N_{f_D}^2 - 1)^2} = \frac{1}{N_{f_D}} + \mathcal{O}(N_{f_D}^{-3})\,. \tag{3.16}$$

Hochberg et al. demonstrated that this mechanism is dominant over the $2\chi_{\rm DM} \to 2{\rm SM}$ process, and as a result the dark matter mass that gives the correct relic abundance is significantly lower than in the WIMP scenario, typically in the MeV to GeV range. Being strongly interacting, SIMPs are naturally self-interacting dark matter candidates, and as it turns out, the strength of interactions needed to achieve the observed relic abundance simultaneously means self-interactions that are large enough to address several of the small-structure problems. This was dubbed *the SIMP miracle* [55]. However, this theory has faced significant challenges in the face of the Bullet Cluster constraints on the self-interaction strength of dark matter candidates. These observations suggest that dark matter must have self-interactions that are significantly weaker than those required by the SIMP miracle. Moreover, such cannibalistic processes can create significant kinetic energy within the dark sector, which is kinetically decoupled from the SM, and thus the dark thermal bath becomes overheated, leading to extended free-streaming of dark matter particles and ultimately resulting in issues with structure formation [57].

To address these issues, several alternative number-changing processes have been proposed. One such mechanism is the Co-SIMP scenario [58], where the freeze-out process involves co-annihilation between dark matter particles and SM particles in the process $\chi_{\rm DM}+\chi_{\rm DM}+{\rm SM} \to \chi_{\rm DM} + {\rm SM}$. For the Co-SIMP scenario to work, the dark sector must have a $\mathbb{Z}_N$ ($N \leq 3$) symmetry to stabilize the dark matter candidate, and a mass of $m_{\rm DM} \leq 2m_{\rm SM}$, where $m_{\rm SM}$ is the mass of the co-annihilating SM particle, as well as no couplings to photons or neutrinos. This solution yields dark matter masses of $m_{\rm DM} \leq 1$ GeV.

Another proposed mechanism involves the presence of a dark photon [59], which mediates interactions between the dark sector and the SM. In this scenario, the dark photon mixes kinetically with the SM photon, and its presence can facilitate the thermalization of the dark sector with the SM, as well as resonantly enhance the $3\chi_{\rm DM} \to 2\chi_{\rm DM}$ processes. It also provides velocity dependent self-interactions that can address the small-structure problems and evade the Bullet Cluster constraints in the $m_{\rm DM} \sim 0.2 - 2$ GeV range. Since this mechanism still relies on the WZW term, it is only valid for $N_{f_D} \geq 3$.

3.4. Dark matter searches

The search for new particles has been a central objective of particle physics experiments for decades. Even prior to the 2012 discovery of the Higgs boson [4,5] - the most recent addition to the Standard Model - the quest to uncover dark matter was already well underway [60]. The dark matter search strategies traditionally follow one of three principles, as illustrated in Figure 3.4. Below, we discuss these three search strategies with an emphasis on the accelerator-based detection.

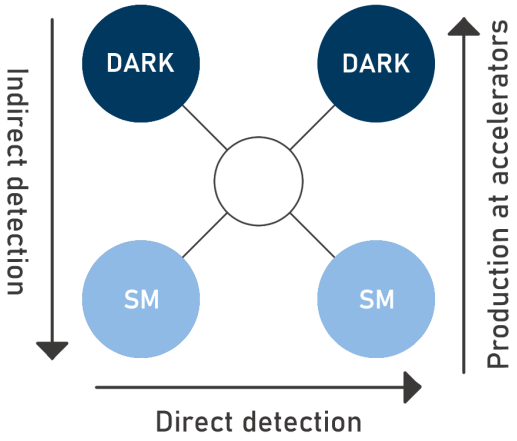

Figure 3.4.: The three typical dark matter detection methods. Read from the left to the right: Direct detection by dark matter scattering off a nucleus or electron in a detector. From top to bottom: Indirect detection by observing the products of dark matter annihilation or decay. Bottom to top: Production at accelerators where dark matter particles are produced from SM particles in high-energy collisions.

3.4.1. Direct detection

Direct detection follows the principle of detecting direct interactions between SM and dark matter particles, usually in the form of recoil events. This is where a dark matter particle scatters elastically of a nuclei or electron, resulting in the SM particle obtaining a small amount of recoil energy. The dark matter particles are assumed to come from the Milky Way halo, and are expected to be rare. Due to the low event rate, as well as low expected recoil energy, these experiments are usually built in underground detectors that are well-shielded from SM backgrounds. The typical dark matter candidate probed by direct detection experiments is the WIMP, as described in section 3.3, although the limits can generally be reinterpreted for other dark matter candidates as well.

The momentum transferred in an elastic scattering can be approximated to be [31]

$$p \approx \sqrt{m_{\mathrm{DM}} E_{\mathrm{kin}}} \tag{3.17}$$

where

$$E_{\mathrm{kin}} = \frac{1}{2}\mu v^2, \tag{3.18}$$

is the kinetic energy transferred to the target particle, with $v \sim 10^{-3}c$ being the typical velocity of dark matter particles in the Milky Way halo, and

$$\mu = \frac{m_{\mathrm{DM}} m_{\mathrm{nucl/e}}}{m_{\mathrm{DM}} + m_{\mathrm{nucl/e}}} \tag{3.19}$$

is the reduced mass of the system. From this, we see that the momentum transfer is maximized when the mass of the dark matter particle is similar to the mass of the target particle. For an electron target, this means that direct detection experiments are most sensitive to dark matter particles with masses around the MeV scale, where the recoil energy is in the eV range and the momentum transfer is in the keV range. For nuclear targets, the experiments are most sensitive to dark matter particles with masses around the tens of GeV scale, where the recoil energy is in the keV range and the momentum transfer is in the tens of MeV range.

The low energy recoils make direct detection experiments very challenging, as they require extremely sensitive detectors with very low backgrounds. The results of direct detection

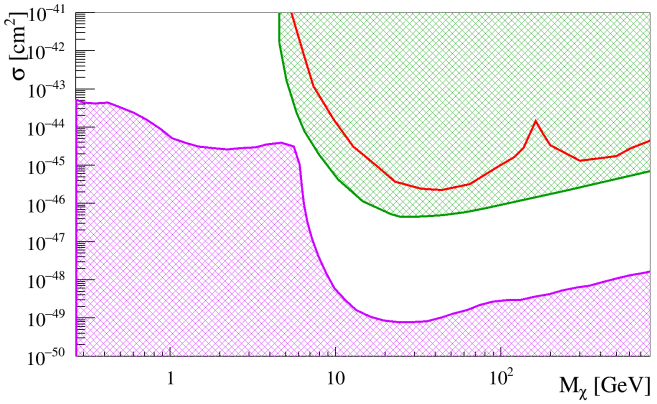

Figure 3.5.: The green region indicates the typical exclusion limits of direct dark matter experiments with null results in the σ_{SI}–m_{DM} plane, where M_χ is the dark matter mass. The violet region denotes the neutrino floor, while the red curve represents the limit derived from annual modulation analysis. Figure is from [67].

experiments are usually presented in the form of exclusion limits in the plane of the dark matter mass, m_{DM}, and the dark matter-nucleon scattering spin-independent cross section, σ_{SI}. The current best limits come from the LuxZeplin [61], XENON1T [62] and PandaX-4T [63] experiments (all based on Xenon detectors), which has excluded cross sections down to $\sigma_{\mathrm{SI}} \sim 10^{-46}$ cm^2 for dark matter masses around $m_{\mathrm{DM}} \sim 30$ GeV. Limits derived by these type of experiments are shown in the green region of Figure 3.5.

A major challenge for direct detection experiments is the so-called neutrino floor, which is the limit where neutrino interactions become a significant background. Neutrinos can interact with the detector material in a similar way as dark matter particles, producing recoils that are indistinguishable from those produced by dark matter. The neutrino floor is shown in violet in Figure 3.5, and represents a fundamental limit for direct detection experiments. In 2024, both the XENONnT [64] and PandaX-4T [65] experiments reported the first detection of coherent elastic neutrino-nucleus scattering from solar neutrinos (CEνNS), marking a significant milestone in neutrino physics and dark matter detection. This observation not only confirms a key prediction of the SM but also highlights the challenges posed by neutrino backgrounds in direct dark matter searches, as CEνNS events can mimic potential dark matter signals.

However, an alternative approach to direct detection is annual modulation analysis. This method takes advantage of the fact that the Earth orbits the Sun, which in turn orbits the center of the Milky Way. This means that the relative velocity between the Earth and the dark matter halo changes throughout the year, leading to a modulation in the expected event rate. Since solar neutrinos are not present in the dark matter gas causing the annual modulation, but rather come from the Sun, this method can help to distinguish between dark matter signals and neutrino backgrounds. While the DAMA experiment has reported a positive signal for annual modulation [66], this result has not been reproduced by other experiments, and additionally there is a lack of data sharing, and thus the result has been questioned [67]. Assuming the results can be validated, the limit derived from annual modulation analysis is shown in red in Figure 3.5. Current and upcoming experiments, such as COSINE-100 [68] and SABRE [69], aim to test the DAMA results using the same target material (NaI), but with improved background rejection and sensitivity.

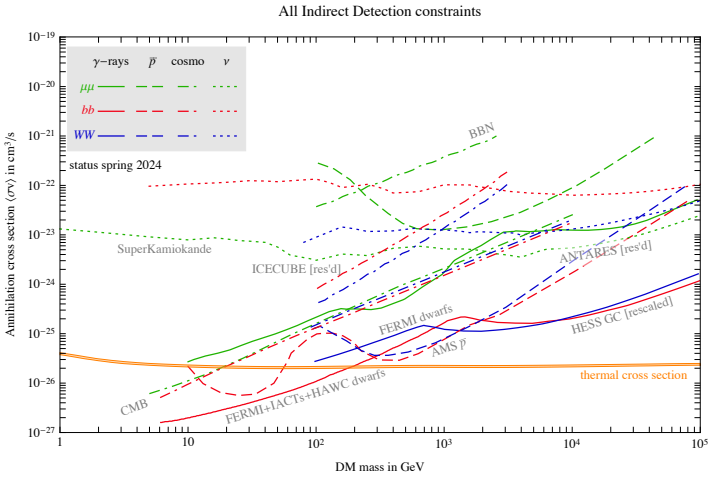

Figure 3.6.: Current limits from indirect detection experiments in the $\langle\sigma v\rangle$–M_χ plane, assuming dark matter annihilates into $\mu^+\mu^-$ (green), $\bar{b}b$ (red) or W^+W^- (blue). The thick orange line indicates the thermal relic cross section needed to achieve the correct relic abundance via the WIMP freeze-out mechanism. Figure is from [31].

3.4.2. Indirect detection

Indirect detection is based on the principle of detecting the products of dark matter annihilation or decay occuring in the galaxy. This can be done by looking for excesses in for example gamma rays, cosmic rays or neutrinoes that cannot be explained by known astrophysical sources. The typical dark matter candidate probed by indirect detection experiments is also the WIMP, as they are assumed to annihilate into SM particles with a cross section that is large enough to produce detectable signals. The annihilation cross section needed to achieve the correct relic abundance via the WIMP freeze-out mechanism is $\langle\sigma v\rangle \sim 0.73 \times 10^{-26}$ cm^3/s [31]. This cross section often serves as a benchmark for indirect detection experiments.

The highest rate of events from dark matter annihilation is expected to come from regions with high dark matter density, such as the center of the Milky Way. However, this region also presents significant challenges due to the presence of various astrophysical sources that can produce similar signals. Modelling of the astrophysical backgrounds is therefore crucial for indirect detection experiments.

Anti-protons are a particularly interesting candidate signal, as this is not expected to be produced in large quantities by known astrophysical sources. Several experiments, such as the space-based AMS-02 experiment, have searched for anti-proton excess in cosmic rays, and have reported an excess that could potentially be explained by annihilation of a dark matter candidate of $\sim$ 80 GeV [70]. However, the interpretation of this excess is still debated, in particular due to the uncertainties in the modelling and the treatment of correlations among the data [31, 71].

The results of indirect detection experiments are usually presented in the form of exclusion limits in the plane of the dark matter mass, m_{DM}, and the velocity-averaged annihilation cross section, $\langle\sigma v\rangle$. Some of the current best limits come from the Fermi-LAT [72], which have excluded cross sections down to $\langle\sigma v\rangle \sim 10^{-26}$ cm^3/s for dark matter masses around $m_{\mathrm{DM}} \sim 100$ GeV, assuming dark matter annihilates into $b\bar{b}$ quarks. Limits derived by these type of experiments are shown in Figure 3.6.

3.4.3. Accelerator-based detection

Accelerator-based detection is based on the principle of producing dark matter particles in high-energy particle collisions, and then detecting their interactions with SM particles. Historically, this has been the primary method for discovering new particles in particle physics. Accelerator-based detection has the advantage of being able to produce dark matter particles in a highly controlled environment, where the initial conditions, such as input energy and background, are well-known. This allows for precise measurements of the properties of new particles, such as their mass and interactions with SM particles.

The simplest idea of dark matter detection at accelerators is to produce them in SM particle collisions, where they subsequently, under the assumption of stability, escape the detector without interacting. This leads to an imbalance in the momentum and energy of the detected particles, which can be used to infer the presence of dark matter particles. This is often referred to as "missing transverse energy" (MET) searches, or "mono-X" searches, where X is a SM particle that is produced in association with the dark matter particles, such as photons or jets. WIMPs are generally asummed to leave such signatures, and thus, MET searches are often interpreted in the context of WIMP models.

However, more complicated signatures are possible as well, depending on the specific dark matter model under consideration. For instance, if a massive portal is involved, the production rate of interactions related to the portal could be resonantly enhanced near the mass of the portal. We expect that this would lead to a peak in the invariant mass distribution of suspected decay products. This is often referred to as "bump hunts", and was how the Higgs boson was discovered in 2012 [4, 5]. Another example is if the theory contains new particles with long lifetimes, leading to displaced vertices or other unusual signatures like emerging jets, although such unstable particles would not be the dark matter candidate. Dark sector models may not only contain one such particle or portal, but may even contain several new particles with different masses and lifetimes, leading to a rich phenomenology. The increased complexity of the models open up a wide range of possible signatures, and accelerator-based detection is a powerful tool to explore these possibilities.

There are many ways to categorize accelerator experiments, depending on the setup and the type of particles being collided, and these variables have a significant impact on the types of dark matter candidates that can be probed, as well as the sensitivity of the experiments. Accelerator experiments can be in the form of collider experiments, where two high-intensity beams are collided head-on, or fixed-target experiments, where a high-intensity beam of particles is sent onto a stationary target. We will first discuss the former.

The current highest energy collider, and undoubtedly the most well-known, is the Large Hadron Collider (LHC) at CERN, which collides protons at a center of mass energy of $\sqrt{s} = 13$ TeV. Proton-proton collisions generally result in events with complicated hadronic final states. While these can contain very interesting dynamics, or traces thereof, these events are also very challenging to analyze.

The LHC has been operational since 2009, and has been the site of several important discoveries, most notably the discovery of the Higgs boson. The LHC consists of many experiments, with the main four being ATLAS, CMS, LHCb and ALICE. The ATLAS and CMS experiments are general-purpose detectors, designed to search for a wide range of new particles and phenomena, while the LHCb experiment is focused on studying the properties of b-quarks, and the ALICE experiment is focused on studying heavy-ion collisions. No conclusive evidence for dark matter particles has been found so far, leading to increasingly stringent limits on the properties of dark matter candidates.

Some of the LHC results can be seen in Figure 3.7, which shows the current limits on the mass and coupling of a hypothetical vector mediator, assuming that the mediator couples to

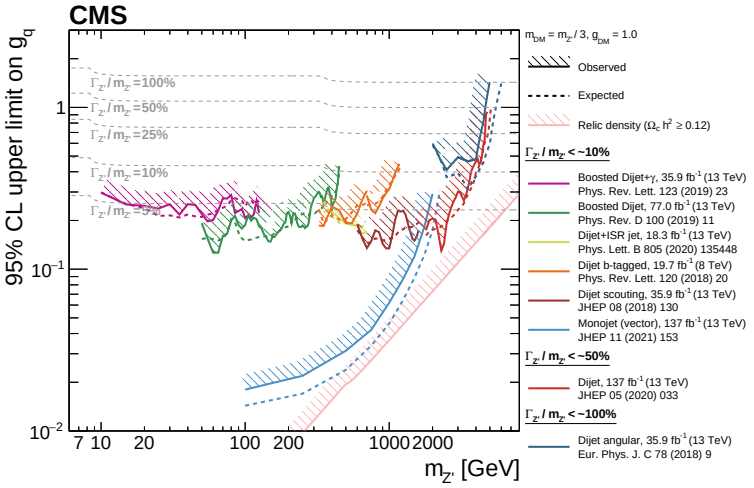

Figure 3.7.: Observed and expected 95% CL exclusion regions on a vector mediator coupling universally to SM quarks with g_q, and to dark matter with coupling $g_{\mathrm{DM}} = 1$. Figure is from [74].

all SM with equal strength, expressed as g_q (and to dark matter with coupling $g_{\mathrm{DM}} = 1$). The limits are derived from different searches, as indicated by the figure. The light pink line shows the relic abundance line, meaning that the region left of this line would lead to overproduction of dark matter in the early universe, and is thus excluded. The figure shows that a large region of parameter space has been excluded, but there are still many possibilities left to explore. ATLAS provides similar limits [73], and the two experiments often perform similar searches, ensuring that results can be validated independently.

An additional challenge of proton-proton colliders lies in the fact that protons are composite particles, made up of quarks and gluons, meaning that the actual collisions occur between the constituent partons of the protons. This means that the center of mass energy of the partonic collision is lower than the center of mass energy of the proton-proton collision, and can vary significantly from event to event. The partonic center of mass energy is given by $\sqrt{\hat{s}} = x_1 x_2 \sqrt{s}$, where x_1 and x_2 are the momentum fractions of the partons involved in the hard scattering process. The values of x_1 and x_2 can vary depending on the specific partons involved and the kinematics of the event.

One way to mitigate some of these challenges is to use electron-positron colliders, which collide electrons and positrons at high energies. Electron-positron collisions generally result in events with cleaner final states, and since electrons and positrons are elementary particles, the entire center of mass energy is available for the collision. This makes electron-positron colliders particularly well-suited for precision measurements of particle properties, as well as searches for new particles with relatively low masses.

The Large Electron-Positron Collider (LEP) at CERN was the predecessor to the LHC, and operated from 1989 to 2000, colliding electrons and positrons at center of mass energies up to $\sqrt{s} \approx 200$ GeV. The LEP experiments, ALEPH, DELPHI, L3 and OPAL, made several important measurements of the properties of the Z and W bosons, as well as searches for new particles [75]. More recently, the Belle II experiment at the SuperKEKB collider in Japan has been operational since 2018, colliding electrons and positrons in an asymmetric system at a center of mass energy of $\sqrt{s} = 10.58$ GeV. The Belle II experiment is focused on studying the properties of B-mesons in the form of rare decays, as well as searching for new particles and phenomena [76, 77].

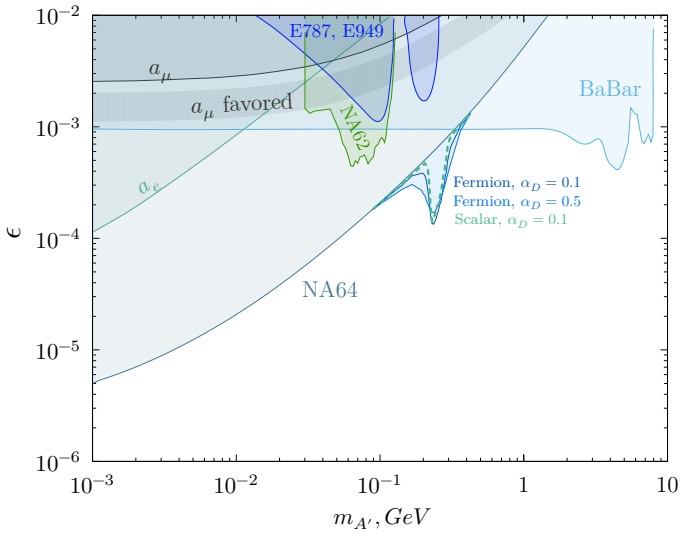

Figure 3.8.: Exclusion limits on the kinetic mixing parameter ϵ as a function of the dark photon mass $m_{A'}$ from the NA64 and NA62 experiments, BaBar and the E787 and E949 experiments. Figure is from [78].

Next, we turn to fixed-target experiments, which also encompass beam-dump experiments. In fixed-target setups, an electron beam is typically directed at a thin target, whereas beam-dump experiments involve directing either an electron or proton beam at a thick target. The center of mass energies of these experiments are often (though not always) lower than those of collider experiments, but they have the advantage of being able to deliver high luminosities, meaning that they can produce a large number of events. This makes them particularly well-suited for searching for new particles with very weak interactions with the SM particles, as well as for studying rare processes.

Another advantage of fixed-target and beam-dump experiments is that they can be designed to be sensitive to long-lived particles (LLPs). This is particularly relevant for dark sector models, where the dark matter candidate may be part of a larger dark sector containing several new particles with different masses and lifetimes. To optimize sensitivity to LLPs, these experiments often have a near and a far detector, where the near detector is used to measure the background from SM processes, while the far detector is used to search for signals from LLPs that decay after traveling some distance.

NA64 is a fixed-target experiment at CERN that has been operational since 2016, using a high-intensity electron beam with an energy of 100-150 GeV extracted from the Super Proton Synchrotron (SPS). The experiment is designed to search for dark sector particles by looking for missing energy signatures in electron-nucleus collisions. NA62 is another fixed-target experiment at CERN, also operational since 2016 and uses a beam extracted from the SPS. However, it uses a proton beam with an energy of 400 GeV. The experiment is primarily focused on studying rare kaon decays, but it also has the capability to search for dark sector particles. Recent results from NA64 and NA62 on the search for dark photons are shown in Figure 3.8.

After the run of these experiments finishes at CERN, new experiments have already been proposed and accepted. One of these is the SHiP experiment. This is also a beam-dump experiment that will use a high-intensity proton beam from the SPS with $\sqrt{s} = 27.42$ GeV. The goal of SHiP is to study neutrinoes as well as to search for dark sector particles. The experiment is designed to be sensitive to a wide range of dark sector models, including those with LLPs. SHiP is expected to start taking data in 2031 [79].

CHAPTER 4

Strongly Interacting Dark Sectors

In this chapter, we introduce the framework for a strongly interacting dark sector that forms the basis of this thesis. While such sectors can be realized through a variety of theoretical constructions, we focus on a specific type of model, namely a QCD-like dark sector. We will introduce this in section 4.1, and use the model consistently throughout our analysis. This setup is chosen because it captures exciting aspects of dark matter phenomenology, can account for the observed relic abundance, and remains both theoretically well-motivated and experimentally testable.

The dark sector under consideration features a compelling dark matter candidate: the dark pion. In addition to the dark pion, the theory includes a dark vector meson, commonly referred to as the dark rho. This particle contributes significantly to the internal dynamics of the dark sector and can influence both cosmological and collider phenomenology. We describe the origin of these particles and their interactions within the dark sector in subsection 4.1.1.

Crucially, the dark sector is not entirely secluded from the SM. We incorporate a massive vector portal, which facilitates interactions between the dark sector and SM particles. This portal plays a key role in connecting the hidden dynamics of the dark sector to observable phenomena. This is detailed in subsection 4.1.2.

This dark sector model is particularly intriguing due to its rich phenomenological implications. It offers a framework that can accommodate self-interacting dark matter, generate distinctive collider signatures, and provide a viable explanation for the observed dark matter relic abundance. Key phenomenological aspects of this type of dark sector is outlined in section 4.2, though it will be studied in more details in later chapters.

In section 4.3, we discuss the simulation of the dark sector, which is essential for making precise predictions and comparing them with experimental data. We outline the computational tools and techniques employed to model the dark sector's behavior and interactions.

4.1. Our dark sector setup

In this work, we focus on a strongly interacting dark sector from a new $SU(N_{c_D})$ gauge group with N_{f_D} mass-degenerate dark quarks, q_d, in the fundamental representation. We will

at all times assume that the dark sector exhibits asymptotic freedom at high energies and confinement at low energies, distinguished by the dark confinement scale Λ_D. We expect this to be valid as long as we choose $N_{f_D} < 3N_{c_D}$ [3]. The theory is therefore similar to SM QCD and can also be referred to as dark QCD or a QCD-like dark sector. This means that a lot of the tools we used to describe SM QCD in Chapter 2 can be applied to our dark sector. In particular, we will use the chiral perturbation theory (ChPT) framework to describe the low-energy effective field theory of the dark sector.

We have pseudo-Goldstone bosons of spin 0 in our dark sector, dark pions π_D. These will be essential in our studies of the dark sector. We describe them with a Dark Chiral Lagrangian, using the subscript D to denote the dark equivalent of the SM parameters discussed in Chapter 2. The Dark Chiral Lagrangian is

$$\mathcal{L}_{\mathrm{Ch_{Dark}}} = \frac{f_{\pi_D}^2}{4}\mathrm{Tr}\left(\partial_\mu U \partial^\mu U^\dagger\right) + \left[\frac{\mu_D^3}{2}\mathrm{Tr}\left(M_{q_D}U^\dagger\right) + \mathrm{h.c.}\right], \tag{4.1}$$

where M_{q_D} is the dark quark mass martrix. Since we assume mass-degenerate quarks, for simplicity, we will replace M_{q_D} with the scalar quantity m_{q_D}, where we implicitly assume multiplication with the identity matrix when it is used in matrix expressions.

However, the dark pions are not the only mesons of the theory, as there also exists a spin-1 meson for every spin-0 meson with a similar quark content. We call these dark rho mesons, ρ_D. If the ρ_D is expected to have significance to the dynamics and phenomenology of the theory, it will be necessary to include their effect in the Chiral Lagrangian for more accurate descriptions and predictions. This is typically not considered in the SM case, as the SM ρ meson is almost ~ 6 times heavier than the pion, and thus is not relevant for most calculations.

In our dark sector, we do not know the mass of the π_D or ρ_D a priori, and we can therefore imagine a scenario where the ρ_D is much closer to the π_D in mass. Indeed, the majority of this thesis will focus on a scenario where the ρ_D is relatively light, with a mass of $m_{\rho_D} \lesssim 2m_{\pi_D}$. This means that the ρ_D will be relevant for the dynamics of the dark sector and will need to be included in the Dark Chiral Lagrangian.

4.1.1. Interactions between the dark mesons

We describe the interactions between π_D and ρ_D using the Massive Yang-Mill approach [80]. Here we promote the derivative ∂_μ in Equation 4.1 to the covariant derivative defined as

$$D_\mu U = \partial_\mu U + i g_{\pi_D\rho_D}[U, \rho_{D\mu}], \tag{4.2}$$

where $g_{\pi_D\rho_D}$ is the coupling between dark pions and rho mesons. We obtain a relation for this coupling to the dark pion mass and decay constant via the KSRF relation [81]. It is given by

$$g_{\pi_D\rho_D} \approx m_{\rho_D}/(\sqrt{2}f_{\pi_D}). \tag{4.3}$$

Remembering the definition of the pion field $U = \exp\left(2i\frac{\pi_D}{f_{\pi_D}}\right)$, we can insert this and the covariant derivative into the kinematic part of Equation 4.1, and we find the following terms up to $\mathcal{O}(\pi^4)$ (see chapter A for a detailed derivation of this):

$$\begin{aligned}\mathcal{L}_{\mathrm{Ch}} \supset & \mathrm{Tr}\left(D_\mu\pi_D D^\mu\pi_D\right) + m_{\pi_D}^2\mathrm{Tr}\left(\pi_D^2\right) + \frac{m_{\pi_D}^2}{3f_{\pi_D}^2}\mathrm{Tr}\left(\pi_D^4\right) \\ & - \frac{2}{3f_{\pi_D}^2}\mathrm{Tr}\left(\pi_D^2 D_\mu\pi_D D^\mu\pi_D - \pi_D D_\mu\pi_D\pi_D D^\mu\pi_D\right).\end{aligned} \tag{4.4}$$

The second term, $m_{\pi_D}^2\mathrm{Tr}\left(\pi_D^2\right)$, is the mass term for the dark pions. The other three terms contain interaction terms between the dark pions and the dark rhos, as well as the kinetic term. We will expand these according to the order of pion fields.

$\mathcal{O}({\pi_D}^2)$ interactions

The first term gives us the following

$$\begin{aligned}\mathrm{Tr}\left(D_\mu\pi_D D^\mu\pi_D\right) &= \mathrm{Tr}\left(\left(\partial_\mu\pi_D + ig[\pi_D,\rho_{D\mu}]\right)\left(\partial^\mu\pi_D + ig[\pi_D,{\rho_D}^\mu]\right)\right)\\ &= \mathrm{Tr}\left(\partial_\mu\pi_D\right)^2 + ig\mathrm{Tr}\left(\partial_\mu\pi_D[\pi_D,{\rho_D}^\mu] + [\pi_D,\rho_{D\mu}]\partial^\mu\pi_D + ig[\pi_D,\rho_{D\mu}][\pi_D,{\rho_D}^\mu]\right). \quad (4.5)\\ &= \mathrm{Tr}\left(\partial_\mu\pi_D\right)^2 + ig\mathrm{Tr}\left(\underline{2\cdot\partial_\mu\pi_D[\pi_D,{\rho_D}^\mu]} + \underline{ig[\pi_D,\rho_{D\mu}][\pi_D,{\rho_D}^\mu]}\right),\end{aligned}$$

where we have used the cyclic property of the trace in the last equality. $\mathrm{Tr}\left(\partial_\mu\pi_D\right)^2$ is the kinetic term. The term underlined in blue gives us the Lagrangian for the $2\pi_D\rho_D$ interactions;

$$\mathcal{L}_{2\pi_D\rho_D} = 2ig_{\pi_D\rho_D}\mathrm{Tr}\left(\partial_\mu\pi_D[\pi_D,{\rho_D}^\mu]\right). \quad (4.6)$$

We will do a detailed study of this interaction as it becomes important in later chapters. However, most other interactions will not be as important for our studies, and we will therefore not go into as much detail with them.

The dark pion field π_D can be expressed as $\pi_D = {\pi_D}^a T^a$, where T^a are the generators of the gauge group, normalized such that $\mathrm{Tr}(T^aT^b) = \frac{1}{2}\delta^{ab}$. Similarly, we write $\rho_D = {\rho_D}^a T^a$, and so we are interested in the non-Abelian commutation relation for the generators, which is given by:

$$[T^a,T^b] = i\epsilon^{abc}T^c \quad (4.7)$$

where ϵ^{abc} is the totally antisymmetric Levi-Civita symbol. We will use that

$$[\pi_D,\rho_{D\mu}] = {\pi_D}^a{\rho_D}^b_\mu[T^a,T^b] = {\pi_D}^a{\rho_D}^b_\mu(T^aT^b - T^bT^a)$$

Inserting this into Equation 4.6 and considering permutations, which corresponds to switching the indices of the two incoming dark pions, we get

$$\begin{aligned}\mathcal{L}_{2\pi_D\rho_D} &= 2ig\mathrm{Tr}\left(\partial^\mu{\pi_D}^a T^a{\pi_D}^b{\rho_D}^c_\mu[T^b,T^c] + \partial^\mu{\pi_D}^b T^b{\pi_D}^a{\rho_D}^c_\mu[T^a,T^c]\right)\\ &= 2ig_{\pi_D\rho_D}{\rho_D}^c_\mu\mathrm{Tr}\left(\partial_\mu{\pi_D}^a{\pi_D}^b(T^aT^bT^c - T^aT^cT^b) + \partial_\mu{\pi_D}^b{\pi_D}^a(T^bT^aT^c - T^bT^cT^a)\right)\\ &= 2ig_{\pi_D\rho_D}{\rho_D}^c_\mu\mathrm{Tr}\left(\partial_\mu{\pi_D}^a{\pi_D}^b(T^aT^bT^c - T^bT^aT^c) + \partial_\mu{\pi_D}^b{\pi_D}^a(T^bT^aT^c - T^aT^bT^c)\right)\\ &= 2ig_{\pi_D\rho_D}{\rho_D}^c_\mu\mathrm{Tr}\left(\partial_\mu{\pi_D}^a{\pi_D}^b[T^a,T^b]T^c + \partial_\mu{\pi_D}^b{\pi_D}^a(-)[T^a,T^b]T^c\right)\\ &= 2ig_{\pi_D\rho_D}{\rho_D}^c_\mu\mathrm{Tr}\left((\partial_\mu{\pi_D}^a{\pi_D}^b - {\pi_D}^a\partial_\mu{\pi_D}^b)[T^a,T^b]T^c\right)\\ &= 2ig_{\pi_D\rho_D}{\rho_D}^c_\mu(\partial_\mu{\pi_D}^a{\pi_D}^b - {\pi_D}^a\partial_\mu{\pi_D}^b)\mathrm{Tr}\left([T^a,T^b]T^c\right), \quad (4.8)\end{aligned}$$

where we have used the cyclic property of the trace to change the order of the generators in the trace. We see that the interaction is proportional to $\mathrm{Tr}\left([T^a,T^b]T^c\right)$, which is a group theory factor that depends on the gauge group. For $SU(N_{f_D})$, this factor is given by $\mathrm{Tr}\left([T^a,T^b]T^c\right) = \epsilon^{abc}N_{f_D}(N_{f_D}^2-1)/4$. Thus, we can write the $2\pi_D\rho_D$ interaction Lagrangian as

$$\mathcal{L}_{2\pi_D\rho_D} = \frac{N_{f_D}(N_{f_D}^2-1)}{2}ig_{\pi_D\rho_D}\epsilon^{abc}{\rho_D}^c_\mu(\partial_\mu{\pi_D}^a{\pi_D}^b - {\pi_D}^a\partial_\mu{\pi_D}^b). \quad (4.9)$$

We can directly see from this, that terms with equal indices, like $\pi_D^3\pi_D^3\rho_D^3$ are forbidden. These mesons correspond to neutral mesons once a dark charge is introduced (as we will discuss in subsection 4.1.2), such that in that case, interactions like $\rho_D^0 \to \pi_D^0\pi_D^0$ do not exist.

The term underlined in red in Equation 4.5 gives us the Lagrangian for the $2\pi_D2\rho_D$ interactions;

$$\mathcal{L}_{2\pi_D2\rho_D} = -g^2_{\pi_D\rho_D}\mathrm{Tr}\left([\pi_D,\rho_{D\mu}][\pi_D,{\rho_D}^\mu]\right) \quad (4.10)$$

$\mathcal{O}({\pi_D}^4)$ interactions

Going back to Equation 4.4, we now expand the $\mathcal{O}({\pi_D}^4)$ term as

$$
\begin{aligned}
&-\tfrac{2}{3f_{\pi_D}^2}\mathrm{Tr}\Big(\pi_D^2 D_\mu \pi_D D^\mu \pi_D - \pi_D D_\mu \pi_D \pi_D D^\mu \pi_D\Big) \\
&\qquad = -\tfrac{2}{3f_{\pi_D}^2}\mathrm{Tr}\Big(\pi_D^2(\partial_\mu \pi_D + ig_{\pi_D\rho_D}[\pi_D, \rho_{D\mu}])(\partial^\mu \pi_D + ig_{\pi_D\rho_D}[\pi_D, \rho_D{}^\mu]) \\
&\qquad\qquad - \pi_D(\partial_\mu \pi_D + ig_{\pi_D\rho_D}[\pi_D, \rho_{D\mu}])\pi_D(\partial^\mu \pi_D + ig_{\pi_D\rho_D}[\pi_D, \rho_D{}^\mu])\Big) \\
&\qquad = -\tfrac{2}{3f_{\pi_D}^2}\mathrm{Tr}\Big(\underline{{\pi_D}^2 \partial_\mu \pi_D \partial^\mu \pi_D} + ig_{\pi_D\rho_D}{\pi_D}^2 \partial_\mu \pi_D[\pi_D, \rho_D{}^\mu] \\
&\qquad\qquad + ig_{\pi_D\rho_D}{\pi_D}^2[\pi_D, \rho_{D\mu}]\partial^\mu \pi_D - \underline{g^2_{\pi_D\rho_D}{\pi_D}^2[\pi_D, \rho_{D\mu}][\pi_D, \rho_D{}^\mu]} \\
&\qquad\qquad - \underline{\pi_D \partial_\mu \pi_D \pi_D \partial^\mu \pi_D} - ig_{\pi_D\rho_D}\pi_D \partial^\mu \pi_D \pi_D[\pi_D, \rho_D{}^\mu] \\
&\qquad\qquad - ig_{\pi_D\rho_D}\pi_D[\pi_D, \rho_{D\mu}]\pi_D \partial^\mu \pi_D + \underline{g^2_{\pi_D\rho_D}\pi_D[\pi_D, \rho_{D\mu}]\pi_D[\pi_D, \rho_D{}^\mu]}\Big)
\end{aligned}
\tag{4.11}
$$

The terms underlined in blue give us the $4\pi_D$ interactions, however we also have a contribution from the mass term in Equation 4.4, which gives us the full $4\pi_D$ interaction Lagrangian as

$$
\mathcal{L}_{4\pi_D} = -\tfrac{2}{3f_{\pi_D}^2}\mathrm{Tr}\Big({\pi_D}^2 \partial_\mu \pi_D \partial^\mu \pi_D - \pi_D \partial_\mu \pi_D \pi_D \partial^\mu \pi_D + \frac{{m_{\pi_D}}^2}{2}{\pi_D}^4\Big) \tag{4.12}
$$

The terms underlined in red give us interactions containing both $4\pi_D$ and $2\rho_D$, and we can write it as

$$
\mathcal{L}_{4\pi_D 2\rho_D} = -\tfrac{2}{3f_{\pi_D}^2}\mathrm{Tr}\Big(-g^2_{\pi_D\rho_D}{\pi_D}^2[\pi_D, \rho_{D\mu}][\pi_D, \rho_D{}^\mu] + g^2_{\pi_D\rho_D}\pi_D[\pi_D, \rho_{D\mu}]\pi_D[\pi_D, \rho_D{}^\mu]\Big) \tag{4.13}
$$

Finally, the remaining terms give us the interactions containing $4\pi_D$ and $1\rho_D$, and we write it as

$$
\mathcal{L}_{4\pi_D\rho_D} = -\tfrac{2ig_{\pi_D\rho_D}}{3f_{\pi_D}^2}\mathrm{Tr}\Big({\pi_D}^2 \partial^\mu \pi_D[\pi_D, \rho_D{}^\mu] + {\pi_D}^2[\pi_D, \rho_{D\mu}]\partial^\mu \pi_D - 2\pi_D \partial^\mu \pi_D \pi_D[\pi_D, \rho_D{}^\mu]\Big). \tag{4.14}
$$

4.1.2. A vector portal to the Standard Model

The dark sector structure as described above is fully isolated from the SM, as we have not yet introduced any sort of interactions between the two sectors. This idea suffers from a glaring challenge; the lack of verifiable tests[4]. There exists several choices of portals, such as a scalar portal or a Higgs portal. We will consider the case of a vector portal, arising from the introduction of a $U(1)'$ gauge symmetry, under which both the dark fermions and the SM fermions are charged. This leads to the emergence of a neutral, boson, denoted Z', that mediate interactions between the dark sector and the SM. We assume that the Z' is a massive boson, with mass $m_{Z'}$, which can be generated either via a dark Higgs mechanism [83] or the Stueckelberg mechanism [84].

[4]We may still be able to test truly isolated dark sector via its gravitational effects or effects on cosmology, though the latter is already highly constrained [82].

The full Lagrangian describing the Z' is

$$\mathcal{L}_{Z'} = -\frac{1}{4}Z'^{\mu\nu}Z'_{\mu\nu} + \frac{1}{2}m_{Z'}^2 Z'^{\mu}Z'_{\mu} - \kappa e Z'_{\mu}\sum_f q_f \bar{f}\gamma^{\mu}f - e_D Z'_{\mu}\sum_{q_D}\bar{q}_D\gamma^{\mu}Q_{q_D}q_D. \tag{4.15}$$

The first two terms are the kinetic and mass terms for the Z', respectively. The third term describes the interactions between the Z' and the SM fermions, and the fourth term describes the interactions between the Z' and the dark quarks. Here, κ is the kinetic mixing parameter, e is the electromagnetic coupling constant, q_f is the electric charge of the SM fermion f. The sum runs over all SM fermions.

The interactions between the Z' and the SM arise from kinetic mixing with the SM hypercharge field, B_μ. This mixing introduces a term in the Lagrangian of the form [85, 86]

$$\mathcal{L}_{\text{SM mix}} = -\frac{\kappa}{2c_W}Z'^{\mu\nu}B_{\mu\nu}, \tag{4.16}$$

where κ is the kinetic mixing parameter, $B_{\mu\nu}$ is the field strength tensor of the hypercharge field, c_W is the cosine of the weak mixing. After electroweak symmetry breaking, this mixing induces photon-like couplings for the Z' to the SM fermions. The effective interaction term can be written as

$$\mathcal{L}_{Z'\text{-SM}} = -\kappa e Z'_{\mu}\sum_f q_f \bar{f}\gamma^{\mu}f, \tag{4.17}$$

where e is the electromagnetic coupling constant, q_f is the electric charge of the SM fermion f. This allows the Z' to mediate interactions between the dark sector and the SM through its coupling to SM fermions. For simplicity, we will assume that the Z' couples universally to all SM fermions, although this is not a strict requirement. In the case that the couplings are not universal, we expect the phenomenology to be qualitatively similar, but with different branching ratios for the Z' decays into various SM fermions.

The coupling of the Z' to the dark quarks depends on the $U(1)'$ gauge coupling, denoted e_D, and the dark quark charges under the $U(1)'$ gauge symmetry. We can write the charges of the dark quarks in a $N_{f_D} \times N_{f_D}$ diagonal matrix, Q_D, where the eigenvalues, denoted Q_{q_D}, correspond to the charge of the dark quark q_D. The choice of Q_D can significantly impact the phenomenology of the dark sector, as it influences decay patterns and stability of the dark mesons [3, 87]. Further details of this will be explored in section 4.2.

At low energies, where we describe the dark sector in terms of dark mesons, we need to include the interactions between the Z' and the dark mesons in our Dark Chiral Lagrangian. To describe the interactions with the dark pions, we extend the covariant derivative in Equation 4.2 to include the Z' as

$$D_\mu \pi_D = \partial_\mu \pi_D + i g_{\pi_D\rho_D}[\pi_D, \rho_{D\mu}] + i e_D [\pi_D, Q_D] Z'_\mu. \tag{4.18}$$

Additionally, we will find a kinetic mixing term between the Z' and the vector mesons in the effective Lagrangian [87, 88], which can be written as

$$\mathcal{L}_{\text{dark mix}} = -\frac{e_D}{g_{\pi_D\rho_D}}Z'_{\mu\nu}\text{Tr}(Q_D {\rho_D}^{\mu\nu}), \tag{4.19}$$

where ${\rho_D}^{\mu\nu} = \partial^\mu {\rho_D}^\nu - \partial^\nu {\rho_D}^\mu - ig[{\rho_D}^\mu, {\rho_D}^\nu]$.

In Appendix B we expand this term for the example $N_{f_D} = 2$ and $Q_D = \text{diag}(1, -1)$ to find the mixing between the Z' and the individual dark rho mesons. Higher values of N_{f_D} will yield quantitatively the same results, but with additional mesons included in the interactions.

The expanded Lagrangian for the interactions between the Z' and the dark rho mesons gives us

$$\mathcal{L}_{Z'-\rho_D} = -\frac{e_D}{g_{\pi_D\rho_D}} Z'_{\mu\nu}\left(\partial^\mu \rho_D^{0\nu} - \partial^\nu \rho_D^{0\mu}\right) + ie_D Z'_{\mu\nu}(\rho_D^{+\mu}\rho_D^{-\nu} - \rho_D^{-\mu}\rho_D^{+\nu}). \tag{4.20}$$

We see that we have interactions between the Z' and charged $\rho_D^\pm$ in the form of $Z'\rho_D^+\rho_D^-$, leading to annihilation and creation of $\rho_D^+\rho_D^-$ pairs through the Z'. However, the most important interaction for our studies is the mixing between the Z' and the neutral ρ_D^0, which is given by the first term in Equation 4.20. This kinetic mixing induces interactions directly between the ρ_D^0 and the SM fermions, in the same way as the Z' couples to SM fermions in Equation 4.15.

Under the assumption $m_{Z'} \gg \sqrt{s} \gg \Lambda_D$, which will hold for all cases studied in this thesis, the coupling between the ρ_D^0 and the SM fermions can be written as [88]

$$\mathcal{L}_{\rho_D^0\text{-SM}} = \frac{\kappa \cdot e \cdot e_D}{g_{\pi_D\rho_D}} \frac{m_{\rho_D}^2}{m_{Z'}^2} \rho_{D\mu}^0 \sum_f q_f \bar{f}\gamma^\mu f. \tag{4.21}$$

We can define a suppression scale, Λ, for this interaction as

$$\Lambda \equiv \frac{m_{Z'}}{\sqrt{\kappa e e_D}}, \tag{4.22}$$

such that

$$\mathcal{L}_{\rho_D^0\text{-SM}} = \frac{2}{g_{\pi_D\rho_D}} \frac{m_{\rho_D}^2}{\Lambda^2} \rho_{D\mu}^0 \sum_f q_f \bar{f}\gamma^\mu f. \tag{4.23}$$

We can understand the suppression scale Λ in the way that a larger Λ corresponds to a heavier Z' and/or weaker couplings to SM, and so the interaction in Equation 4.23 is more suppressed. Conversely, a smaller Λ indicates a lighter Z' and/or stronger couplings to SM, and the mixing will become enhanced. This scale will be important for our studies of the collider phenomenology of the dark sector, as it will influence the decay rates and lifetimes of the dark mesons, as well as their production rates in various processes.

4.1.3. Fundamental parameters of the theory

Let's begin by considering only the $SU(N_{c_D})$ part of the dark sector. We have four fundamental parameters in our $SU(N_{c_D})$ theory; the two discrete parameters, N_{c_D} and N_{f_D}, and the two continuous parameters, Λ_D and m_{q_D} - alternatively, we could consider one dimensional scale and one ratio, namely Λ_D and Λ_D/m_{q_D}. These parameters are meaningful in the high energy regime, but in the low energy regime we exchange them for more suitable parameters. N_{c_D} and N_{f_D} remain fundamental parameters, but we are now interested in the dimensional scale and ratio in terms of other quantities. In the low energy regime, we consider two kinds of dark mesons, the dark pions and dark rhos. The most interesting quantities to consider are perhaps the masses of these mesons, m_{π_D} and m_{ρ_D}. We therefore choose to work with m_{π_D} as our dimensional scale, and the ratio $r_m \equiv \frac{m_{\rho_D}}{m_{\pi_D}}$ as our ratio.

As evident from Equation 4.1, the interactions in the dark sector at low energies are also governed by the dark pion decay constant, f_{π_D}. This parameter is especially important in the context of the self-interactions of the dark pions. We can relate f_{π_D} to our ratio m_{ρ_D}/m_{π_D} via non-perturbative methods, using results from Ref. [89], and we find an approximate relation between the quantities as

$$\xi \equiv \frac{m_{\pi_D}}{f_{\pi_D}} = 7.79\frac{m_{\pi_D}}{m_{\rho_D}} + 0.57\left(\frac{m_{\pi_D}}{m_{\rho_D}}\right)^2 = 7.79 \cdot r_m^{-1} + 0.57 \cdot r_m^{-2}, \tag{4.24}$$

which is generally valid for $0.4 \lesssim \xi \lesssim 8$ or $1 < r_m \lesssim 20$ [1]. However, the higher values of ξ, or equivalently lower r_m, are uncomfortably close to the perturbative limit of $m_{\pi_D}/f_{\pi_D} \approx 4\pi$. As we move towards this limit, we can no longer trust the chiral perturbation theory description as higher order corrections become increasingly important [90]. We therefore restrict ourselves to $\xi \lesssim 5.7$, or $r_m \gtrsim 1.45$, motivated by the validity of the Gell-Mann-Oakes-Renner relations [16, 91].

We may wish to relate the high energy and low energy parameters, for example to define high-energy input parameters for simulation tools, which will be discussed in details later. For this purpose, we rely on lattice QCD results from Ref. [92], presented in Ref. [3], which provide non-perturbative relations between the high energy parameters Λ_D and m_{q_D}, and the low energy parameters m_{π_D} and m_{ρ_D}, or r_m. This allows us to connect the two regimes and guide us in setting the simulation parameters for our studies. The relations are given by

$$\Lambda_D = \frac{5}{12} m_{\pi_D} \sqrt{r_m^2 - 1.5}, \quad m_{q_D} = \frac{4}{121} \frac{{m_{\pi_D}}^2}{\Lambda_D}. \tag{4.25}$$

Now, for the portal between the dark sector and the SM, we will take two different approaches. For the chapter 5, we will remain agnostic about the nature of the portal, and only consider the four fundamental parameters described above. This is because we are mainly interested in the cosmological implications of the dark sector, and the details of the portal do not significantly affect our results. In that case, we will only have the four fundamental parameters described above.

However, for the accelerator phenomenology studies in chapter 6, we need to be more specific about the portal, as it will directly impact the production and decay of dark mesons at colliders. In that case, we will consider the $U(1)'$ case as introduced earlier, which will naturally give rise to additional free parameters in our theory. These are the mass of the new mediator, $m_{Z\prime}$, and the strength of the kinetic mixing to the SM fermions, κ. The coupling strength of the dark quarks and the Z' can be set to $e_D = 1$ without loss of generality.

4.2. Phenomenology of the dark sector

In this section, we explore the phenomenological implications of the strongly interacting dark sector described in the previous sections. We will focus on three key aspects: the possibility of pionic dark matter, the behavior of long-lived vector mesons, and the phenomenon of dark showers. These topics will help us understand the potential observational signatures and experimental constraints of the dark sector, as well as its relevance to cosmology and particle physics, as will be explored further in depth in the next chapters.

4.2.1. Pionic dark matter

Dark pions have emerged as promising dark matter candidates within the framework of strongly interacting dark sectors. As they are electrically neutral, exhibit self-interactions, and posses masses in the sub-GeV to GeV range, they are well-suited to account for the observed dark matter abundance while simultaneously addressing small-scale structure challenges in cosmology due to its self-interactions [93], all while evading current direct detection constraints. In what follows, we focus on two crucial aspects that determine their viability: their stability and the mechanisms governing their relic abundance.

These discussions are in the context of a thermal relic. In the theory we consider, we have interactions between the dark sector and the SM - albeit suppressed as to not violate constraints - and we therefore assume that the dark sector was in thermal equilibrium with the Standard Model in the early universe, and decoupled at some early time when the interactions became too inefficient to maintain equilibrium. Thus, the dark pions are thermal relics, and their relic abundance are set by a freeze-out process.

Stability of dark pions

In subsection 4.1.2, we introduced a $U(1)'$ gauge symmetry, under which the dark quarks are charged. This means that the dark mesons will also carry this dark charge. For example, in an $N_{f_D} = 2$ scenario with dark quark charges $+1$ and -1, the dark pions will have charges $+2$, 0, and -2. The charged dark pions, ${\pi_D}^{\pm}$, will be stable, as there are no lighter states with the same dark charge that they can decay into. The neutral dark pion, ${\pi_D}^0$, however, may or may not be stable, depending on the specific choice of dark quark charges and the presence of additional symmetries in the dark sector, and the dark sector cosmology is incredibly sensitive to their lifetime.

It turns out that if the ${\pi_D}^0$ decays into SM particles relatively fast, they can transfer energy between the dark sector and the SM at a rapid rate, which leads to delay or elimination of freeze-out processes and therefore a suppressed relic abundance. In that case, the dark pions cannot account for the observed dark matter abundance and lose their appeal as dark matter candidates. On the other hand, if the ${\pi_D}^0$ decays too slowly, they may disrupt BBN by injecting electromagnetic or hadronic energy, altering the primordial abundance of elements [94, 95]. They may also leave imprints in the CMB anisotropy, which are tightly constrained by observations [94, 96]. Therefore, for the dark pions to be viable dark matter candidates, they must be stable on cosmological timescales.

The stability of π_D^0 may be ensured by imposing an additional symmetry in the dark sector. One such symmetry is G-parity, defined as

$$G \equiv C \times \mathbb{Z}_2 \times U_q, \tag{4.26}$$

where C is the charge conjugation operator, $\mathbb{Z}_2$ is a discrete symmetry that transforms $Z'_\mu \to -Z'_\mu$, and $U_q \in SU(N_{f_D})$ is a unitary transformation that acts on the dark quark fields as $U_q^\dagger Q_D U_q q_D = -Q_D^T$ [87]. For the symmetry to hold, we need to make some assumptions on our dark sector, namely that

- the dark quarks are mass-degenerate, i.e. $M_{q_D} = m_{q_D} \times \mathbb{1}$.
- the dark quark charges are chosen such that the dark sector does not have anomalous terms [87, 97], meaning that $\mathrm{Tr}(Q_D) = 0$ and $Q_D^2 = \mathbb{1}$.

These conditions can only be fulfilled for even N_{f_D}. Under these assumptions, the dark pions can be classified as either G-even or G-odd, depending on their transformation properties under the G-parity operation. The neutral pion, ${\pi_D}^0$, is G-odd, and as a result, the decay of ${\pi_D}^0$ into SM particles is forbidden by G-parity conservation, ensuring its stability over cosmological timescales.

A caveat to this is that the G-parity symmetry can be broken by higher-dimensional operators, which may arise from physics at a higher energy scale. This can be realised by a dimension five operator giving rise to $\pi_D^0 \to \gamma\gamma$ decays in a UV theory including gravity [98].

To conclude, the stability of the dark pions can be debated in a model-specific framework. Nonetheless, we will remain as model-independent as possible in this thesis, and simply assume that both the charged and neutral dark pions are stable on cosmological timescales. This allows us to explore the phenomenology of the dark sector without being tied to a specific model.

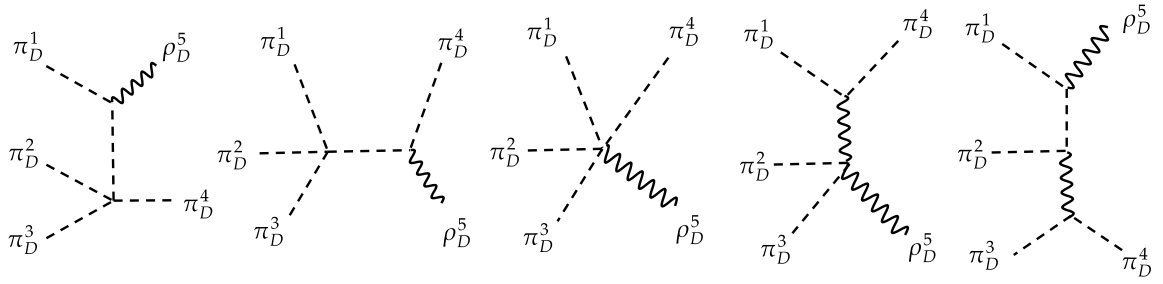

Figure 4.1.: Representative Feynman diagrams for the $3\pi_D \to \rho_D + \pi_D$ process.

Relic abundance of dark pions

We now turn to the mechanisms that determine the relic abundance of dark pions in the early universe. As mentioned earlier, we consider the dark pions to be thermal relics, and their abundance is set by a freeze-out process. It is not straightforward what processes are responsible for the freeze-out, as the simple $2\pi_D \to 2\text{SM}$ process would require relatively strong couplings between the dark sector and the SM to be efficient enough to deplete the dark pions to the observed relic abundance. This would be in tension with constraints from e.g. direct detection experiments and CMB data [55]. Instead, we must consider number-changing processes within the dark sector itself. Some of the proposed processes and their implications were discussed in section 3.3.

In this work, we propose another scenario, where the dark rho mesons ρ_D is relatively light, specifically, we consider the regime where $1.45 < m_{\rho_D} < 2m_{\pi_D}$. This is expected if the dark quarks mass is comparable to the dark confinement scale, and is consistent with the validity of chiral perturbation theory, as discussed in subsection 4.1.3. The light ρ_D opens up the $3\pi_D \to \rho_D\pi_D$ channel, contributing to the depletion of dark pions. We deduced this interaction from the dark chiral Lagrangian in Equation 4.14, and the Feynman diagrams of this process can be seen in Figure 4.1. As we will show in chapter 5, this process is dominant over the $3\pi_D \to 2\pi_D$ process for $N_{f_D} \geq 3$, leading to a significantly more effective depletion of the dark pion abundance, which allows for lower self-interactions, evading the Bullet Cluster constraints. This mechanism is also valid for $N_{f_D} = 2$, as it does not rely on the WZW term. As discussed earlier, this case is particularly interesting due to the stability of the dark pions.

The ρ_D produced in the $3\pi_D \to \rho_D\pi_D$ process will subsequently decay into SM particles via the mixing with the Z', as discussed in subsection 4.2.2, thus transferring energy from the dark sector to the SM, avoiding overheating of the dark sector.

4.2.2. Long-lived vector mesons

In the scenario where a massive Z' boson is introduced with mixing to the Standard Model (SM) hypercharge, the neutral dark rho meson (${\rho_D}^0$) acquires couplings to SM fermions, as we saw in subsection 4.1.2. Consequently, the ${\rho_D}^0$ can decay into SM fermions. Since we assume $m_{\rho_D} < 2m_{\pi_D}$, this is the only kinematically allowed decay channel, making it the dominant mode.

The decay width of ${\rho_D}^0$ into SM leptons is given by [86]:

$$\Gamma({\rho_D}^0 \to \ell^+\ell^-) = \frac{1}{3\pi g^2_{\pi_D\rho_D}} \frac{{m_{\rho_D}}^5}{\Lambda^4} \left(1 + 2\frac{m_\ell^2}{m_{\rho_D}^2}\right) \sqrt{1 - 4\frac{m_\ell^2}{m_{\rho_D}^2}}, \tag{4.27}$$

under the assumption that $m_{\rho_D} \ll m_{Z'}$. Here, m_ℓ is the mass of the lepton ℓ, and Λ is the suppression scale defined in Equation 4.22. The ${\rho_D}^0$ can also decay into SM quark and

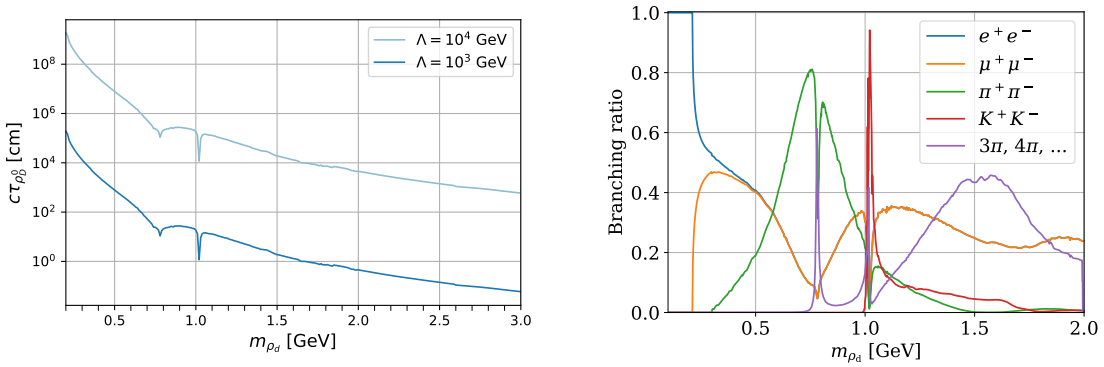

Figure 4.2.: Left: Lifetime of the neutral dark rho meson, ${\rho_D}^0$, as a function of its mass, m_{ρ_D}, for different values of the suppression scale, Λ. Right: Branching ratios of the ${\rho_D}^0$ into various SM lepton pairs and hadrons as a function of its mass, from Ref. [86].

anti-quark pairs, however, for low m_{ρ_D} ($\lesssim 2$ GeV) and around QCD resonances, it is more appropriate to consider decays into hadrons. We can relate the decay width into hadrons to the decay width into muons via the ratio $R(\sqrt{s})$ the following way:

$$\Gamma({\rho_D}^0 \to \text{hadrons}) = \Gamma({\rho_D}^0 \to \mu^+\mu^-) \cdot R(\sqrt{s}), \tag{4.28}$$

where $R(\sqrt{s})$ represents the ratio of the cross sections $\sigma(e^+e^- \to \text{hadrons})/\sigma(e^+e^- \to \mu^+\mu^-)$ mediated by an off-shell photon at a center-of-mass energy $\sqrt{s}$, and is enhanced near relevant QCD resonances [10].

The total decay width of the ${\rho_D}^0$ is then given by the sum of the decay widths into all kinematically allowed SM fermions:

$$\Gamma_{{\rho_D}^0} = \sum_{\ell} \Gamma({\rho_D}^0 \to \ell^+\ell^-) + \Gamma({\rho_D}^0 \to \text{hadrons}), \tag{4.29}$$

where the sum runs over all leptons ℓ for which $m_{\rho_D} > 2m_\ell$.

The lifetime of the ${\rho_D}^0$ is inversely proportional to its decay width:

$$c\tau_{{\rho_D}^0} = \frac{1}{\Gamma_{{\rho_D}^0}}. \tag{4.30}$$

The lifetime of the ${\rho_D}^0$ can vary significantly depending on the values of m_{ρ_D} and Λ. In Figure 4.2 (left), we plot the lifetime of the ${\rho_D}^0$ as a function of its mass for two different values of the suppression scale Λ, illustrating the shift in lifetime when we shift Λ. We see that the lifetime can range from sub-centimeter to hundreds or even thousands of meters, depending on the parameters.

For instance, for sub-GeV m_{ρ_D} and $\Lambda \sim 1$ TeV, the ${\rho_D}^0$ can have a lifetime of $\sim \mathcal{O}(1-100)$ meters, making it potentially long-lived on the scales of high energy experiment. This opens up the possibility of observing displaced vertices in accelerator experiments, which can serve as a distinctive signature of the dark sector.

Figure 4.2 (right, from Ref. [86]) displays the branching ratios of the ${\rho_D}^0$ into various Standard Model (SM) final states as a function of its mass. At low masses, the decay is predominantly into electrons, and into muons once $m_{\rho_D} > 2m_\mu$. As the mass increases, hadronic final states become significant. Distinct resonance structures corresponding to the SM mesons ρ^0 ($\to \pi^+\pi^-$), ω ($\to K^+K^-$), and ϕ ($\to 3\pi$) are visible, arising from mixing between the ${\rho_D}^0$ and the SM neutral vector mesons.

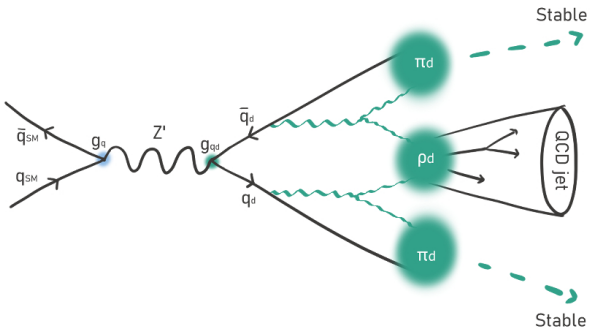

Figure 4.3.: A dark shower event at e.g. the LHC, initiated by a Z' boson produced in a high energy SM particle collision. The Z' boson decays into a dark quark and anti-quark pair, which subsequently undergo a dark parton shower, leading to the production of multiple dark mesons. The dark mesons can be stable or can decay into SM particles via the Z' portal, possibly initiating a SM QCD jet. Here, g_q and g_{q_D} are the couplings of the Z' to SM quarks and dark quarks, respectively.

4.2.3. Dark showers

The strong nature of the interactions in the dark sector has a crucial implication for high energy processes involving dark mesons; it leads to the phenomenon of *dark showers*. This is a process analogous to the parton showers in QCD, where high energy quarks and gluons are able to produce additional particles, leading to a cascade of dark particles in high energy systems.

This can be understood e.g. through the Lund string model, where the strong interactions between the dark quarks and gluons lead to the formation of color flux tubes, which can break and produce additional quark-antiquark pairs under the assumption of sufficient energy. This process continues until the energy of the system falls below the dark confinement scale, at which point the dark quarks and gluons confine into mesons and hadrons. The result is a high multiplicity of hadrons produced in a single event. This is, however, not the only way we can understand parton showers. An alternative approach is the clustering model, where the partons are grouped into clusters based on their kinematic properties, and these clusters then hadronize into mesons.

Since we assume there exists a portal between the dark sector and the SM, dark quark and anti-quark pairs can be produced in high energy collisions of SM particles, such as at the LHC. The dark quarks can then undergo a dark parton shower, leading to the production of a large number of dark mesons in a single event. Depending on the details of the dark sector, some of these dark mesons may be stable and escape the detector, while others may decay back into SM particles through the portal and leave visible signatures. This process is illustrated in Figure 4.3. This is a distinctive feature of strongly interacting dark sectors, and can lead to a rich phenomenology that can be probed experimentally.

The phenomenology of dark showers is quite diverse, depending on the specifics of the model. Ref. [3] provides a comprehensive overview also listing current benchmarks. Here, we will briefly summarize on four different ways in which dark showers can manifest, and how they can be probed experimentally.

An important quantity in the context of dark showers is the variable known as r_{inv}. This is the ratio of stable dark mesons to all dark mesons within the dark shower;

$$r_{\text{inv}} = \frac{N_{\text{stable dark mesons}}}{N_{\text{all dark mesons}}}. \tag{4.31}$$

A few comments are in order. First, unstable dark mesons only refers to SM-decaying dark mesons. A dark meson decaying within the dark sector is considered stable in this context. Second, stable means stable within the scale of the detector. A dark meson that decays past the detector scale is thus still considered stable.

Clearly, this variable fluctuates event-by-event, as it depends on the exact dynamics of each dark shower. Nonetheless, it is possible to define an expected mean value $\langle r_{\text{inv}} \rangle$ based on the specifics of the model under consideration. This mean value can be used to characterize the dark shower and its phenomenology. We can identify three different scenarios, based on the value of $\langle r_{\text{inv}} \rangle$:

- **Small values of $\langle r_{\text{inv}} \rangle$ (~ 0)**: This scenario corresponds to a situation where the dark showers are dominated by the production of unstable dark mesons that decay into SM particles. In this case, the dark showers would produce a large number of SM particles, leading to highly visible signatures in collider experiments. These signatures are known as *dark jets*, and are generally characterized by jets with higher multiplicities and broader distribution of particles (fat jets) than typical QCD jets, due to the fact that there is a dark shower preceding the QCD shower.

- **Large values of $\langle r_{\text{inv}} \rangle$ (~ 1):** Conversely, large values mean that the dark sector is dominated by stable dark mesons, and therefore very few or no SM particles are produced as a result of the dark showers. In this case, the dark showers would be invisible to collider experiments, unless they are produced in connection with initial state radiation (ISR) processes. This would lead to events with large missing energy in opposite direction of the ISR jet, as the stable dark mesons would escape detection. This signature is known as *mono-jet* events, and is a common signature in many dark matter models, especially WIMP models, as discussed in section 3.3.

- **Intermediate values of $\langle r_{\text{inv}} \rangle$:** Finally, intermediate values of $\langle r_{\text{inv}} \rangle$ correspond to a situation where the dark showers produce a mix of stable and unstable dark mesons. In this case, the dark showers would produce both SM particles and stable dark mesons, leading to truly novel signatures that are generally characterized by back-to-back jets with significant missing energy aligned with one of the jets. This is due to the fact that the initial dark quark and anti-quark are boosted in opposite directions, whereafter a the dark shower leads to multiple decays into SM particles and gives rise to SM jets in both directions. However, it is unlikely that these jets contain the same number of SM particles, or the same amount of energy in the visible sector, and thus we find missing energy along the more invisible jet. These signatures are known as *semi-visible jets*. A particularly interesting aspect of semi-visible jets is that they can evade many of the traditional searches for dark matter, as events with a small angle between the missing energy and the jet are often discarded in order to reduce backgrounds and misreconstructed jets. Additionally, they may not appear in traditional bump-hunt searches, as the semi-visibility distorts the invariant mass distribution. This means that semi-visible jets can be a hidden channel for discovering dark matter at colliders [99].

Another key characteristic of dark showers is the lifetime of the unstable dark mesons. If the unstable dark mesons decay promptly, the phenomenology will fall into one of the three categories described above. However, if the unstable dark mesons are long-lived, this can lead to displaced vertices. In a very high-energy system, like at the LHC, we do not only expect

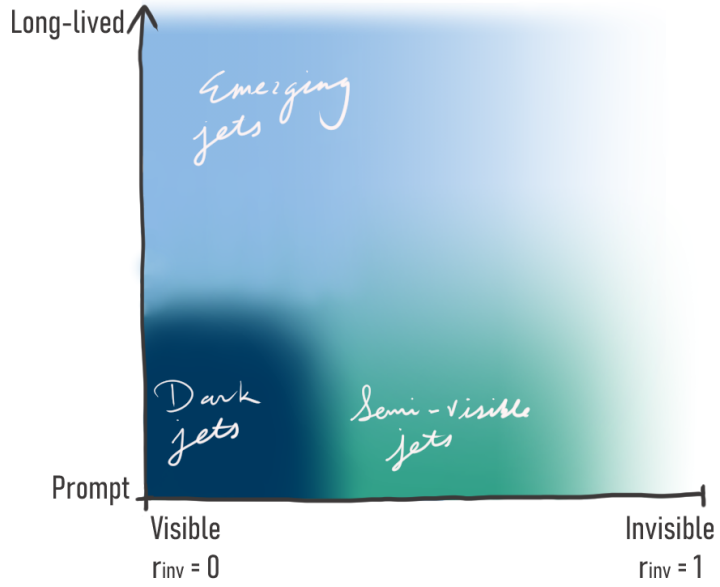

Figure 4.4.: An illustrative overview of the different signatures of dark showers, depending on the value of r_{inv} and the lifetime of SM-decaying the dark mesons.

one or a few displaced vertices, but rather a large number of them, as the dark showers can produce a high multiplicity of long-lived dark mesons. This leads to another novel signature, known as *emerging jets*.

A summary of the different signatures of dark showers is given in Figure 4.4. Displaced vertex signatures will be explored in more detail in chapter 6, while chapter 7 will touch upon the phenomenology of dark showers with prompt decays.

4.3. Simulating the dark sector

To study the accelerator phenomenology of the strongly interacting dark sector, we need to simulate the production and decay of dark mesons in high-energy collisions. To this end, we utilize two Monte Carlo event generators that are able to model the interactions we are studying; Pythia 8 [100] and MadGraph_aMC@NLO [101]. While Pythia 8 includes a Hidden Valley module that can simulate both the production of the dark quark and anti-quark pair in a collision, and the subsequent showering and hadronization process, the implementation of the dark sector parameters is not as transparent as we would like. Therefore, for the chapter 6, we use MadGraph_aMC@NLO to simulate the production of the dark quark and anti-quark pair, which we then feed into Pythia 8 for showering and hadronization. In this section, we will briefly describe how we use these two tools to simulate the dark sector.

4.3.1. MadGraph

To simulate the production of dark quark and anti-quark pairs in high-energy collisions, we use MadGraph_aMC@NLO (hereafter referred to as MadGraph) [101]. This tool allows us to define a custom model for the dark sector, including the relevant particles and interactions, and then generate events for specific processes - providing full transparency. We use the Universal FeynRules Output (UFO) format [102] to define our model, which includes

the dark quarks, the Z' mediator, and their interactions with the Standard Model particles. We then use MadGraph to generate events for the process $pp \to Z' \to q_D\bar{q}_D$. The generated events are then exported in the Les Houches Event (LHE) format, which can be read by Pythia 8 for further processing.

When generating events in MadGraph, we need to set several parameters that define the kinematics of the collisions and the properties of the particles involved. The key parameters include the center-of-mass energy of the collisions $\sqrt{s}$, the number of dark colors N_{c_D} and flavors N_{f_D}, the current dark quark mass m_{q_D}, the Z' mediator mass $m_{Z'}$ and width $\Gamma_{Z'}$, the couplings between the dark sector and the SM, i.e. both e_D and κ, and the dark pion mass, m_{π_D}.

4.3.2. Pythia 8

The dark showering and hadronization process is simulated with the Hidden Valley module in Pythia 8 [100]. This module allows us to define a hidden sector with its own $SU(N_{c_D})$ gauge group, particles, and interactions, and then simulate the production and decay of particles in this sector.

It is possible to produce the initial dark quark and anti-quark pair directly in Pythia 8 via the Z' mediator in $pp \to Z' \to q_D\bar{q}_D$. We will use this method for some of the models in chapter 7. In this case, the inputs include the center-of-mass energy of the collisions $\sqrt{s}$, the number of dark colors N_{c_D} and flavors N_{f_D}, the Z' mediator mass $m_{Z'}$ its width $\Gamma_{Z'}$, as well as the dark confinement scale Λ_D, the constituent dark quark mass which we can define as $m_{q_D} + \Lambda_D$ [3], the dark meson masses m_{π_D} and m_{ρ_D}, and additional parameters that control the showering and hadronization process.

Some of these parameters are very specific to the Lund string model and the implementation in Pythia 8, and their descriptions are outside the scope of this work. These are the `HiddenValley:aLund` and `HiddenValley:bLund` parameters. It was noted in Ref. [3] that the effects of these parameters on the phenomenology have not been investigated in detail. While there are no official recommendations for these parameters, we follow internal suggestions and set them to 0.3 and 0.087, respectively.

Other parameters that control the showering and hadronization process include the Hidden Valley settings `probVector`, which sets the probability of producing vector mesons over pseudo-scalar mesons in the hadronization process, and `probKeepEta1`, which controls the suppression of dark η' meson production. We have clear expectations of what the ratios of vector to pseudo-scalar mesons should be in two special cases. These are 1) when $m_{\rho_D} = m_{\pi_D}$, counting spin degrees of freedom suggests that vector mesons should be produced three times as often as pseudo-scalar mesons, and 2) when $m_{\rho_D} \approx 5.7 m_{\pi_D}$, we expect approximately equal production of vector and pseudo-scalar mesons, as this is the case for SM QCD. In Ref. [103], a fit to these values depending on the mass ratio r_m was performed, resulting in values of $\sim 0.68 - 0.71$. for $r_m \sim 1.5 - 1.9$. For `probKeepEta1`, we set it to 0, effectively suppressing the production of dark η' mesons, as we expect them to be significantly heavier than the dark pions and rhos, and thus not relevant for our phenomenology.

It should also be noted that we set `HiddenValley:separateFlav` to `on`, which allows for different dark quark flavors to be treated separately during the showering and hadronization process. However, since we do not simulate the decays of the dark mesons in Pythia 8, this is not expected to have an impact on our results.

CHAPTER 5

Studies of a Light Vector Meson Model in the Early Universe

In Chapter 4 we saw how the dark pions of a strongly interacting dark sector can be stabilized, and thus become a viable dark matter candidate. We introduced how a light vector meson, ρ_D with $m_{\rho_D} < 2m_{\pi_D}$, leads to $3\pi_D \to \pi_D\rho_D$ interactions that can contribute to the depletion of the dark pion abundance in the early universe.

The classical SIMP scenario [21, 55] relies on the Wess-Zumino-Witten (WZW) term to provide $3\pi_D \to 2\pi_D$ interactions that can deplete the dark pion abundance in the early universe. This term is only present if the number of flavors, N_{f_D}, is greater than or equal to 3, thus it is not present for $N_{f_D} = 2$. The presence of a light vector meson changes this picture: it introduces $3\pi_D \to \pi_D\rho_D$ interactions that remain possible even for $N_{f_D} = 2$. Consequently, a dark sector with only two flavors of dark quarks can still yield a viable dark matter candidate.

Moreover, the additional depletion channel broadens the allowed range of dark pion masses, as the $3\pi_D \to \pi_D\rho_D$ process plays a significant role in freeze-out. In sections 5.1 and 5.2, we will analyze this mechanism in detail by solving the Boltzmann equation, explicitly incorporating the $3\pi_D \to \pi_D\rho_D$ interaction.

Throughout this chapter, we will assume that the dark sector remains in thermal equilibrium with the SM. For this, we make the assumption that the ρ_D mixes with SM fermions, the strength of which is parameterized by a coupling, g_ℓ, although we do not specify the exact mechanism of this mixing. Thermal equilibrium is then maintained through energy and entropy transfer by the decay and production of the ρ_D to and from SM fermions. However, this assumption introduces a new depletion mechanism, namely the $\pi_D\pi_D \to \bar{f}f$ via an s-channel ρ_D. In section 5.3, we will estimate the contribution of this process to the freeze-out of dark pions and show that it is negligible for a large range of the coupling, g_ℓ, where the dark sector remains in thermal equilibrium with the SM.

Finally, we will consider the self-interactions of the dark pions, that can be compared to constraints from the Bullet Cluster observations. In section 5.4, we will calculate the self-interaction cross section of dark pions and show that the Bullet Cluster constraints can be evaded for this model with varying N_{c_D}, N_{f_D} and r_m, while successfully reproducing the dark matter relic abundance.

5.1. The Boltzmann equation for the $3\pi_D \to \pi_D\rho_D$ process

We introduced the Boltzmann equation in section 3.2, where we saw that the time evolution of the number density of a particle species is given by the Liouville operator on the left-hand side and a collision term on the right-hand side. While we previously considered a collision term arising from 2DM $\to$ 2SM interactions, we will now derive the appropriate collision term for the $3\pi_D \to \pi_D\rho_D$ process.

We consider the distribution function of the dark pions, $f_{\pi_D{}^i}(p,t)$, and dark rho, $f_{\rho_D{}^5}(p,t)$, where p is the momentum of the particle and t is time, and i goes from 1 to 4, counting the 3 dark pions in the initial state and the one in the final state, as illustrated in Figure 4.1. The distribution functions for the pions are the same, i.e. $f_{\pi_D{}^1}(p,t) = f_{\pi_D{}^2}(p,t) = f_{\pi_D{}^3}(p,t) = f_{\pi_D{}^4}(p,t) = f_{\pi_D}(p,t)$, but for now we will continue to write the subscript to keep better track of them. We track the evolution of the distribution function of one of the dark pions, e.g. $\pi_D{}^1$, as it undergoes the $3\pi_D \to \rho_D\pi_D$ and inverse $\rho_D\pi_D \to 3\pi_D$ interactions. In the direction $3\pi_D \to \pi_D\rho_D$, the $f_{\pi_D{}^i}(p,t)$ distribution decreases proportional to the amplitude of the interaction, $|\mathcal{M}|^2_{3\pi_D\to\pi_D\rho_D}$, the density of the initial state particles, $f_{\pi_D{}^1}f_{\pi_D{}^2}f_{\pi_D{}^3}$, and a Bose enhancement factor;

$$\Delta^-(f_{\pi_D{}^1}) = |\mathcal{M}_{3\pi_D\to\pi_D\rho_D}|^2 f_{\pi_D{}^1}f_{\pi_D{}^2}f_{\pi_D{}^3}(1+f_{\pi_D{}^4})(1+f_{\rho_D{}^5}). \tag{5.1}$$

The increase in $f_{\pi_D{}^1}$ is by similar arguments given by

$$\Delta^+(f_{\pi_D{}^1}) = |\mathcal{M}_{\pi_D\rho_D\to 3\pi_D}|^2 f_{\pi_D{}^4}f_{\rho_D{}^5}(1+f_{\pi_D{}^1})(1+f_{\pi_D{}^2})(1+f_{\pi_D{}^3}). \tag{5.2}$$

We assume $|\mathcal{M}_{3\pi_D\to\pi_D\rho_D}|^2 = |\mathcal{M}_{\pi_D\rho_D\to 3\pi_D}|^2$ and denote it $|\mathcal{M}|^2$, and that the distribution functions for all the particles are very small such that $(1+f) \approx 1$. We then find that the change in the distribution function of the dark pion $\pi_D{}^1$ is given by $\Delta^+(f_{\pi_D{}^1}) - \Delta^-(f_{\pi_D{}^1})$ integrated over all possible momenta, where we ensure energy conservation with a delta function over the four momenta of the incoming particles minus that of the outgoing particles. This gives us the collision term for the Boltzmann equation;

$$\begin{aligned} C[f_{\pi_D{}^1}] = \frac{1}{2E_{\pi_D{}^1}} \int d\Pi_{\pi_D{}^2} d\Pi_{\pi_D{}^3} d\Pi_{\pi_D{}^4} d\Pi_{\rho_D{}^5} (2\pi)^4 \delta^{(4)}(P_1+P_2+P_3-P_4-P_5) \\ \times \sum_{\text{spins}} |\mathcal{M}|^2 \left(f_{\pi_D{}^4}f_{\rho_D{}^5} - f_{\pi_D{}^1}f_{\pi_D{}^2}f_{\pi_D{}^3} \right), \end{aligned} \tag{5.3}$$

where $d\Pi = \frac{d^3p}{(2\pi)^3 2E}$, P_i is the four-momentum of particle i, and we sum over the spins of the particles. If we can assume that the ρ_D distributions follows its equilibrium distributions, i.e. $f_{\rho_D} = e^{-E/T}$ we can replace

$$f^{\text{eq}}_{\rho_D{}^5} = e^{-(E_5)/T} = e^{-(E_1+E_2+E_3-E4)/T} = f^{\text{eq}}_{\pi_D{}^1} f^{\text{eq}}_{\pi_D{}^2} f^{\text{eq}}_{\pi_D{}^3} (f^{\text{eq}}_{\pi_D{}^4})^{-1} \tag{5.4}$$

where we know that $E_5 = E_1 + E_2 + E_3 - E_4$ from energy conservation. Now we use that $f_{\pi_D{}^i} = f_{\pi_D}$, so we can write

$$f_{\pi_D{}^4}f_{\rho_D{}^5} - f_{\pi_D{}^1}f_{\pi_D{}^2}f_{\pi_D{}^3} = f_{\pi_D}(f^{\text{eq}}_{\pi_D})^2 - (f_{\pi_D})^3. \tag{5.5}$$

We insert this into Equation 5.3

$$\begin{aligned} C[f_{\pi_D}] = \frac{1}{S_I \cdot S_F} \frac{1}{2E_{\pi_D}} \int d\Pi_{\pi_D{}^2} d\Pi_{\pi_D{}^3} (f_{\pi_D}(f^{\text{eq}}_{\pi_D})^2 - (f_{\pi_D})^3) \\ \times \int d\Pi_{\pi_D{}^4} d\Pi_{\rho_D{}^5} (2\pi)^4 \delta^{(4)}(P_1+P_2+P_3-P_4-P_5) \sum_{\text{spins}} |\mathcal{M}|^2, \end{aligned} \tag{5.6}$$

where we have also performed permutations over the initial and final states, which introduces a factor of $1/S_{I,F} = 1/N_{\text{identical}}!$ for N number of identical particles in the initial and final state. For this process, $S_I = 3!$ and $S_F = 1$.

To get the desired form of the Liouville operator for the Boltzmann equation, as seen in section 3.2, we integrated over the 3-momenta of the dark pion and multiplied by $\frac{1}{(2\pi)^3}$. We do the same for the collision term, and we get

$$\begin{aligned}\frac{1}{(2\pi)^3}\int d^3pC[f_{\pi_D}] = \frac{1}{S_I\cdot S_F}\int d\Pi_{\pi_D{}^1}d\Pi_{\pi_D{}^2}d\Pi_{\pi_D{}^3}(f_{\pi_D}(f^{\text{eq}}_{\pi_D})^2 - (f_{\pi_D})^3)\\ \times\int d\Pi_{\pi_D{}^4}d\Pi_{\rho_D{}^5}(2\pi)^4\delta^{(4)}(P_1+P_2+P_3-P_4-P_5)\sum_{\text{spins}}|\mathcal{M}|^2.\end{aligned} \tag{5.7}$$

Before we put this together with the Liouville operator, we rewrite the distribution functions in terms of the number densities, using $\frac{n}{n^{\text{eq}}} = \frac{f}{f^{\text{eq}}}$, the following way:

$$\begin{aligned}f_{\pi_D}(f^{\text{eq}}_{\pi_D})^2 - (f_{\pi_D})^3 =& \frac{f_{\pi_D}(f^{\text{eq}}_{\pi_D})^2 - (f_{\pi_D})^3}{(f^{\text{eq}}_{\pi_D})^3}\cdot(f^{\text{eq}}_{\pi_D})^3\\ =&(\frac{n_{\pi_D}}{n^{\text{eq}}_{\pi_D}} - \frac{n^3_{\pi_D}}{(n^{\text{eq}}_{\pi_D})^3})\cdot(f^{\text{eq}}_{\pi_D})^3 = ((n^{\text{eq}}_{\pi_D})^2 n_{\pi_D} - n^3_{\pi_D})\cdot\frac{(f^{\text{eq}}_{\pi_D})^3}{(n^{\text{eq}}_{\pi_D})^3}.\end{aligned} \tag{5.8}$$

Since the number density is related to the distribution function by

$$n^{\text{eq}}_{\pi_D} = \frac{g}{(2\pi)^3}\int d^3p f^{\text{eq}}_{\pi_D}, \tag{5.9}$$

where g is the number of degrees of freedom, which is 1 for the pions and will be omitted from here on, we can rewrite Equation 5.7 as

$$\begin{aligned}\frac{1}{(2\pi)^3}\int d^3pC[f_{\pi_D}] = ((n^{\text{eq}}_{\pi_D})^2 n_{\pi_D} - n^3_{\pi_D})\frac{1}{S_I\cdot S_F}\frac{1}{(n^{\text{eq}}_{\pi_D})^3}\int d\Pi_{\pi_D{}^1}d\Pi_{\pi_D{}^2}d\Pi^3_{\pi_D{}^3}(f^{\text{eq}}_{\pi_D})^3\\ \times\int d\Pi_{\pi_D{}^4}d\Pi_{\rho_D{}^5}(2\pi)^4\delta^{(4)}(P_1+P_2+P_3-P_4-P_5)\sum_{\text{spins}}|\mathcal{M}|^2.\end{aligned} \tag{5.10}$$

At this point we will simplify Equation 5.10 by recognizing that the entire term following the number densities is equal to the thermally averaged cross section times velocity squared[5], $\langle\sigma v^2\rangle$. This point will be elaborated further on in the next section. Thus, we arrive at the final collision term;

$$\frac{1}{(2\pi)^3}\int d^3pC[f_{\pi_D}] = ((n^{\text{eq}}_{\pi_D})^2 n_{\pi_D} - n^3_{\pi_D})\langle\sigma v^2\rangle_{3\pi_D\to\pi_D+\rho_D}. \tag{5.11}$$

Finally, putting this together with the Liouville operator, we arrive at the appropriate Boltzmann equation for the dark pion abundance;

$$\frac{dn_{\pi_D}}{dt} + 3Hn_{\pi_D} = \langle\sigma v^2\rangle_{3\pi_D\to\pi_D\rho_D}\left((n^{\text{eq}}_{\pi_D})^2 n_{\pi_D} - n^3_{\pi_D}\right), \tag{5.12}$$

In terms of the dimensionless yield, $Y_{\pi_D} = \frac{n_{\pi_D}}{s}$, we can rewrite Equation 5.12 as

$$\frac{dY}{dx} = \frac{s^2}{\tilde{H}x}\langle\sigma v^2\rangle_{3\pi_D\to\pi_D\rho_D}Y\left((Y^{\text{eq}})^2 - Y^2\right). \tag{5.13}$$

[5]The velocity referred to here is understood as the relative velocity between the three incoming π_D, the definition of which is discussed in e.g. Ref. [56].

5.1.1. Thermally averaged cross section

The thermally averaged cross section, $\langle\sigma v^2\rangle_{3\pi_D\to\pi_D\rho_D}$, can be derived from the general form as derived in Ref. [56]. For a process with 3 initial particles and 2 final particles it takes the form

$$\begin{aligned}\langle\sigma v^2\rangle_{3\pi_D\to\pi_D\rho_D} =&\frac{1}{(n^{\rm eq}_{\pi_D})^3}\frac{1}{S_I S_F}\int d\Pi_{\pi_D{}^1} d\Pi_{\pi_D{}^2} d\Pi_{\pi_D{}^3} (f^{\rm eq}_{\pi_D})^3 \\ &\times \int d\Pi_{\pi_D{}^4} d\Pi_{\rho_D{}^5} (2\pi)^4 \delta^{(4)}(P_1+P_2+P_3-P_4-P_5)\sum_{\rm spins}|\mathcal{M}|^2,\end{aligned} \tag{5.14}$$

We have 3 identical particles in the initial state and no identical particles in the final state so we can replace $S_I = 3! = 6$ and $S_F = 1$. The matrix element of the $3\pi_D \to \pi_D\rho_D$ process is independent of the momenta of the incoming particles, which means we can move it outside the integral. This is not generally the case for all types of interactions - for example the $3\pi_D \to 2\pi_D$ process mediated by the WZW term has a momentum-dependent matrix element [59], which carries through to the $\langle\sigma v^2\rangle$ in form of a dependence on x^{-2}, as seen in Equation 3.15. However, in our case, the amplitude $|\mathcal{M}|^2_{3\pi_D\to\pi_D\rho_D}$ approaches a constant in the non-relativistic limit and thus is independent of momenta. Noting that $d\Pi = \frac{d^3p}{(2\pi)^3 2E}$ and using Equation 5.9, we can rewrite the integrals over $p_{1,2,3}$ in Equation 5.14 and we get

$$\langle\sigma v^2\rangle_{3\pi_D\to\pi_D\rho_D} = \frac{1}{6}\sum_{\rm spins}|\mathcal{M}|^2\frac{1}{(2\pi)^2}\int dp_{\pi_D{}^4} dp_{\rho_D{}^5}\prod_{i=1}^{5}\frac{1}{2E_i}\delta^{(4)}(P_1+P_2+P_3-P_4-P_5). \tag{5.15}$$

The delta function $\delta^{(4)}(P_1+P_2+P_3-P_4-P_5)$ enforces both energy and momentum conservation and we can factorize it as:

$$\delta^{(4)}(P_1+P_2+P_3-P_4-P_5) = \delta(E_1+E_2+E_3-E_4-E_5)\delta^{(3)}(\vec{p}_1+\vec{p}_2+\vec{p}_3-\vec{p}_4-\vec{p}_5). \tag{5.16}$$

In the non-relativistic limit, the incoming particles have negligible momenta ($\vec{p}_1, \vec{p}_2, \vec{p}_3 \approx 0$), so the outgoing momenta must satisfy:

$$\vec{p}_4 + \vec{p}_5 = 0 \quad \Rightarrow \quad \vec{p}_5 = -\vec{p}_4. \tag{5.17}$$

Thus, when we can carry out the integral over $p_{\rho^5_D}$ we get a factor of $4\pi p^2_{\pi^4_D}$, and we arrive at

$$\langle\sigma v^2\rangle_{3\pi_D\to\pi_D\rho_D} = \frac{1}{6}\sum_{\rm spins}|\mathcal{M}|^2\frac{1}{(2\pi)^2}\int dp_{\pi_D{}^4} 4\pi p^2_{\pi_D{}^4}\prod_{i=1}^{5}\frac{1}{2E_i}\delta(E_1+E_2+E_3-E_4-E_5). \tag{5.18}$$

In the non-relativistic limit, we can also write the energies of the incoming pions as $E_1 = E_2 = E_3 = m_{\pi_D}$. We write the outgoing π_D and ρ_D energies as $E_4 = \sqrt{p^2_{\pi_D{}^4} + m^2_{\pi_D}}$ and $E_5 = \sqrt{p^2_{\rho_D{}^5} + m^2_{\rho_D}}$. In the center of mass frame $p^2_{\pi_D{}^4} = p^2_{\rho_D{}^5}$ so we can transform the delta function to

$$\delta(E_1+E_2+E_3-E_4-E_5) = \delta(3m_{\pi_D} - \sqrt{p^2_{\pi_D{}^4}+m^2_{\pi_D}} - \sqrt{p^2_{\pi_D{}^4}+m^2_{\rho_D}}). \tag{5.19}$$

We define the value at which the term inside the delta function is zero as $p_{\pi_D{}^4} - \tilde{p}_{\pi_D{}^4}$ with

$$\begin{aligned}\tilde{p}_{\pi_D{}^4} &= \frac{\sqrt{64{m_{\pi_D}}^4 - 20{m_{\pi_D}}^2{m_{\rho_D}}^2 + {m_{\rho_D}}^4}}{6m_{\pi_D}} = \frac{{m_{\pi_D}}^2}{6m_{\pi_D}}\sqrt{64 - 20\frac{{m_{\rho_D}}^2}{{m_{\pi_D}}^2} + \frac{{m_{\rho_D}}^4}{{m_{\pi_D}}^4}} \\ &= \frac{m_{\pi_D}}{3}\sqrt{16 - 20\frac{{m_{\rho_D}}^2}{4{m_{\pi_D}}^2} + \frac{{m_{\rho_D}}^4}{4{m_{\pi_D}}^4}} = \frac{2m_{\pi_D}}{3}\sqrt{4 - 5\frac{{m_{\rho_D}}^2}{4{m_{\pi_D}}^2} + \frac{{m_{\rho_D}}^4}{4^2{m_{\pi_D}}^4}} \\ &= \frac{2m_{\pi_D}}{3}\sqrt{4 - 5y + y^2}\end{aligned} \tag{5.20}$$

where we have defined $y = \frac{{m_{\rho_D}}^2}{4{m_{\pi_D}}^2}$. Using the rule $\delta(f(x)) = \frac{1}{f'(x_{\text{root}})}\delta(x - x_{\text{root}})$, we can rewrite the delta function as

$$\begin{aligned}&\delta(3m_{\pi_D} - \sqrt{p^2_{\pi_D{}^4} + m^2_{\pi_D}} - \sqrt{p^2_{\pi_D{}^4} + m^2_{\rho_D}}) \\ &\qquad = \frac{\sqrt{\tilde{p}^2_{\pi_D{}^4} + {m_{\pi_D}}^2}\sqrt{\tilde{p}^2_{\pi_D{}^4} + {m_{\rho_D}}^2}}{\tilde{p}_{\pi_D{}^4}(\sqrt{\tilde{p}^2_{\pi_D{}^4} + {m_{\pi_D}}^2} + \sqrt{\tilde{p}^2_{\pi_D{}^4} + {m_{\rho_D}}^2})}\delta(p_{\pi_D{}^4} - \tilde{p}_{\pi_D{}^4}).\end{aligned} \tag{5.21}$$

We then use that this is only non-zero when $p_{\pi_D{}^4} = \tilde{p}_{\pi_D{}^4}$, so we can write our product over the energies in terms of $\tilde{p}_{\pi_D{}^4}$;

$$\prod_{i=1}^{5}\frac{1}{2E_i} = \frac{1}{8{m_{\pi_D}}^3}\frac{1}{2\sqrt{\tilde{p}^2_{\pi_D{}^4} + {m_{\pi_D}}^2}}\frac{1}{2\sqrt{\tilde{p}^2_{\pi_D{}^4} + {m_{\rho_D}}^2}}. \tag{5.22}$$

Inserting Equations 5.20, 5.21 and 5.22 into the expression for the thermally averaged cross section in Equation 5.18 and carrying out the integral over $p_{\pi_D{}^4}$, we get

$$\langle\sigma v^2\rangle_{3\pi_D\to\pi_D\rho_D} = \frac{|\mathcal{M}_{3\pi_D\to\pi_D\rho_D}|^2}{192\pi} \times \frac{2m_{\pi_D}/3\cdot\sqrt{4-5y+y^2}}{{m_{\pi_D}}^3(\sqrt{\tilde{p}^2_{\pi_D{}^4} + {m_{\pi_D}}^2} + \sqrt{\tilde{p}^2_{\pi_D{}^4} + {m_{\rho_D}}^2})}, \tag{5.23}$$

where the factor of 192 in the denominator comes from the $8\cdot 2\cdot 2\cdot 6$ from the denominators above and the identical particle factor discussed earlier. In the non-relativistic limit we can approximate the energies of the outgoing particles as $E_4 + E_5 \approx 3m_{\pi_D}$, so the last fraction above simplify to

$$\frac{2m_{\pi_D}/3\cdot\sqrt{4-5y+y^2}}{{m_{\pi_D}}^3(E_4+E_5)} = \frac{2\sqrt{4-5y+y^2}}{9{m_{\pi_D}}^3} \tag{5.24}$$

This gives us the final expression for the thermally averaged cross section:

$$\langle\sigma v^2\rangle_{3\pi_D\to\pi_D\rho_D} = \frac{|\mathcal{M}_{3\pi_D\to\pi_D\rho_D}|^2}{864\pi}\frac{\sqrt{4-5y+y^2}}{{m_{\pi_D}}^3}. \tag{5.25}$$

The squared amplitude $|\mathcal{M}_{3\pi_D\to\pi_D\rho_D}|^2$ is the sum of the five diagrams shown in Figure 4.1, and we use the FeynCalc [104–106] Mathematica package to calculate it. The result is

$$|\mathcal{M}|^2_{3\pi_D\to\pi_D\rho_D} = \frac{8m^4_{\pi_D}(1-y)(4-y)(\frac{\Gamma^2_{\text{th}}}{m^2_{\pi_D}} + 4y^2)(5N^4_{f_D}\frac{\Gamma^2_{\text{th}}}{m^2_{\pi_D}}(13y+2)^2 + 32(2Ay^2+2By+C))}{3f^6_{\pi_D}(\frac{\Gamma^2_{\text{th}}}{m^2_{\pi_D}} + 64)(2y+1)^2(9\frac{\Gamma^2_{\text{th}}}{m^2_{\pi_D}} + 64(1-y)^2)}, \tag{5.26}$$

with

$$A = \frac{(821N_{f_D}^4 - 168N_{f_D}^2 + 36)}{N_{f_D}(N_{f_D}^2 - 1)^2},$$
$$B = \frac{(245N_{f_D}^4 - 114N_{f_D}^2 + 36)}{N_{f_D}(N_{f_D}^2 - 1)^2},$$
$$C = \frac{(37N_{f_D}^4 - 30N_{f_D}^2 + 18)}{N_{f_D}(N_{f_D}^2 - 1)^2}. \tag{5.27}$$

The parameter $\Gamma_{\rm th}$ is the thermal width of the dark pions. It comes about from the interactions of the dark pions with the thermal plasma, leading to thermal self-energy corrections. The thermal width is exponentially suppressed at low temperatures, as there are not enough dark pions in the plasma to interact with. However, as m_{ρ_D} approaches $2m_{\pi_D}$, the thermal width increases slightly. We include this in our calculations by using the following approximation for the thermal width [1]:

$$\Gamma_{\rm th} = \frac{8\pi(N_{f_D}^2 - 1)}{x^2} e^{-x} m_{\pi_D}^3 \sigma_c \tag{5.28}$$

with σ_c being the cross section for pion-pion scattering in the non-relativistic limit. We will discuss this in further details in section 5.4, but for now we will just state that in the non-relativistic limit, it is given by

$$\sigma_{\rm c} \approx \frac{3}{64\pi} \frac{m_\pi^2}{f_\pi^4} (1 + \mathcal{O}(N_{f_D}^{-2})) \tag{5.29}$$

5.2. Numerical solution to the Boltzmann equation

We will need to solve Equation 5.13 numerically, and for this purpose we change variables to $W = \ln(Y)$. This is done because the yield Y varies over many orders of magnitude (Equation 5.13 is what is known as a numerically stiff equation), and instead, taking the logarithm of Y results in smaller variations and makes the numerical solution more stable. We can then rewrite Equation 5.13 as

$$\frac{dW}{dx} e^W = \frac{s^2}{\tilde{H}x} \langle \sigma v^2 \rangle_{3\pi_D \to \pi_D \rho_D} e^W \left(e^{2W_{\rm eq}} - e^{2W} \right) \Rightarrow$$
$$\frac{dW}{dx} = \frac{s^2}{\tilde{H}x} \langle \sigma v^2 \rangle_{3\pi_D \to \pi_D \rho_D} \left(e^{2W_{\rm eq}} - e^{2W} \right). \tag{5.30}$$

having used that

$$Y = e^W \quad \& \quad \frac{dY}{dx} = e^W \frac{dW}{dx}$$

When we insert the modified Hubble rate (Equation 3.12) into Equation 5.13 and replace $s = \frac{2\pi^2}{45} h T^3$ for one power of s, we can rewrite it as

$$\frac{dW}{dx} = \sqrt{\frac{90}{8\pi^3 g}} \frac{M_{\rm Pl}}{T^2} \left[1 + \frac{1}{3} \frac{\mathrm{d}(\ln\, h)}{\mathrm{d}(\ln\, \mathrm{T})} \right] \frac{2\pi^2}{45} h T^3 \frac{s}{x} \langle \sigma v^2 \rangle_{3\pi_D \to \pi_D \rho_D} e^W \left(e^{2W_{\rm eq}} - e^{2W} \right),$$
$$= \sqrt{\frac{\pi}{45}} M_{\rm Pl} \frac{h}{\sqrt{g}} \left[1 + \frac{1}{3} \frac{\mathrm{d}(\ln\, h)}{\mathrm{d}(\ln\, \mathrm{T})} \right] \frac{m_{\pi_D} s}{x^2} \langle \sigma v^2 \rangle_{3\pi_D \to \pi_D \rho_D} e^W \left(e^{2W_{\rm eq}} - e^{2W} \right), \tag{5.31}$$

where we have defined $\sqrt{g_\star}$ following Ref. [52] as:

$$\sqrt{g_\star} = \frac{h}{\sqrt{g}} \left[1 + \frac{1}{3} \frac{\mathrm{d}(\ln\, h)}{\mathrm{d}(\ln\, \mathrm{T})} \right], \tag{5.32}$$

and we use the tabulated values for $g_\star$ from Ref. [52]. We arrive at the final expression for $\frac{dW}{dx}$ for the $3\pi_D \to \pi_D\rho_D$ process, which we will solve numerically:

$$\frac{dW}{dx} = \sqrt{g_\star}\sqrt{\frac{\pi}{45}} M_{\rm Pl} \frac{m_{\pi_D} s}{x^2} \langle \sigma v^2 \rangle_{3\pi_D \to \pi_D\rho_D} \left(e^{2W_{\rm eq}} - e^{2W} \right). \tag{5.33}$$

The equation for the $3\pi_D \to 2\pi_D$ is slightly different as we have two identical particles in the final state. We stated the Boltzmann equation for this process in section 3.3, and the quantity $\frac{dW}{dx}$ reads

$$\frac{dW}{dx} = \frac{s^2}{\tilde{H} x} \langle \sigma v^2 \rangle_{3\pi_D \to 2\pi_D} \left(e^{W + W_{\rm eq}} - e^{2W} \right). \tag{5.34}$$

The differential equation we actually solve is the sum of Equations 5.30 and 5.34. We use the initial condition that Y_{π_D} starts at its equilibrium value $Y^{\rm eq}_{\pi_D} = n^{\rm eq}_{\pi_D}/s$.

First, we define a function that calculates $\frac{dW}{dx}$ as a function of the value of W in the previous time-step and the size of the time-step, x. We construct a class that we call `BSolution` and when we initiate it, we feed it all the relevant model parameters, such as N_{f_D}, N_{c_D}, m_{π_D}, r_m. The class also contains an instance variable called `solution`, which will hold the solution to the Boltzmann equation. To find the solution, we must first call a function under the class called `solve`. The function takes two arguments, `x_init` and `x_inf`, which are the initial and final values of x, respectively. The function will then solve the Boltzmann equation for the dark pion abundance from `x_init` to `x_inf`. We find that using `x_init`$= 10$ and `x_inf`$= 50$ is sufficient to obtain a reliable solution, while maintaining stability and low computational expense.

We use the SciPy library [107] to solve the differential equation numerically. The code snippet below shows how we implement this in Python:

```
def solve(self, x_init, x_inf):
        T = self.mpi/x_init
        g_star_sqrt = gStarSqrt(T)
        gi = self.gi
        s = T**3*(2*hEff(T)*(np.pi**2)/45)
        n = gi * (self.mpi*T/(2*np.pi))**(3/2) * np.exp(-x_init)
        self.Y_init = n/s

        self.solution = solve_ivp(self.dWdx, [x_init, x_inf], [np.log(self.Y_init)],
                        method='Radau', max_step = 1)
```

We show the solutions for several different models in Figure 5.1. We keep $N_{c_D} = 3$ for all models but vary $N_{f_D} = 2$ or 3, and adjust the pion mass to $m_{\pi_D} = 200$ or 150 MeV, respectively, so that the relic abundance matches the dark matter relic abundance very closely. We also vary $r_{\rm m}$ between $1.5 - 1.99$. Please note that for the $N_{f_D} = 2$ case we have no $3\pi_D \to 2\pi_D$ contribution as the WZW term that gives rise to this process does not exist for theories with $N_{f_D} \leq 2$, as discussed in chapter 4.

It is worth noting that for the $3\pi_D \to 2\pi_D$ only solution, we effectively close the $3\pi_D \to \pi_D\rho_D$ channel by not including it in the Boltzmann equation. However, we continue to assume the relation between the pion decay constant f_{π_D} and the mass ratio r_m from Equation 4.24. Therefore, the solutions for the $3\pi_D \to 2\pi_D$ only case also depend on the choice of r_m indirectly.

Immediately, we can see from the $N_{f_D} = 3$ case that the inclusion of the $3\pi_D \to \pi_D\rho_D$ process leads to a much more efficient depletion of the dark pion abundance, and therefore

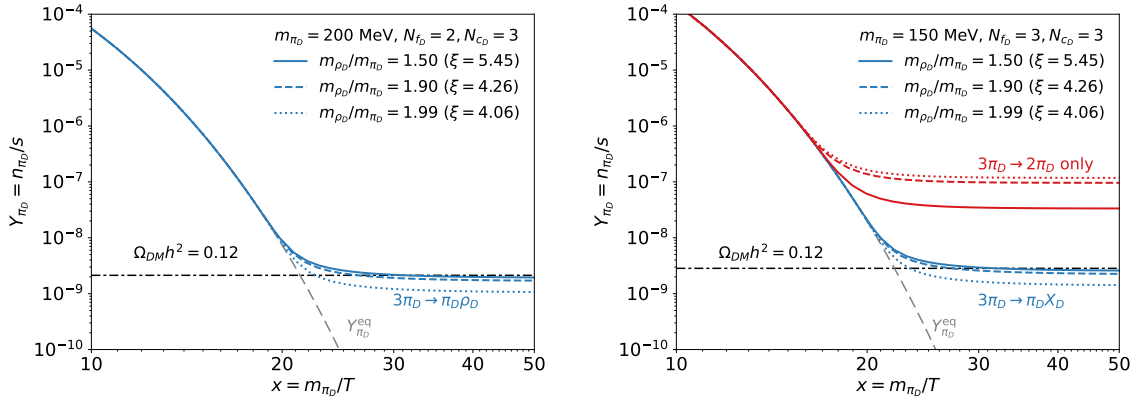

Figure 5.1.: The solution to the Boltzmann equation for the dark pion abundance. The left plot shows the solution for $N_{f_D} = 2$ with $m_{\pi_D} = 200$ MeV. The right plot shows the solution for $N_{f_D} = 3$ and $N_{c_D} = 3$, with $m_{\pi_D} = 150$ MeV. The grey dashed line shows the equilibrium distribution of the dark pions. The black dash-dotted line shows the relic abundance of dark matter, $\Omega_{\rm DM}h^2 = 0.12$.

a lower relic abundance of dark matter. In fact, the $3\pi_D \to \pi_D\rho_D$ process is dominant over the $3\pi_D \to 2\pi_D$ process for all values of r_m that we have considered. This is mainly due to the fact that the $3\pi_D \to \pi_D\rho_D$ is an s-wave type annihilation, while the $3\pi_D \to 2\pi_D$ process is a d-wave type annihilation, and therefore suppressed by the squared velocity, as discussed in section 3.3.

We can confirm this explicitly by comparing the thermally averaged cross sections for the two processes. We find the ratio [1]

$$R \equiv \frac{\langle\sigma v^2\rangle_{3\pi_D\to\pi_D\rho_D}}{\langle\sigma v^2\rangle_{3\pi_D\to 2\pi_D}} = \frac{\alpha^{\rm eff}_{3\pi_D\to\pi_D\rho_D}}{\alpha^{\rm eff}_{3\pi_D\to 2\pi_D}} \approx (1800 - 8500) \times \frac{1}{N_{c_D}^2\,\xi^4}\frac{x^2}{\sqrt{1-y}}$$

by varying y in the range $0.6 < y < 1$ and N_{f_D} between 3 and 6. This ratio is always larger than unity in the parameter space that we consider. Take as an example the freeze-out point at $x \approx 20$ and $N_{c_D} = 3$. For $r_m = 1.5$ we get $\xi = 5.45$, and we then have $R \gtrsim 90$. R increases with higher r_m, where the $\langle\sigma v^2\rangle_{3\pi_D\to\pi_D\rho_D}$ cross section is enhanced. It also increases with higher x, i.e. decreasing temperature, because the d-wave type annihilation decreases with decreasing temperature. This means that the $3\pi_D \to \pi_D\rho_D$ process is always dominant over the $3\pi_D \to 2\pi_D$ process during freeze-out.

It is also instructive to look at the relic abundance of dark pions as a function of r_m and m_{π_D} simultaneously. We show this in Figure 5.2. The white dashed line indicates where the relic abundance matches that of dark matter, i.e. at $\Omega_{\rm DM}h^2 = 0.12$. The choice of $N_{c_D} = 3$ is again used for all models, and we vary $N_{f_D} = 2$ for the left plot and $N_{f_D} = 3$ for the right plot.

The relic abundance of dark pions is naturally very sensitive to their mass, but it can also be very sensitive to the value of r_m in some ranges of r_m. For lower values of r_m, the dependence of the relic abundance on the mass is weak, but as we approach $r_m = 2$ this changes. We see a clear enhancement of the dark pion depletion for larger values of r_m, which is due the fact that the internal dark pions can be nearly on-shell. We also do see this effect in Figure 5.1, where the relic abundance for $r_m = 1.5$ and $r_m = 1.9$ are very similar, despite the large difference in r_m, and the relic abundance is noticeably lower for $r_m = 1.99$.

The relic abundance is largely independent of N_{c_D}, but there is a significant dependence on N_{f_D}. We can approximate numerically, how the preferred dark pion mass for which

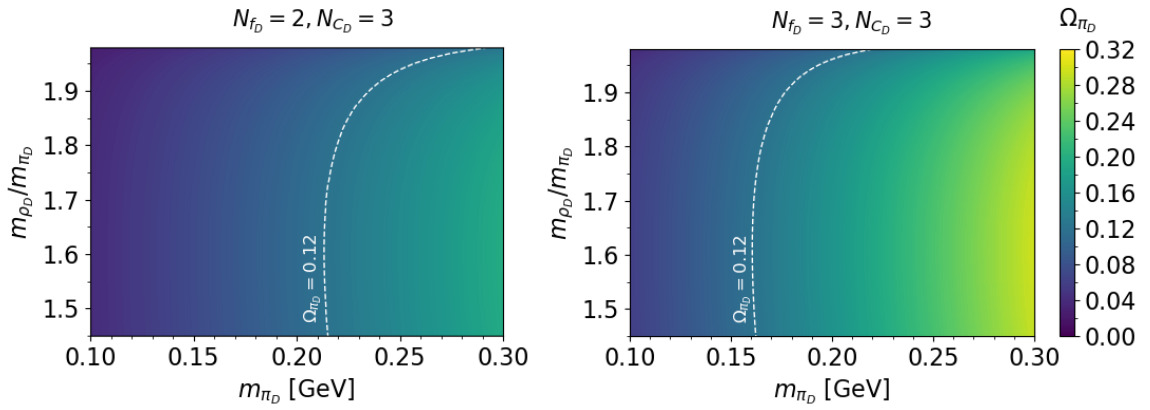

Figure 5.2.: The relic abundance of dark pions as a function of their mass and r_m. The white dashed line shows where the relic abundance of dark matter is $\Omega_{\rm DM}h^2 = 0.12$. The left plot shows the results for $N_{f_D} = 2$ and the right plot for $N_{f_D} = 3$. In both cases, $N_{c_D} = 3$.

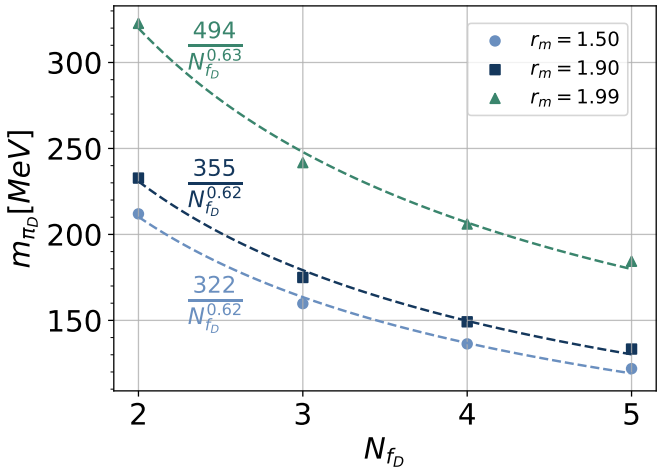

Figure 5.3.: Fits of m_{π_D}, for which $\Omega_{\rm DM}h^2 = 0.12$, as a function of N_{f_D} and r_m. We have set $N_{c_D} = 3$ for all models.

$\Omega_{\rm DM}h^2 = 0.12$ depends on N_{f_D} and r_m. We show the results of these fits in Figure 5.3, where $N_{c_D} = 3$. We find that generally $m_{\pi_D}^{\rm relic} \propto N_{f_D}^{2/3}$, and more specifically we find that

$$m_{\pi_D}^{\rm relic} \approx \begin{cases} 322 N_{f_D}^{-2/3} & \text{if } r_m = 1.50 \\ 355 N_{f_D}^{-2/3} & \text{if } r_m = 1.90 \\ 494 N_{f_D}^{-2/3} & \text{if } r_m = 1.99 \end{cases} \tag{5.35}$$

5.3. ρ_D interactions with the Standard Model

As mentioned earlier, we assume that the dark rho mesons couple to the SM fermions with a coupling strength g_ℓ. We can write the interaction Lagrangian as

$$\mathcal{L}_{\rho_D - \rm SM} = g_\ell \rho_{D\mu} \bar{\ell} \gamma^\mu \ell, \tag{5.36}$$

where ℓ is a SM lepton, which we will take to be the electron and positron, as this is the dominant annihilation channel for the dark rho mesons in the mass ranges that we are inter-

ested in. This leads to the decay of the dark rho meson into an electron-positron pair, with a decay width for $m_{\rho_D} \gg m_e$ as

$$\Gamma_{\rho_D} = \frac{m_{\rho_D} g_\ell^2}{12\pi}. \tag{5.37}$$

In the case that the mixing arises from a massive Z' boson, as discussed in subsection 4.1.2, we have that

$$g_\ell = \frac{{m_{\rho_D}}^2}{m_{Z'}^2} \frac{2ee_D\kappa}{g_{\pi_D\rho_D}}, \tag{5.38}$$

To maintain thermal equilibrium between the dark sector and the SM, the interactions must be sufficiently frequent. We can find this lower limit on g_ℓ by studying the Boltzmann equation for the dark rho meson decay process, which is given by [1]

$$\frac{\mathrm{d}Y}{\mathrm{d}x} = -\frac{\Gamma_{\rho_D}}{Hx}\left(\frac{Y}{Y^{\mathrm{eq}}} - 1\right), \tag{5.39}$$

where Γ_{ρ_D} is the decay width of the dark rho meson, given by Equation 5.37. We can define $y = Y/Y_{\mathrm{eq}}$ and require that $y \approx 1$ to maintain thermal equilibrium. We may find that $Y^{\mathrm{eq}} \propto e^{-x}x^{3/2}$, such that

$$x\frac{\mathrm{d}y}{\mathrm{d}x} = -\frac{\Gamma_{\rho_D}}{H}(y-1) + y\left(x - \frac{3}{2}\right). \tag{5.40}$$

To maintain $y \approx 1$, we require that the first term on the right-hand side dominates over the second term. This is because the first term "works against" the deviation of y from unity, while the second term "works with" the deviation, meaning that if $y > 1$ the first term will decrease y while the second term will increase it further - and vice verse for $y < 1$. Therefore, we require that

$$\frac{\Gamma_{\rho_D}}{H} \gg x. \tag{5.41}$$

We evaluate this condition at the freeze-out point $x \sim 20$, for a model with $m_{\pi_D} = 100$ MeV, $m_{\rho_D} \approx 2m_{\pi_D}$, which is expected to give the strongest constraint on g_ℓ. This gives us the lower bound $g_\ell \gtrsim \times 10^{-9}$.

The upper bound on g_ℓ can be derived by considering the contribution of the annihilation process of $\pi_D\pi_D$ into SM particles on the freeze-out of the dark pions. In the mass ranges that we are interested in, the dominant annihilation channel is $\pi_D\pi_D \to e^+e^-$, and so we will focus on this process. The annihilation occurs via an s-channel ρ_D mediator. The dark pions couple to the ρ_D via the interaction term in Equation 4.9, and the ρ_D couples to the SM fermions via kinetic mixing with the photon.

The amplitude of this reaction is given by the product of the amplitudes of the three parts of the process; the annihilation of the two incoming π_D into a ρ_D, the ρ_D propagator, and the decay of the ρ_D into an electron and positron. The first part we identify from the Lagrangian for the $2\pi_D\rho_D$ interaction in Equation 4.9, and it is given by

$$\mathcal{M}_{2\pi_D\to\rho_D} = 2ig_{\pi_D\rho_D}(p_a - p_b)\mathrm{Tr}\left([T_a, T_b]T_e\right) \tag{5.42}$$

where $p_{a,b}$ is the momentum of the incoming pions, and we use the subscript e to denote the ρ_D in the interaction.

The rho propagator yields the contribution

$$\mathcal{M}_{\rho_D} = \frac{-i}{s - m_{\rho_D}^2 + im_\rho\Gamma_{\rho_D}} \tag{5.43}$$

where s is the squared momentum of the propagator, using that in the non-relativistic limit the s-wave contribution dominates and we define $s = (p_a + p_b)^2 = 4{m_{\pi_D}}^2$.

The matrix element for the ρ_D decay into an electron and positron is similar to that of textbook examples of vector boson decays into fermions, and is given by

$$\mathcal{M}_{\rho_D \to e^+e^-} = (ie\kappa) \sum_f \bar{u}(p_c) q_f \gamma^\mu v(p_d), \tag{5.44}$$

where $p_{c,d}$ is the momentum of the outgoing positron and electron, respectively, e is the electric charge of the electron, and κ is the kinetic mixing parameter of between the ρ_D and SM fermions.

Putting Equation 5.42, Equation 5.43, and Equation 5.44 together, we find the full matrix element for the process $2\pi_D \to e^+e^-$:

$$\mathcal{M}_{2\pi_D \to e^+e^-} = 2ig(p_a - p_b)\mathrm{Tr}\left([T_a, T_b]T^e\right) \times \frac{-i}{s - m_\rho^2 + i m_{\rho_D}\Gamma_{\rho_D}} \times (ie\kappa) \sum_f \bar{u}(p_c) q_f \gamma^\mu v(p_d). \tag{5.45}$$

We then get the squared matrix element

$$|\mathcal{M}|^2_{2\pi_D \to e^+e^-} = \frac{4g^2(e\kappa)^2 \Sigma_{abe} |\mathrm{Tr}\left([T_a, T_b]T_e\right)|^2}{N_{\pi_D}^2 (s - {m_{\rho_D}}^2)^2} \sum_{\text{spin}} \Big(\bar{u}(p_c)(\not{p}_a - \not{p}_b) v_(p_d) \bar{v}(p_d)(\not{p}_a - \not{p}_b) u_(p_c) \Big), \tag{5.46}$$

where we have summed over initial states and over the spin of the final state fermions. In the center of mass frame, we find that [59]

$$\sum_{\text{spin}} \Big(\bar{u}(p_c)(\not{p}_a - \not{p}_b) v_(p_d) \bar{v}(p_d)(\not{p}_a - \not{p}_b) u_(p_c) \Big) = 32p^2[k^2(1 - \cos^2\theta) + m_{e^-}^2], \tag{5.47}$$

where p is the 3-momentum of the incoming pions, k is the 3-momentum of the outgoing electron and positron, and θ is the scattering angle. We get the squared matrix element

$$|\mathcal{M}|^2_{2\pi_D \to e^+e^-} = \frac{4g^2(e\kappa)^2 \Sigma_{abe} |\mathrm{Tr}\left([T_a, T_b]T_e\right)|^2}{N_{\pi_D}^2 (s - {m_{\rho_D}}^2)^2} 32p^2[k^2(1 - \cos^2\theta) + m_{e^-}^2] \tag{5.48}$$

The thermally averaged cross section is determined via a similar method as for the $3\pi_D \to \pi_D\rho_D$ process in section 5.1, with the general expression for the thermally averaged cross section for a $2 \to 2$ process [56]:

$$\begin{aligned} \langle \sigma v \rangle_{2\pi_D \to e^+e^-} = \frac{1}{(n^{\text{eq}}_{\pi_D})^2} \frac{1}{S_I S_F} \int d\Pi_{{\pi_D}^1} d\Pi_{{\pi_D}^2} (f^{\text{eq}}_{\pi_D})^2 N^2_{\pi_D} \\ \times \int d\Pi_{e^+} d\Pi_{e^-} (2\pi)^4 \delta^{(4)}(p_1 + p_2 - p_4 - p_4) |\mathcal{M}|^2_{2\pi_D \to e^+e^-}. \end{aligned} \tag{5.49}$$

We then follow the procedure outlined in [50, 59, 108] to arrive at the result:

$$\langle \sigma v \rangle_{2\pi_D \to e^+e^-} = \frac{g_\ell^2 \alpha \alpha_D}{3\sqrt{\pi}} \frac{N_{f_D}}{N_{f_D}^2 - 1} \frac{x^{3/2} e^{2x}}{m^2_{\pi_D}} \int_1^\infty d\tilde{s} \frac{\tilde{s}^{3/4} (\tilde{s} - 1)^{3/2} e^{-2x\sqrt{\tilde{s}}}}{(\tilde{s} - \frac{m^2_{\rho_D}}{4m^2_{\pi_D}})^2}. \tag{5.50}$$

where $\tilde{s} = s/(4{m_{\pi_D}}^2)$ is dimensionless, and we use that $\Sigma_{abe} |\mathrm{Tr}\left([T_a, T_b]T_e\right)|^2 = N_{f_D}(N_{f_D}^2 - 1)/4$ and $N_{\pi_D} = N_{f_D}^2 - 1$.

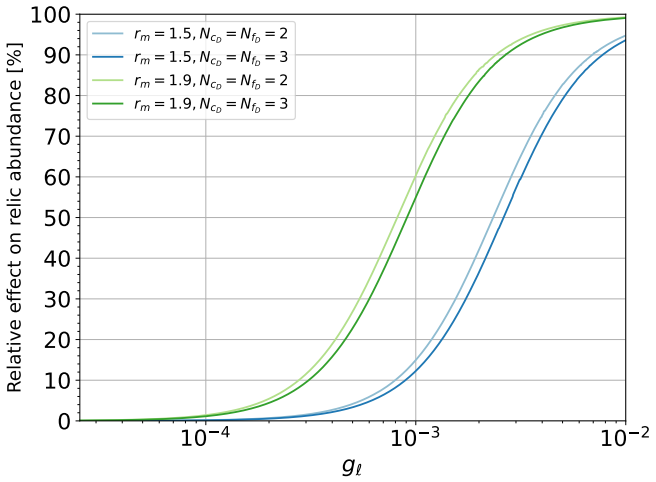

Figure 5.4.: The relative effect on the relic abundance when including $\pi_D\pi_D \to e^+e^-$ annihilations as a function of the coupling strength, g_ℓ. We show the effect for different values of r_m and N_{f_D}, N_{c_D}, while $m_{\pi_D} = 100$ MeV for all models.

We can investigate the effect of dark pion annihilations into SM particles by including this process in the Boltzmann equation. In Figure 5.4 we show the relative effect on the relic abundance when including $\pi_D\pi_D \to e^+e^-$ annihilations as a function of the coupling strength, g_ℓ. The relative effect is defined as

$$\text{Relative effect} = \frac{\Omega_{\pi_D}h^2|_{\text{without } \pi_D\pi_D\to e^+e^-} - \Omega_{\pi_D}h^2|_{\text{with } \pi_D\pi_D\to e^+e^-}}{\Omega_{\pi_D}h^2|_{\text{without } \pi_D\pi_D\to e^+e^-}}. \tag{5.51}$$

We see that for $g_\ell \lesssim 10^{-4}$, we have a very small relative effect, meaning that the annihilations into SM particles do not contribute significantly to the depletion of the dark pion abundance. However, as we increase g_ℓ, we see that the relative effect increases, and for $g_\ell \sim 10^{-2}$, we have a relative effect of order one, meaning that the annihilations into SM particles are just as important as the $3\pi_D \to \pi_D\rho_D$ and $3\pi_D \to 2\pi_D$ processes in depleting the dark pion abundance.

We therefore conclude that the results in our calculations of the relic abundance are unaffected by the annihilations into SM particles as long as $g_\ell \lesssim 10^{-4}$.

5.4. π_D self-interactions and the Bullet Cluster constraints

Dark pions can undergo self-interactions through two primary mechanisms. The first is a direct four-point contact interaction, $\pi_D\pi_D \to \pi_D\pi_D$, which is governed by the Lagrangian shown in Equation 4.12. The second mechanism involves the exchange of a virtual ρ_D, which can mediate the interaction via the s-, t-, and u-channel diagrams. In the non-relativistic limit, the contribution from ρ_D exchange becomes suppressed due to its dependence on the momentum transfer. As a result, the four-point contact interaction becomes the dominant contribution to the self-scattering process, and we will only consider this contribution. The cross section of the contact interaction is given by the expression [1]

$$\sigma_c = \frac{1}{2\pi s}\frac{1}{f_{\pi_D}^4}\left(\frac{3N_{f_D}^4 - 2N_{f_D}^2 + 6}{8N_{f_D}^2(N_{f_D}^2-1)}m_{\pi_D}^4 + \frac{N_{f_D}^2}{N_{f_D}^2-1}\left(m_{\pi_D}^2p^2 + \frac{5}{6}p^4\right)\right),$$

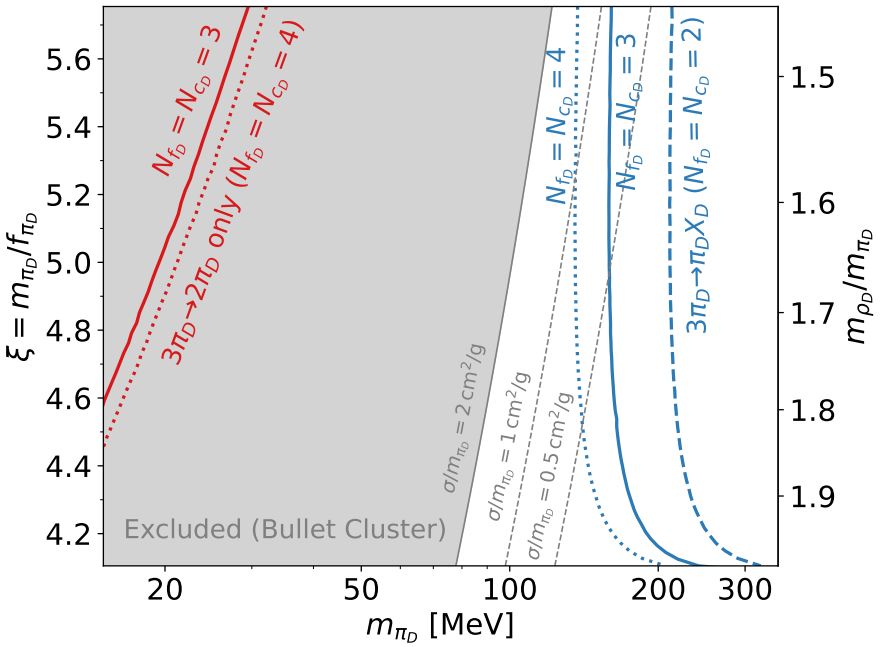

Figure 5.5.: Combinations of m_{π_D} and ξ or r_m that yield the correct dark matter relic abundance $\Omega_D h^2 = 0.12$. For the red lines only the process $3\pi_D \to 2\pi_D$ is included, whereas for the blue lines $3\pi_D \to \rho_D \pi_D$ is also taken into consideration. Note that the process $3\pi_D \to 2\pi_D$ does not exist for $N_{f_D} = 2$. The grey shaded region is excluded by the Bullet Cluster bound on the DM self-interaction cross section (evaluated for $N_{f_D} \gg 1$).

where p is the momentum of each incoming dark pion. In the non-relativistic limit, we can approximate the momentum transfer as $p^2 \approx 0$ and $s \approx 4{m_{\pi_D}}^2$, such that the cross section simplifies to

$$\sigma_c \approx \frac{1}{64\pi} \frac{3N_{f_D}^4 - 2N_{f_D}^2 + 6}{N_{f_D}^2(N_{f_D}^2 - 1)} \frac{\xi^4}{{m_{\pi_D}}^2} = \frac{3}{64\pi} \frac{{m_{\pi_D}}^2}{f_{\pi_D}^4} (1 + \mathcal{O}(N_{f_D}^{-2})). \tag{5.52}$$

We compare this to the bound on the self-interaction cross section from the Bullet Cluster observations, which was discussed in chapter 3. To briefly iterate, the Bullet Cluster observations provide a constraint on the self-interaction cross section of dark pions, which can be expressed as

$$\sigma_c \lesssim 2 \text{ cm}^2/\text{g} \tag{5.53}$$

although the exact value of the constraint is still debated in the literature [40, 49].

Figure 5.5 shows lines where we obtain the correct relic abundance of dark pions, $\Omega_{\pi_D} h^2 = 0.12$, as a function of the dark pion mass m_{π_D} and the ratio r_m. The red lines show the results when only including the $3\pi_D \to 2\pi_D$ number-changing process, while the blue lines show the results when including the $3\pi_D \to \pi_D \rho_D$ process. Going to lower masses will result in a lower relic abundance for each model, and conversely, going to larger masses will result in a larger relic abundance. We show the Bullet Cluster bound as the grey region, denoting also the various values for the exact bound.

The $3\pi_D \to 2\pi_D$ models are excluded for all values of r_m that we consider, as expected from conclusions in the literature. It should be noted that there is a small region of parameter space that may be allowed, depending on the exact bound, but this regions exists at values

of $\xi \sim 12$ [59], i.e. right at the edge of the perturbative regime and outside our considered range of ξ. The $3\pi_D \to \pi_D\rho_D$ models, however, are allowed for our entire range of our r_m if $\sigma_c/m_{\pi_D} \lesssim 2\text{cm}^2/\text{g}$, or for $r_m \gtrsim 1.65$ (1.8) for $N_{f_D} = 3$ ($N_{f_D} = 4$) if $\sigma_c/m_{\pi_D} \lesssim 0.5\text{cm}^2/\text{g}$.

This result is as expected because the $3\pi_D \to \pi_D\rho_D$ process is much more efficient at depleting the dark pion abundance. Furthermore, we see that $\langle\sigma v^2\rangle_{3\pi_D\to 2\pi_D} \propto \xi^{10}/{m_{\pi_D}}^5$ requires large values of ξ or low values of m_{π_D} to deplete the dark pion abundance sufficiently. Meanwhile, the self-interaction, $\sigma_c \propto \xi^4/{m_{\pi_D}}^2$, requires low values of ξ or large values of m_{π_D} to satisfy the Bullet Cluster constraint. The tension between these two is relieved by the $3\pi_D \to \pi_D\rho_D$ process, depleting the dark matter abundance efficiently, with a weak but inverse dependence on ξ, i.e. the efficiency of the $3\pi_D \to \pi_D\rho_D$ process increases with decreasing ξ. This allows for a smaller self-interaction cross section while still depleting the dark pion abundance sufficiently to satisfy the relic abundance constraint.

CHAPTER 6

Studies of a Light Vector Meson Model at Accelerator Experiments

If a strongly interacting dark sector indeed consists of feebly interacting light vector mesons, as we saw in chapter 5 is a cosmologically favorable scenario, they are expected to decay exclusively into SM particles. We deduced the lifetime of the ρ_D^0 in subsection 4.2.2, assuming kinetic mixing with the SM photon, and found that it can be on the scale of centimeters to meters, depending on the values of the suppression scale Λ (or the kinetic mixing parameter κ). This opens up a very exciting possibility of detecting the ρ_D^0 at accelerator experiments, where we can look for displaced vertices (DVs) from the decay of LLPs.

In Ref. [86], the phenomenology of a light ρ_D meson at the Belle II experiment was studied. The authors of Ref. [86] found that a dedicated DV search, with final states e^+e^-, $\mu^+\mu^-$, $\pi^+\pi^-$ or K^+K^-, at Belle II could probe a significant portion of the parameter space of the model for ρ_D masses below 2 GeV. They compared the sensitivity of Belle II to that of other experiments, including BaBar and LHCb, and concluded that LHCb may have complimentary sensitivity, particularly in the shorter lifetime regime and larger masses.

However, beam dump experiments offer a unique opportunity to probe very small couplings and long lifetimes, particularly in experimental setups with detectors far down from the target. In this chapter, we will therefore focus on the recently approved SHiP experiment at CERN, which is designed to search for feebly interacting particles (FIPs) with lifetimes on the scale of meters. We will explore the potential of SHiP to detect the light ρ_D^0 meson through displaced decays, leveraging the high intensity of the proton beam and the large decay volume of the detector. This will be compared to the sensitivity of the NA62 and the Belle II experiments. Overviews of the SHiP, NA62 and Belle II experiments are given in section 6.1, section 6.2, and section 6.3 , respectively.

The dark sector that we will explore is based on the theoretical framework outlined in chapter 4. The details of the simulation are discussed in section 6.4. While we remained ambiguous about the portal to the SM in the previous chapter, we necessarily must specify it here, as it will determine the production and decay of the ρ_D^0. We will assume kinetic mixing between the Z' and the SM hypercharge gauge boson, as described in subsection 4.1.2. This will allow the ρ_D^0 to mix with the SM photon and subsequently decay into SM fermions. Interestingly, the kinetic mixing will also allow for the production of the dark ρ_D^0 through dark photon-like mechanisms. This is discussed in more detail in section 6.5.

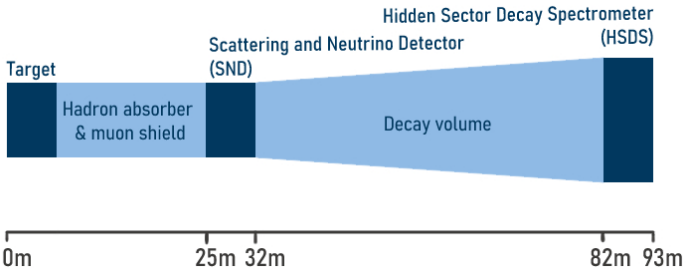

Figure 6.1.: Overview of the target and experimental area for the SHiP detector as implemented in the physics simulation. [79]

In section 6.6, we outline the procedures for estimating the sensitivity of the three different experiments to the ρ_D^0 meson, where we utilize the `SensCalc/EventCalc` programmes [109, 110] for the SHiP and NA62 experiments, and an analysis implemented in Ref. [86] for the Belle II experiment. Finally, we present the results of our sensitivity study in section 6.7.

6.1. The SHiP Experiment

The SHiP (Search for Hidden Particles) experiment at CERN is an upcoming fixed-target facility designed to explore the intensity frontier by searching for GeV-scale feebly interacting particles [79, 111, 112]. It is expected to start taking data in 2031. Using a 400 GeV proton beam extracted from the CERN SPS accelerator dumped on a tungsten target, SHiP will generate an unprecedented number of heavy flavour mesons. Within its full 15 years of data taking, the facility is expected to deliver approximately 6×10^{20} protons on target (PoT), producing $\mathcal{O}(10^{18})$ charmed mesons and $\mathcal{O}(10^{14})$ bottom mesons [113]. With such a high intensity beam, a large decay volume and advanced systems to suppress backgrounds, SHiP can explore parameter regions that are inaccessible to current accelerator experiments, especially for particles with very small couplings and long lifetimes.

The layout of the SHiP experiment[6] is shown in Figure 6.1. Immediately after dumping the proton beam on the target, the particles resulting from the interaction will travel through a hadron absorber and magnetic muon shield to filter out SM particles, with neutrinoes of course being an exception. At about 27 meters downstream from the target, the first detector is placed. This is the Scattering and Neutrino Detector (SND), which main purpose is to identify neutrino-induced background events. The second detector is the Hidden Sector Decay Spectrometer (HSDS), which proceeds a 50 meter long decay volume. The current design of the HSDS spans an area of 4×6 m^2, and consists of a tracker, an electromagnetic and a hadronic calorimeter, allowing for decay vertex reconstruction and particle identification. It is ensured to have very low background noise, as the decay volume is kept under vacuum and surrounded by high-efficiency background taggers.

The center of mass energy at SHiP is $\sqrt{s} = 27.42$ GeV, putting it at higher energy than Belle II ($\sqrt{s} = 10.58$ GeV), and much lower than that of LHCb ($\sqrt{s} = 13$ TeV). The typical partonic center of mass energy at SHiP is $\sqrt{\tilde{s}} \approx 4$ GeV, which means that we expect to be able to probe ρ_D masses up to ~ 4 GeV, depending on the production mechanism. This is particularly interesting, as it allows us to explore a mass range that is complementary to that of Belle II and LHCb, which are more sensitive to lower masses. Additionally, the long decay

[6] It is important to note that the layout and design of the SHiP experiment are still subject to updates as the project evolves. As new insights are gained and technical challenges are addressed, modifications to the experimental setup may be implemented. The description in this thesis is based on the design plans as of 2025 [79] and may not fully reflect the final configuration of the experiment.

volume of SHiP (50 meters) allows for the detection of particles with lifetimes on the scale of meters, which is particularly relevant for our dark sector model where the ρ_D can have a long lifetime due to its feeble coupling to the SM.

6.2. The NA62 Experiment

The NA62 experiment at CERN [114] is designed to investigate ultra-rare kaon decays and conduct precision tests of the SM. The initial phase of data collection took place between 2016 and 2018, followed by a second run from 2021 after the experiment underwent upgrades. Data acquisition is expected to continue at least through 2026 [115].

The experiment utilizes a 400 GeV proton beam from the CERN SPS accelerator, same as SHiP. It was designed to operate in two modes [116]: a standard mode, where the proton beam strikes a beryllium target to produce a secondary beam of hadrons, and a "beam-dump" mode, where the proton beam is directly dumped onto a copper and iron target. The former mode is used for studying rare kaon decays, such as $K^+ \to \pi^+ \nu\bar{\nu}$, and will not be discussed further in this work. On the other hand, the latter mode is particularly relevant for our dark sector studies, as it allows for the production of LLPs that can decay within the detector volume.

The experiment features a 117-meter-long vacuum vessel, starting roughly 105 meters downstream from the target. In 2021, NA62 began operating in beam-dump mode, and has collected data corresponding to 1.4×10^{17} PoT. The experiment is expected to accumulate up to 1×10^{18} PoT by the end of its beam-dump operation [115]. Due to the significantly lower number of PoT compared to SHiP, NA62 is expected to have a lower sensitivity to the FIPs. Additionally, as the decay volume begins further downstream from the target, NA62 is expected to lose sensitivity quickly to short lifetimes, or large m_{ρ_D}, compared to SHiP.

6.3. The Belle II Experiment

Located in Japan at the KEK laboratory, the Belle II experiment is a current accelerator experiment designed to explore the properties of B mesons and search for new physics beyond the SM [117]. It is an upgrade of the original Belle experiment, which operated from 1999 to 2010. Belle II began data collection in 2018 and aims to accumulate an integrated luminosity of 50 ab^{-1}.

Belle II operates at the SuperKEKB accelerator, which collides an electron beam with energy of 7 GeV and a positron beam with energy of 4 GeV, resulting in a center-of-mass energy of $\sqrt{s} = 10.58$ GeV [117]. This energy is at the mass of the $\Upsilon(4S)$ resonance, which predominantly decays into pairs of B mesons. The experiment is thus also known as a B-factory, as it is optimized for producing large numbers of B mesons. The high luminosity of SuperKEKB allows Belle II to collect a vast amount of data, enabling precision measurements of B meson decays and searches for rare processes.

The Belle II detector is a full solid-angle detector, consisting of several sub-detectors; a vertex detector, a central drift chamber, a particle identification detector, an electromagnetic calorimeter, and a K-long and muon detector [117]. The advanced detector design allows for detection of LLPs with decay lengths on the order of millimeters to meters, making it well-suited for searching for FIPs [86]. The experiment has already conducted searches for various FIP candidates, including dark photons [118].

6.4. Simulating the ρ_D^0 production at accelerators

We will simulate an $SU(3)$ dark sector with $N_{f_D} = 2$ dark quarks. This will give us three dark pions and three dark rhos. We extend the dark sector with a $U(1)'$ gauge group, under which the dark quarks are charged. If we assume unit charge for the dark quark, the dark pions will be charged as $\{+2, 0, -2\}$ and the dark rhos as $\{+2, 0, -2\}$. The neutral dark rho, ${\rho_D}^0$, will mix with the SM fermions, as described in subsection 4.1.2. We will consider two different values of the ratio r_m, namely $r_m = 1.5$ and $r_m = 1.9$. These two values are near the lower and upper limits of the range of r_m that we consider, as per the discussion in subsection 4.1.3, and should provide a good representation of the phenomenology of the model.

We simulate the process $pp \to Z' \to q_d\bar{q}_d$ in MadGraph v.3.5.8 [101], using a UFO file that models the effective interaction between dark quarks and SM quarks, as described in section 4.3. The subsequent dark shower is simulated with the Hidden Valley (HV) module in Pythia v. 8.313 [100]. Both programs are run in the CM frame. The main reason for this is that we will need to simulate mass scales below 1 GeV, which is not supported by the version of Pythia we are using,[7] and we will circumvent this by applying a scaling to all energetic variables in the dark sector as well as the CM energy. We will discuss the details of this procedure in the next section. An important point is that, in a symmetric collision we will not need to worry about the mass of the incoming particles when we scale the variables, whereas in a fixed-target experiment we do. Thus, simulating in the CM frame is more convenient, and we perform the boost to the lab frame of SHiP only after the simulation and rescaling method has been applied.

The parameter choices for the simulation are summarized in Table 6.1. We follow the theoretical framework outlined in subsection 4.1.3, ensuring a consistent model. We set $m_{Z'} = 1$ TeV and $\Gamma_{Z'} = 1$ GeV to ensure that the Z' is sufficiently heavy to be integrated out, justifying the use of an effective field theory approach for the interaction between dark quarks and SM quarks.

We scan over m_{ρ_D} in the range $0.2 - 3$ GeV, in increments of 0.1 GeV. Additionally, we also simulate the points $m_{\rho_D} = \{0.78, 1.02\}$ GeV to have a finer scan around the resonance points of the SM ρ, ω and ϕ mesons. We simulate 10^6 events per parameter point.

An important remark is that we set the kinetic mixing parameter κ to a fixed value of 10^{-3} in the simulation. However, we will later rescale the results to different values of κ when we estimate the sensitivity of SHiP to the ρ_D meson. This is possible because the production cross section of the dark quarks scales as κ^2 and therefore, the number of expected events at SHiP will scale with κ^2. This is not including the ρ_D decay probabality, but this factor is taken care of later (see section 6.6). We can find the cross section for any κ given the reference coupling, κ_{ref}, by the relation;

$$\sigma(\kappa) = \sigma(\kappa_{\text{ref}}) \left(\frac{\kappa}{\kappa_{\text{ref}}} \right)^2 . \tag{6.1}$$

This approach allows us to efficiently explore a wide range of kinetic mixing values without needing to rerun the computationally intensive simulations for each value.

We use the NNPDF23_nlo_as_0119 parton distribution function (PDF) set [120] and fix the factorization scale for the PDF of the incoming beams (the parameter `dsqrt_q2fact`$_{1,2}$) to 10 GeV. Using a constant factorization scale ensures that the proton PDFs remain unchanged

[7] A later version of Pythia (v.8.315) has been released that supports simulating HV mass scales below the QCD scale, but was not available during the entirety of the project and remains to be properly validated. [119]

Table 6.1.: Model parameters used in MadGraph and Pythia for simulating the dark sector.

Parameter	Value ($r = 1.5$)	Value ($r = 1.9$)	Setting in
$m_{Z'}$	1 TeV		MadGraph
$\Gamma_{Z'}$	1 GeV		MadGraph
`dsqrt_q2fact`$_{1,2}$	10 GeV		MadGraph
`scalefact`	1		MadGraph
`dsqrt_shat`	$2m_{\pi_D}$		MadGraph
κ	1×10^{-3}		MadGraph
e_d	1		MadGraph
N_{C_D}	3		MadGraph, Pythia
N_{f_D}	2		MadGraph, Pythia
m_{ρ_D}	$0.2 - 3$ GeV		Pythia
r_m	1.5	1.9	Pythia
$m_{\pi_D} = \frac{m_{\rho_D}}{r_m}$	$0.134 - 2.3$ GeV	$0.1 - 1.8$ GeV	Pythia
$\Lambda_D = \frac{5}{12} \cdot m_{\pi_D} \cdot \sqrt{r_m^2 - 1.5}$	$0.36 m_{\pi_D}$	$0.61 m_{\pi_D}$	Pythia
$m_{q_D,\text{curr}} = \frac{4}{121} \cdot \frac{{m_{\pi_D}}^2}{\Lambda_D}$	$0.09 m_{\pi_D}$	$0.05 m_{\pi_D}$	MadGraph
$m_{q_D,\text{const}} = m_{q_D,\text{curr}} + \Lambda_D$	$0.45 m_{\pi_D}$	$0.66 m_{\pi_D}$	Pythia
`probVec`	0.71	0.68	Pythia

under the rescaling procedure, which we will describe in Section 6.4.2. We have verified that varying the factorization scale within the range $2 - 20$ GeV modifies the total cross section by less than 20% and has a negligible impact on kinematic distributions.

Additionally, we impose a minimum partonic center-of-mass energy (`dsqrt_shat`) of $\sqrt{\hat{s}} = 2m_{\pi_D}$, which excludes Drell–Yan production of a single dark ρ_D meson. This contribution is instead accounted for explicitly in the dark-photon-like production modes, which we discuss in section 6.5.

We have set `dynamical_scale_choice` to option 4, meaning that the renormalization scale is set to $\sqrt{\hat{s}}$. We choose the event-by-event scale factorisation (`scalefact`) to 1.

6.4.1. Lorentz boosting

Since we are simulating the events in the center-of-mass (CM) frame, we need to perform a Lorentz boost to transform the results into the laboratory frame of SHiP after the simulation. This step is essential because, unlike collider experiments—where two particle beams collide head-on in a symmetric setup—fixed-target experiments involve a high-energy particle beam striking a stationary target. As a result, the CM frame is not at rest with respect to the laboratory frame but is instead moving in the direction of the incoming beam. This asymmetry necessitates the boost to accurately interpret the simulated outcomes in the lab frame.

The center of mass energy of the particle collision is defined as the square root of s;

$$\sqrt{s} = \sqrt{(P_1^\mu + P_2^\mu)^2}, \tag{6.2}$$

where P_1^μ and P_2^μ are the four-momuntum vectors of the two colliding particles. Expanding the four-momuntum vectors using $P^\mu = (E, \vec{p})$ and $(P^\mu)^2 = E^2 - \vec{p}^2 = m^2$ gives

$$s = (P_1^\mu)^2 + (P_2^\mu)^2 + 2P_1^\mu P_2^\mu = m_1^2 + m_2^2 + 2E_1E_2 - 2\vec{p_1} \cdot \vec{p_2} \tag{6.3}$$

For the case of SHiP, we set $m_1 = m_2 = m_p$, $E_1 = \sqrt{m_p^2 + p_z^2}$ where $p_z = 400$ GeV, $E_2 = m_p$ and $\vec{p_1} = (0, 0, p_z)$, $\vec{p_2} = (0, 0, 0)$. These assumptions will be used throughout this section. This gives the center of mass energy

$$\sqrt{s} = \sqrt{2m_p^2 + 2m_p\sqrt{m_p^2 + p_z^2}} = 27.42 \text{ GeV}. \tag{6.4}$$

We will be interested in simulating the collision in the CM frame for reasons that will be discussed in the next section. Therefore, we need to perform a Lorentz boost from the CM frame, in which our simulations will be performed, to the lab frame of SHiP, where we want to analyze the results. The Lorentz boost is defined by the Lorentz factor $\gamma = \frac{1}{\sqrt{1-\beta^2}}$ and the velocity $\beta = \frac{v}{c}$ of the CM frame relative to the lab frame.

In the CM frame, the two colliding particles have equal and opposite momenta, so we can write the four-momuntum of either of the particles as

$$(P^\mu)_{\text{CM}} = \left(\frac{1}{2}\sqrt{s}, 0, 0, p_z\right) \tag{6.5}$$

In the SHiP lab frame, the target particle is at rest, so its four-momentum is

$$(P^\mu)_{\text{lab}} = (m_p, 0, 0, 0). \tag{6.6}$$

We then define the boost to the CM frame, which moves with a velocity β in the z-direction relative to the lab frame;

$$(P^\mu)_{\text{CM}} = (P^\mu)'_{\text{lab}} = (\gamma(E + \beta p_z), 0, 0, \gamma(p_z + \beta E)) = (\gamma m_p, 0, 0, \gamma\beta m_p) \tag{6.7}$$

This must be equal to the four-momuntum defined in Equation 6.5, thus setting the first components of each four-momentum equal gives the Lorentz factor:

$$\gamma = \frac{\sqrt{s}}{2m_p}. \tag{6.8}$$

Figures 6.2-6.4 show the CM and fixed lab frame, corresponding to the SHiP experiment, distributions of energy, polar angle and multiplicity distributions of the dark mesons produced in the dark shower, for the two different values of r_m that we are studying in this chapter.

6.4.2. Rescaling method to probe low masses

To address the limitations of simulating HV processes in Pythia at low mass scales, we adopt a rescaling strategy. The main idea is to perform the simulation at a higher mass scale, where the simulation software is reliable, and then rescale the results down to the desired lower mass scale. This is done by applying a common scaling factor to all energetic quantities in the dark sector, and the CM energy, ensuring that the kinematic distributions of the dark sector remain consistent after scaling down again. The scaling of the CM energy is naturally going to change the kinematic results of SM particles. However, we exclusively analyze dark particles, and therefore the SM kinematics are irrelevant.

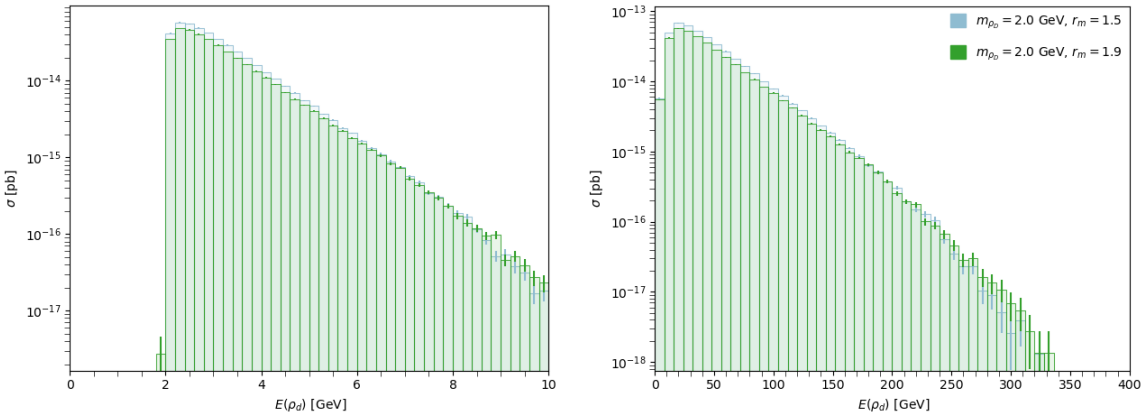

Figure 6.2.: Energy in the CM frame (left) and in the SHiP lab frame (right) distributions of the ${\rho_D}^0$ mesons produced in the dark shower. Both models have $m_{\rho_D} = 2$ Gev, while one has $r_m = 1.5$ and the other has $r_m = 1.9$.

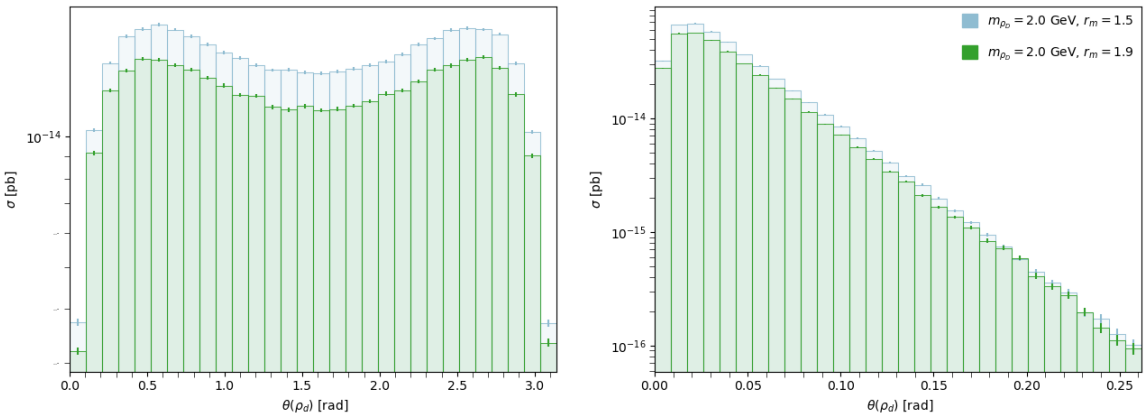

Figure 6.3.: Polar angle in the CM frame (left) and in the SHiP lab frame (right) distributions of the ${\rho_D}^0$ mesons produced in the dark shower. Both models have $m_{\rho_D} = 2$ Gev, while one has $r_m = 1.5$ and the other has $r_m = 1.9$.

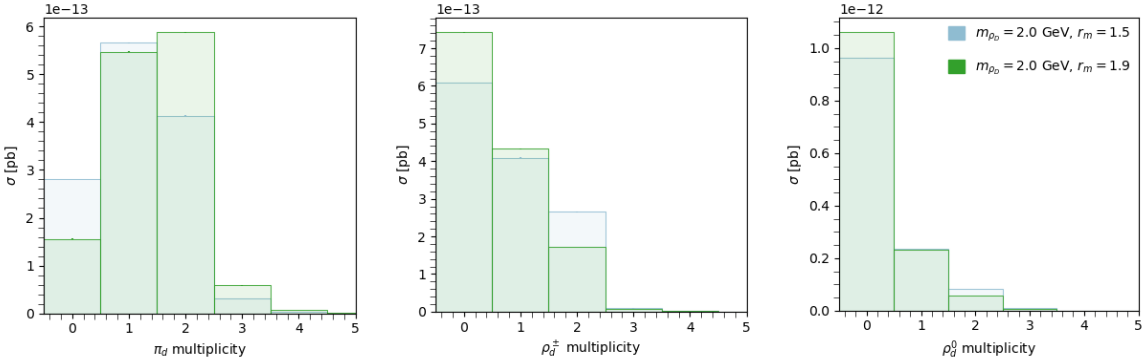

Figure 6.4.: Multiplicity of both neutral and charged π_D (left), of charged ${\rho_D}^{\pm}$ (right) and of neutral ${\rho_D}^0$ (right). Both models have $m_{\rho_D} = 2$ Gev, while one has $r_m = 1.5$ and the other has $r_m = 1.9$.

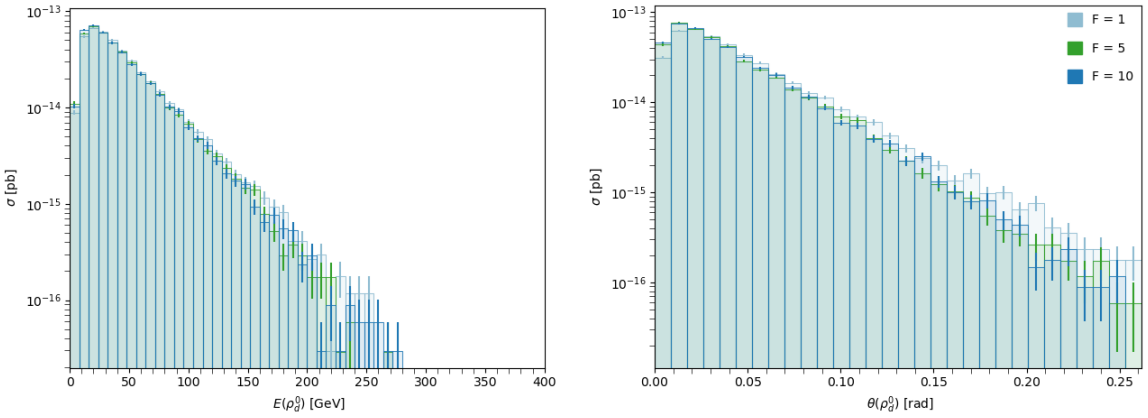

Figure 6.5.: Energy (left) and angle (right) distributions of the ${\rho_D}^0$ mesons produced in the dark shower, for different values of m_{ρ_D} and $r_m = 1.5$. The distributions are shown in the lab frame of SHiP.

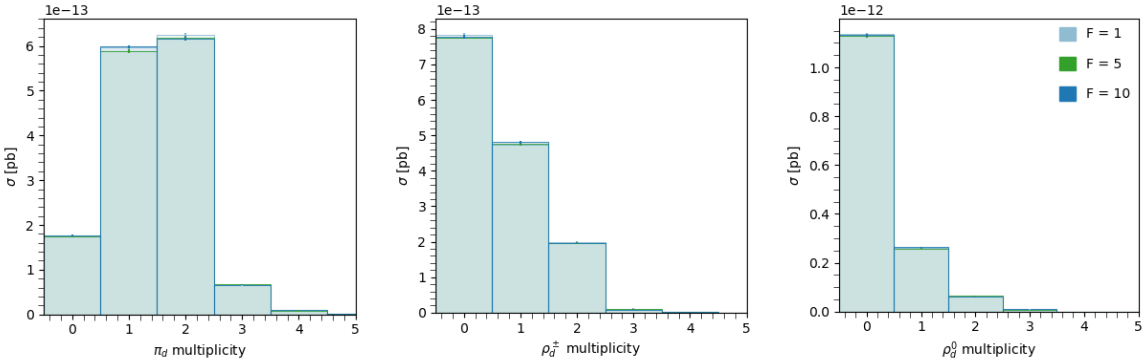

Figure 6.6.: Multiplicity per event of both neutral and charged π_D (left), of charged ${\rho_D}^\pm$ (right) and of neutral ${\rho_D}^0$ (right).

We rescale the following parameters by a common factor F;

$$m_{\pi_D} \to F \times m_{\pi_D}, \quad m_{\rho_D} \to F \times m_{\rho_D}, \quad m_{q_D} \to F \times m_{q_D},$$
$$m_{Z'} \to F \times m_{Z'}, \quad \Gamma_{Z'} \to F \times \Gamma_{Z'}, \quad \Lambda_D \to F \times \Lambda_D, \quad \sqrt{s} \to F \times \sqrt{s}.$$

The factor F is determined by the requirement that $m_{\pi_D} \times F = 1$, if $m_{\pi_D} < 1$ GeV, and $F = 1$ otherwise (i.e. no scaling is applied). This means that we will simulate all mass scales below 1 GeV as if they were 1 GeV, and then rescale the results back down to the desired mass.

It is crucial that we perform a consistency check of our rescaling method by checking that the rescaling does not alter the kinematic distributions of the ρ_D mesons to any significant degree. Therefore, we have validated the rescaling method by comparing the kinematic distributions of the ρ_D mesons for different values of F. Since the lowest mass we want to probe is $m_{\pi_D} \approx 0.1$ GeV, the largest rescaling factor we will need is $F \approx 10$. We also include an intermediate value of $F = 5$. Thus, we validate the rescaling method for $F = \{1, 5, 10\}$.

The validation is done by fixing the pre-scaling parameters such that $m_{\pi_D} = 1$ GeV and $m_{\rho_D} = 1.9$ GeV, performing the scaling to the parameters, run the simulations and then scale back to the original parameters. The results are shown in Figures 6.5 and 6.6.

The results show that the rescaling method does indeed preserve the kinematic distributions of the ρ_D mesons, validating our approach. In particular, the multiplicity distributions are

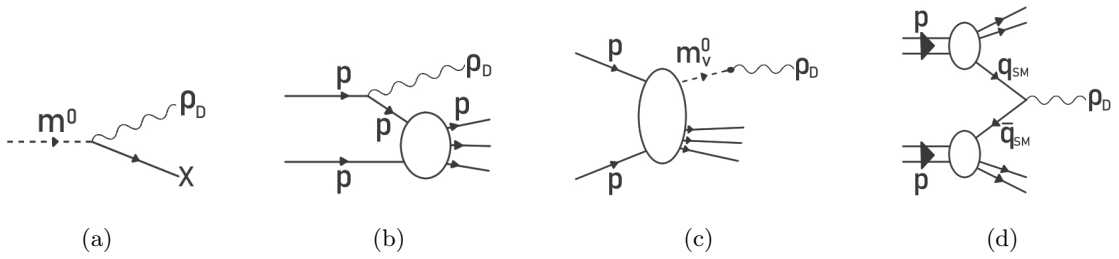

(a) (b) (c) (d)

Figure 6.7.: The diagrams of various dark-photon-like production processes of ρ_D: (a) decays of neutral mesons $m^0 \to \rho_D + X$, (b) proton bremsstrahlung, (c) production via mixing with neutral vector mesons m_v^0, and (d) the Drell-Yan process (quark fusion).

near identical for all the values of F. The multiplicity of ${\rho_D}^0$ is very important for the sensitivity, as each ${\rho_D}^0$ produced in the dark shower is a potential signal event. There are some small deviations in the very tails of both the energy and polar angle distributions, possibly a result of low statistics in our samples. Nonetheless, the discrepancies in the high polar angles are actually not important for us, as SHiP will only be sensitive to very small polar angles of $\theta \sim 0.044$. The discrepancies in the energy distributions are more relevant, as SHiP is most sensitive to high-energy particles. However, the discrepancies are still relatively small, and the uncertaintes associated with simulating a dark sector in a Monte Carlo generator are likely to be larger than the discrepancies we observe here. Therefore, we conclude that the rescaling method is valid for our purposes.

6.5. Dark photon-like production of the ρ_D^0 meson

In addition to the production of the ρ_D^0 meson through dark showers initiated by the effective interaction between dark quarks and SM quarks, there are other potential production mechanisms that could contribute to the overall production rate of the ρ_D^0 meson in proton-proton collisions, such as at SHiP and NA62.

These include SM neutral meson decays, mixing with SM neutral vector mesons, proton bremsstrahlung and the Drell-Yan process. The processes are illustrated in Figure 6.7, and in Figure 6.8 we show the production probabilities of the ${\rho_D}^0$ meson through these mechanisms, as a function of m_{ρ_D}. Note that the proton bremsstrahlung production is not included in Figure 6.8 nor in our sensitivity estimates, as the theoretical uncertainties of this production mode are very large. Thus we take a conservative approach and exclude this production mode from our analysis. The uncertaintes of the Drell-Yan production are shown as the shaded region in Figure 6.8, and the uncertainties of the remaining dark-photon-like production modes are expected to be small and are therefore not shown (we refer the reader to Ref. [121,122] for details on the calculation of the production probabilities and their uncertainties).

These production mechanisms are similar to those of the dark photon, γ_D. This is because the dark photon and the ρ_D meson couple to the SM model through a similar kinetic mixing mechanisms. In fact, we can directly relate the coupling strength of the dark photon, ϵ, to the parameters of our model through the relation

$$\epsilon = \frac{2m_{\rho_D}^2}{\Lambda^2 g_{\pi\rho} e}, \tag{6.9}$$

where Λ is the suppression scale of the effective interaction between the dark ${\rho_D}^0$ and SM fermions, defined in Equation 4.22. This means that the production mechanisms of the dark photon will also exist for the dark ρ_D and can be adapted to the ρ_D meson in our model.

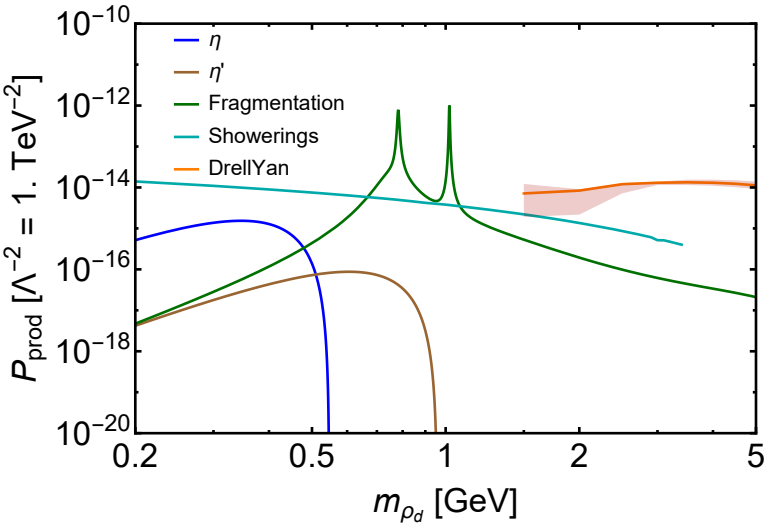

Figure 6.8.: Production probabilities of the ${\rho_D}^0$ meson, as a function of m_{ρ_D}, in the collision of the SPS proton beam with the Tungsten target, corresponding to the SHiP experiment. η and η' signify the decay of these mesons into ${\rho_D}^0$ mesons, while *Fragmentation* refers to the production of ρ_D^0 via mixing with SM neutral vector mesons in the final state radiation. The Drell-Yan production is also shown, and is only expected to happen for higher masses.

This raises the question whether we would be able to distinguish between a dark photon and a ρ_D meson if we were to observe a signal at SHiP. A crucial point here is that the ρ_D meson can be produced through an additional mechanism, the dark shower, which is not available to the dark photon. The dark shower has very distinct phenomenology that leads to signatures different from the other production mechanisms.

The dark shower can produce multiple ρ_D mesons in a single event, whereas other production mechanisms yield at most one FIP decay in the minimal γ_D model or a pair in non-minimal scenarios [123]. The non-minimal dark photon models considered in Ref. [123] include scenarios where 1) quadratic couplings lead to e.g. Higgs boson or B-meson decays into two dark photons, $h/B \to 2\gamma_D$, and 2) a short-lived resonance, χ, decays into a pair dark photons, $\chi \to 2\gamma_D$ In both cases, the maximum number of displaced vertices that can be observed in a single event is two.

Therefore, observing multiple displaced vertices in a single SHiP event would immediately rule out the minimal dark photon model. Moreover, if more than two displaced vertices are observed at a rate consistent with dark shower predictions, the non-minimal dark photon model could also be excluded.

If two or more decays are observed, Ref. [123] proposed that the invariant mass distribution of the reconstructed FIPs could be used to distinguish between the two models. We expect that the dark shower production mechanism would lead to a broad invariant mass distribution and no strict bound at higher energies, as long as $m_{Z'} \gg \sqrt{s}$. This is because the dark shower can produce ρ_D mesons with a wide range of energies, up to the kinematic limit set by the partonic energy available in the collision. This expectation is confirmed by the invariant mass distribution of sets of two or three ${\rho_D}^0$ meson decays originating from the dark showers simulated for this study, shown in Figure 6.9.

The non-minimal dark photon models are expected to produce sharp peaks around the mass of the parent particle, i.e. m_h or m_B for the quadratic coupling model, or m_χ for the resonance model. There is an exception to the quadratic coupling model, however. The B-mesons may undergo 3-body decays into two dark photons and an additional hadronic state,

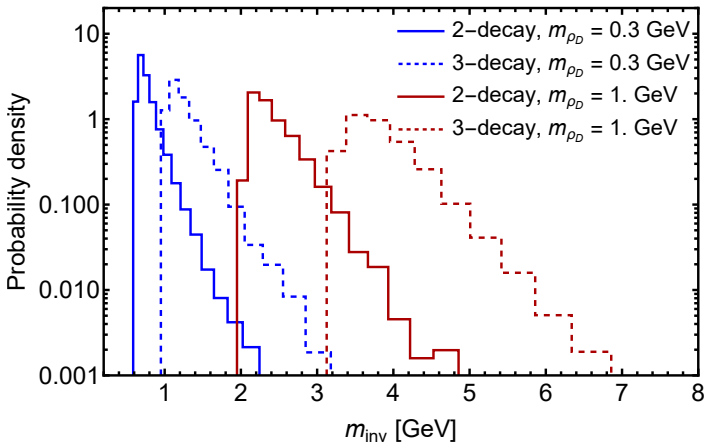

Figure 6.9.: Distribution of the invariant mass of ${\rho_D}^0$ mesons produced in the dark shower, and decaying within the decay volume of SHiP, for two (solid) and three (dashed) decaying dark rho mesons. The ${\rho_D}^0$ masses are $m_{\rho_D} = 0.3$ GeV (blue) and 1 GeV (red).

$B \to 2\gamma_D + Y$. In this case, the invariant mass distribution of the dark photons would be broad, similar to the dark shower case. However, the kinematic limit of the invariant mass distribution would be set by m_B, and so we would expect a sharp cutoff at m_B.

6.6. Projecting the sensitivity to the ρ_D^0 decay

Having established a reliable simulation framework for the dark shower, we now proceed to evaluate the sensitivity of the three experiments to the decay of ρ_D^0 mesons. We use separate frameworks for the Belle II case to the SHiP and NA62 cases.

In the next subsection, we describe the framework used for Belle II. For the SHiP and NA62 cases, we use the `SensCalc` and `EventCalc` frameworks [109,110]. These `Mathematica`-based tools offer two complementary methods for estimating the sensitivity of lifetime frontier experiments to FIPs. Supporting a wide range of FIPs - including heavy neutral leptons (HNLs), axion-like particles (ALPs), and, most relevant to this study, dark photons - the frameworks allow the user to import FIP distributions from external Monte Carlo generators such as Pythia, enabling the modeling of complex production mechanisms like dark showers. This flexibility makes them powerful and versatile tools for exploring diverse LLP models and their experimental signatures.

In this study, we employ both methods to assess the sensitivity of the SHiP experiment to the ρ_D meson, produced via dark showers (section 6.4) and dark photon-like mechanisms (section 6.5). While the `EventCalc` module will allow us to distinguish between mono-, di-, and tri-decay events, `SensCalc` will provide a complementary cross-check of our results. For the NA62 experiment, we only use the `SensCalc` module. We use the same simulated events for both SHiP and NA62, since both experiments take place at the SPS and therefore have the same beam energy. However, the different detector geometries and acceptances of SHiP and NA62 are taken into account in the sensitivity estimates via `SensCalc` and `EventCalc`.

6.6.1. Analysis for the Belle II search

The sensitivity at Belle II is estimated following the procedure outlined in Ref. [86]. In fact, the limits are very similar to those presented in Ref. [86], since the model and treatment thereof is identical to the one used in this study. One major difference is that the coupling $g_{\pi_D\rho_D} = 5.7$ in this study, whereas $g_{\pi_D\rho_D} = 1$ was used in Ref. [86]. This leads to a slightly

Table 6.2.: Selection criteria for displaced vertex reconstruction at Belle II, adapted from Ref. [86].

electron pairs	**muon pairs**
$p(e^+), p(e^-) > 0.1\,\text{GeV}$	$p(\mu^+), p(\mu^-) > 0.05\,\text{GeV}$
$m_{e^+e^-} > 0.03\,\text{GeV}$	$m_{\mu^+\mu^-} < 0.48\,\text{GeV}$ or $m_{\mu^+\mu^-} > 0.52\,\text{GeV}$
$\alpha(e^+, e^-) > 0.025$ rad	
Displaced vertex position	
$0.2\text{cm} < R < 0.9\text{cm}$ *or* $17\text{cm} < R < 60\text{cm}$	$0.2\text{cm} < R < 60\text{cm}$
$-55\,\text{cm} \leq z \leq 140\,\text{cm}$	
$17^\circ \leq \theta_{\text{lab}} \leq 150^\circ$	

higher lifetime of the ρ_D^0 meson in this study, and therefore we may go to higher masses before the sensitivity is lost due to the ρ_D^0 decaying too fast to detect a displaced vertex.

The dark shower, and production of ρ_D^0, is modeled using the same MadGraph and Pythia setup as described in section 6.4. The dark-photon-like production mechanisms are not included in the Belle II sensitivity estimate, as most of these are not expected in e^+e^- collisions, and generally the dark shower production mechanism is expected to dominate. Furthermore, the decays of the ρ_D^0 are simulated within Pythia, contrary to the procedure for SHiP and NA62, which we will outline in the next subsections. The displacement of the ρ_D^0 decay vertex is assigned to each ρ_D^0 meson based on an appropriate random distribution. More details on the Belle II procedure can be found in the original paper [86] (see in particular Section 3).

It is important to note that the estimates are based on a proposed search for Belle II. This search has not yet been performed, and therefore the sensitivity estimates are projections. The proposed search requires the event passes one of the existing Belle II triggers, or a new trigger specifically designed for displaced vertices. This trigger was initially proposed in [124] and requires at least one displaced vertex in the event with $0.9\,\text{cm} < R < 60\,\text{cm}$, which is formed from two tracks with $p_T > 100\,\text{MeV}$ and $38^\circ < \theta_{\text{lab}} < 127^\circ$ each. R is the distance of the decay vertex from the interaction point in transverse direction, and the angle θ_{lab} is defined as the angle between the vector of the decay vertex and the z-axis in the laboratory frame. After passing the trigger, the displaced vertex must satisfy the requirements listed in Table 6.2, which also includes geometric acceptance cuts. The cuts are slightly different for electron and muon pair final states, as shown in the table. The opening angle α is defined as the angle between the two decay products of the ρ_D^0 meson, and m is their invariant mass.

6.6.2. SensCalc

SensCalc provides a semi-analytic approach to estimate experimental sensitivity by predicting average decay rates and detector acceptances. This approach enables rapid sensitivity estimates that are ideal for feasibility studies and detector optimization.

The projected sensitivity is based on a number of inputs, specific either to the experiment or to the FIP model. The experimental inputs include the number of protons on target, the geometric acceptance of the detector, and the detection efficiency for the FIP decay products. The model-specific inputs include the production rate of the FIP, its lifetime and branching

ratios into detectable final states, and the double distribution of the FIP in energy and polar angle. While the lifetime and branching ratios can be calculated from theory, the cross section and kinematic distributions may be determined through Monte Carlo simulations, as described in section 6.4.

The expected number of observed events with a single LLP decay in the detector is given by [109]

$$N_{\text{ev}} = \sum_i N_{\text{prod}}^{(i)} \int \mathrm{d}E\, \mathrm{d}\theta\, \mathrm{d}z\, f^{(i)}(\theta, E) \cdot \epsilon_{\text{az}}(\theta, z) \cdot \frac{\mathrm{d}P_{\text{dec}}}{\mathrm{d}z} \cdot \epsilon_{\text{dec}}(m, \theta, E, z) \cdot \epsilon_{\text{rec}}, \tag{6.10}$$

where the sum runs over all production mechanisms i, $N_{\text{prod}}^{(i)}$ is the total number of ${\rho_D}^0$s produced via mechanism i, $\epsilon_{\text{az}}(\theta, z)$ is the azimuthal acceptance of the detector, $\frac{\mathrm{d}P_{\text{dec}}}{\mathrm{d}z}$ is the differential decay probability of the LLP at a distance z from the production point, and ϵ_{rec} is the reconstruction efficiency for the ${\rho_D}^0$s decay products. $f^{(i)}(\theta, E)$ is the normalized double differential distribution of the ${\rho_D}^0$ in polar angle θ and energy E, and we use the following cross section derived from the Monte Carlo simulation:

$$\sigma_{\text{prod}} = \sigma_{\geq 1 \rho_D} \times \langle N_{{\rho_D}^0} \rangle, \tag{6.11}$$

where $\sigma_{\geq 1 \rho_D}$ is the cross section for producing at least one ${\rho_D}^0$ meson in the event and $\langle N_{{\rho_D}^0} \rangle$ is the average multiplicity of the ${\rho_D}^0$ per event. Finally, $\epsilon_{\text{dec}}(m, \theta, E, z)$ is decay products acceptance, which can be further decomposed as

$$\epsilon_{\text{dec}} = \text{Br}_{\text{vis}}(m) \cdot \epsilon_{\text{geom}} \cdot \epsilon_{\text{other cuts}}, \tag{6.12}$$

where $\text{Br}_{\text{vis}}(m)$ is the branching ratio of the ${\rho_D}^0$ into final states that the experiment can detect, ϵ_{geom} is the geometric acceptance of the decay products, and $\epsilon_{\text{other cuts}}$ accounts for any additional selection criteria applied in the analysis.

As can be from the inputs required in Equation 6.10, `SensCalc` relies on average decay rates and acceptances to estimate the sensitivity. It does not treat events on an event-by-event basis, and therefore cannot account for correlations between multiple FIP decays in a single event. Instead, it treats events with n ${\rho_D}^0$ decays as n independent single ${\rho_D}^0$ decay events, implicitly assuming that the sensitivity to multiple decays is highly suppressed at the boundaries of the sensitivity region, such that the single decay phenomenology is a good approximation.

6.6.3. EventCalc

`EventCalc` is a different approach from `SensCalc`, as it is a Monte Carlo module that stochastically simulates FIP production and decay, generating event-by-event outcomes. A key feature of `EventCalc` is its ability to handle correlated LLP decays on an event basis, which is critical for models involving pair production or multiple displaced vertices.

Rather than use the double distribution of the FIP in energy and polar angle, `EventCalc` requires the four-momentum vectors of each FIP produced in the Monte Carlo simulation, sorted by event. The programme then inspects each ${\rho_D}^0$ and their decay products in a multi-step process that can be summarized as follows:

1. For each ${\rho_D}^0$:
    - Check if its trajectory intersects the experiment decay volume. Assign a geometric weight $\omega_{\text{dec vol}} = 1$ if it intersects, otherwise $\omega_{\text{dec vol}} = 0$.

- Sample the z position of the decay vertex using the inverse CDF (cumulative distribution function) of the decay probability:

$$\frac{dP_{\text{decay}}}{dz} = \frac{\exp\left[-\frac{z}{l_{\rho_d}}\right]}{l_{\rho_d}},$$

  where $l_{\rho_d} = c\tau_{\rho_d}\sqrt{\gamma^2 - 1}\cos(\theta)$ is the decay length of the ρ_D in the lab frame.

- Calculate the decay probability:

$$P_{\text{decay}} = \exp\left[-\frac{z_{\text{min}}}{l_{\rho_d}}\right] - \exp\left[-\frac{z_{\text{max}}}{l_{\rho_d}}\right],$$

  where $z_{\text{min/max}}$ are the boundaries of the decay volume.

2. For each decayed ${\rho_D}^0$:

   - Sample the phase space of its decay products by computing their 4-momenta in the ρ_d^0 rest frame, and then boosting the 4-momenta to the lab frame. For jet decays, use pre-tabulated phase space data from `PYTHIA8`. We consider only visible decay channels with a total branching ratio Br_{vis}.
   - Check if the decay products intersect the experiment decay volume and satisfy applied cuts, such as energy, transverse impact parameter etc. Assign a decay weight; $\epsilon_{\text{dec}} = 1$ if the decay products intersect the decay volume and satisfy the cuts, otherwise $\epsilon_{\text{dec}} = 0$.

3. Assign a weight to the kth ρ_d^0 from the ith event:

$$\omega_{i,k} = \omega^{i,k}_{\text{dec vol}} \times P^{i,k}_{\text{decay}} \times \text{Br}_{\text{vis}} \times \epsilon^{i,k}_{\text{dec}}.$$

Finally, we may calculate the rate of events with m decaying ${\rho_D}^0$s:

$$N^{(m)}_{\text{events}} = N_{\text{PoT}} \cdot \frac{\sigma_{\geq 1\rho_d}}{\sigma_{pN}} \cdot \frac{1}{N_{\text{sample}}} \sum_{i=1}^{N_{\text{sample}}} h(n_i - m) \sum_{\{m\}} \prod_{k\in\{m\}} \omega_{i,k} \prod_{t\notin\{m\}} (1 - \omega_{i,t}), \tag{6.13}$$

where N_{PoT} is the number of protons on target and $h(n_i - m)$ is the step function, ensuring exactly m decays are selected. $\sigma_{pN} = 51\ A^{-0.29}_{\text{target}}$ mb is the proton interaction cross-section per nucleon for the experiment's target, and $\sigma_{\geq 1{\rho_D}^0}$ is the cross-section for producing at least one ${\rho_D}^0$.

6.6.4. Uncertainty in projections resulting from the dark sector simulation

The projections are naturally dependent on the results of our simulation of the dark sector and dark ρ_Ds in Pythia, which are dependent on our choice of several parameters that we do not have a clear expectation of from the theory or that may turn out to be different than expected. Two such parameters are the `probVec` setting in Pythia, and Λ_D. To further our understanding of the impact of uncertainties stemming from variations in these parameters, we project the variations in sensitivity at SHiP as we vary these parameters. We must do the full projection procedure, because the number of events in an experiment is influenced not just by the overall production yield, but also by factors such as the kinematics of the dark rho mesons and their multiplicities, all of which depend on the specific simulation parameters.

In Figure 6.10, we show the number of events at SHiP as a function of Λ^{-2}, considering different choices for `probVec` and the scale Λ_D. We analyze events with 1, 2, or 3 reconstructed decaying dark rho mesons per event. For small m_{ρ_D} values and the single-decay signature, the uncertainties have little to no impact on the results. However, for larger dark rho meson masses and signatures involving 2 or 3 decays, the variation can exceed an order of magnitude.

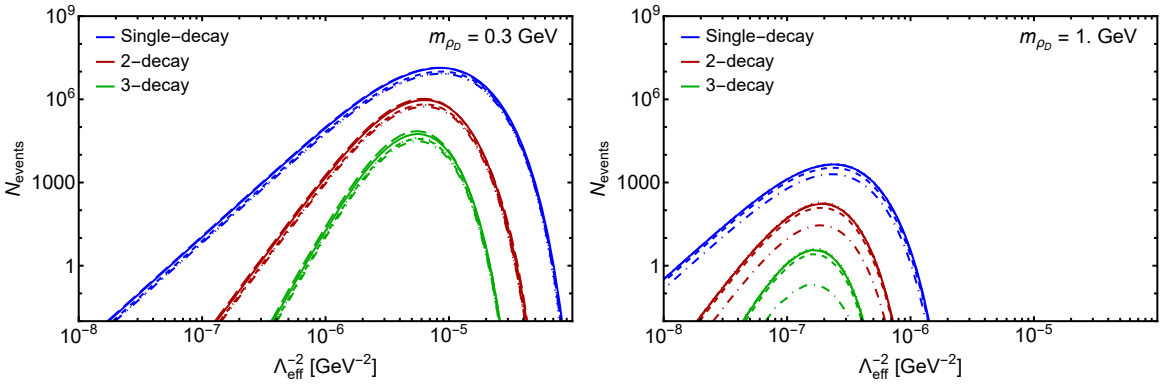

Figure 6.10.: Impact of varying the parameters in the dark shower simulation on the event yields with one (blue), two (red), and three (green) decaying dark rho mesons per event at SHiP. We show two masses; $m_{\rho_D} = 0.3$ GeV (left) and 1 GeV (right). For each color the five line styles denote different parameter choices: *solid* (our general set-up); *short-dash* ($\Lambda_D = \frac{1}{3}\Lambda_D^{\text{default}}$); *long-dash* ($\Lambda_D = 3\,\Lambda_D^{\text{default}}$); *dash-dot* (`probVec`$= 0.33$); *dotted* (`probVec`$= 0.75$).

6.7. Results

We show the result for mono-decays at all three experiments in Figure 6.11. The curves correspond to the full statistics projected for each experiment. The grey region is excluded with results currently obtained by NA62, as well as results from the older CERN experiments BEBC [125, 126] and CHARM [127, 128]. These estimates are based on the $r_m = 1.5$ model. The results for $r_m = 1.9$ are confirmed to not differ significantly, with the only noticeable difference being at the upper boundary of the sensitivity region, where $r_m = 1.5$ yields a slightly better sensitivity due to the larger mean energies of the $n \times \rho_D^0$ particles.

The shape of the sensitivity curves is typical for LLP searches at beam dump experiments. At low values of Λ (the upper boundary), the ρ_D^0 mesons are very short-lived and tend to decay before reaching the decay volume, for which the experiments cannot reconstruct the decay vertex and thus are not senstitive to. At very high values of Λ (the lower boundary), the ρ_D^0 mesons become so long-lived that they tend to decay outside the decay volume, again leading to a loss of sensitivity. The sensitivity is maximized at intermediate values of Λ, where the ρ_D^0 mesons have a significant probability of decaying within the decay volume.

The sensitivity also depends on m_{ρ_D}, as this affects both the production rate and the lifetime of the ρ_D^0 mesons. Generally, lower masses lead to higher production rates and higher multiplicity events. In line with our discussion in section 4.3, we cannot reliably simulate arbitrarily small masses, but we have validated our rescaling method to go as low as $m_{\rho_D} = 200$ MeV. To relate it to the π_D mass, this corresponds to $m_{\pi_D} \approx 100$ MeV for $r_m = 1.9$ and $m_{\pi_D} \approx 130$ MeV for $r_m = 1.5$. This is an interesting mass range for its ability to explain the dark matter relic abundance, and a lower mass would conflict with constraints from the Bullet Cluster.

We see two distinct dips in the sensitivity curves of SHiP and NA62 around ≈ 0.78 GeV and ≈ 1 GeV. These correspond to resonances with the SM ρ/ω and ϕ mesons, respectively, where the mixing between the ρ_D^0 and the SM mesons is enhanced, leading to increased production rates. At these points, both NA62 and SHiP are more sensitive to larger values of the suppression scale, Λ, corresponding to smaller couplings between the dark sector and the SM, κ. Especially for NA62 we see this effect, as we project no sensitivity to the regions between these two resonances or beyond the second resonance. However, we also loose sensitivity slightly at SHiP around the upper boundary, where the lifetime of the ρ_D^0 meson is reduced

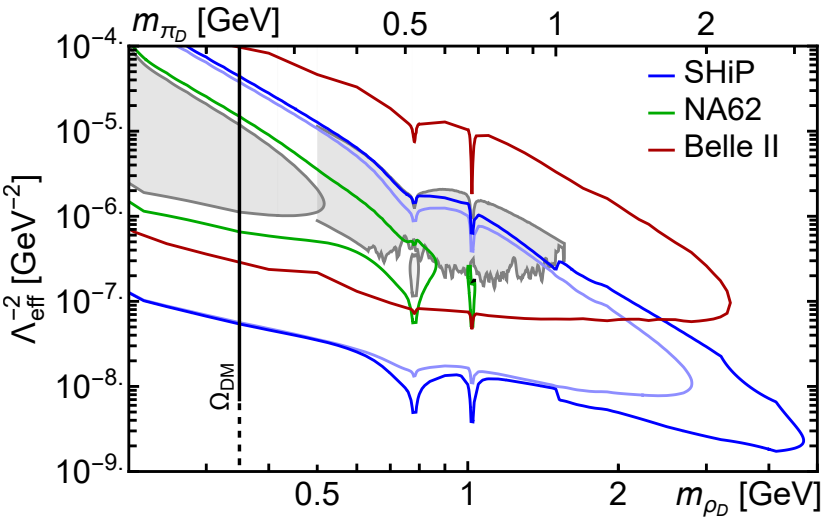

Figure 6.11.: Projected sensitivity to ρ_D^0 mono-decay events at SHiP, NA62 and Belle II. The curves represent 2.3 signal events (assuming zero background). The grey region at $m_{\rho_D} \lesssim 0.5$ GeV as well as the small closed grey region around $m_{\rho_D} \sim 0.78$ GeV show constraints from BEBC, CHARM, and NA62 (with 1.4×10^{17} PoT), while the grey region between $m_{\rho_D} \sim 0.5$ and ~ 1.6 GeV shows constraints from BaBar. For SHiP esitmates, the outer blue line accounts for all ρ_D^0 production mechanisms, and the inner, lighter blue line accounts for dark shower production only. The vertical line indicates the mass points where we obtain the correct relic abundance of dark pions for $r_m = 1.5$ (see main text for details).

due to the enhanced mixing, leading to more ρ_D^0 decaying too fast before reaching the decay volume.

For the Belle II sensitivities, we see a similar shape of the sensitivity curve, with a few key differences in the sensitivity reach. Despite the lower center-of-mass energy, Belle II is able to probe slightly higher m_{ρ_D} than SHiP for the dark shower production mode only, due to the higher collision energy of the e^+e^- compared to the partonic energy at SHiP. Generally, Belle II is sensitive to slightly lower values of Λ, corresponding to larger couplings κ, where SHiP and NA62 lose sensitivity due to the shorter lifetimes. The proposed search at Belle II is therefore complementary, as it probes a region of parameter space that cannot be covered by the other two experiments.

The correct relic abundance, $\Omega_{\rm DM}h^2 = 0.12$, is obtained for $m_{\rho_D} = 318$ MeV ($m_{\pi_D} = 212$ MeV) for $r_m = 1.5$, and $m_{\rho_D} = 442$ MeV ($m_{\pi_D} = 233$ MeV) for $r_m = 1.9$. To arrive at these results, we have used the procedure and code described in chapter 5. The relic abundance is independent of Λ as long as the (inverse) decays of the dark rho meson are rapid enough to maintain equilibrium between the dark rho mesons and the SM bath during the freeze-out of the dark pions. Following the discussion in section 5.3, we know that this condition is satisfied if $\Gamma_{\rho_D}/H \gtrsim x$ at the time of freeze-out. For a dark rho meson mass of $m_{\rho_D} = 318$ MeV, this equilibrium condition implies that $\Lambda^{-2} \gtrsim 7 \times 10^{-9}$ GeV^{-2}. This sets a lower bound on the parameter space where $3\pi_D \to \pi_D\rho_D$ annihilations can determine the dark matter relic density without being constrained by the strength of the interaction between the dark sector and the SM. We represent this in the relic density line with a dotted line for smaller values of Λ^{-2} in Fig. 6.11.

We see that all three experiments are sensitive to this mass range, and that NA62 is already able to exclude this point for the suppression scale at $\Lambda \sim 10^{2.5-3}$ GeV. SHiP will be able to

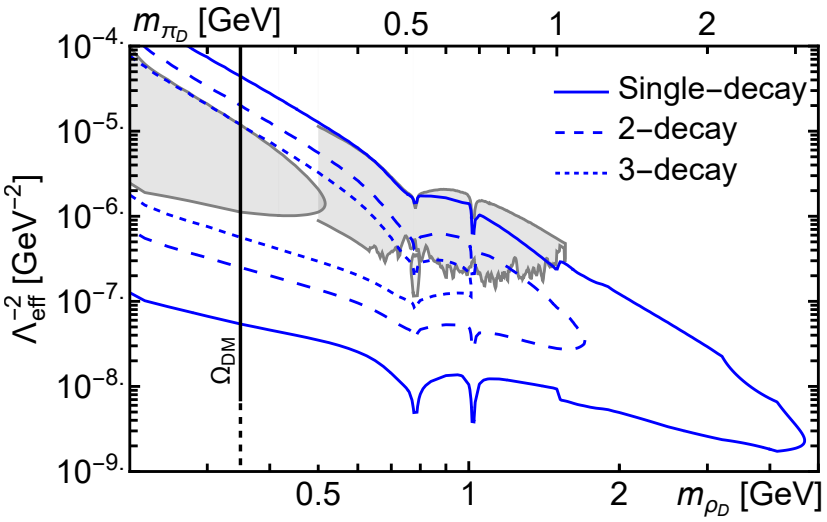

Figure 6.12.: SHiP sensitivity to ρ_D^0 mono-, di- and tri-decay events, obtained using the `EventCalc` module. The curves represent 2.3 signal events (assuming zero background). The grey region at $m_{\rho_D} \lesssim 0.5$ GeV as well as the small closed grey region around $m_{\rho_D} \sim 0.78$ GeV show constraints from BEBC, CHARM, and NA62 (with 1.4×10^{17} PoT), while the grey region between $m_{\rho_D} \sim 0.5$ and ~ 1.6 GeV shows constraints from BaBar. The vertical line indicates the mass points where we obtain the correct relic abundance of dark pions for $r_m = 1.5$.

probe this to a larger value of Λ around these mass points, approximately up to $\Lambda \sim 10^{3.5}$ GeV. Meanwhile, Belle II would cover a significant range of lower values of Λ, approximately down to $\Lambda \sim 10^2$ GeV.

The non-smoothness of the Belle II upper sensitivity curve in Figure 6.11 is due to simulation artefacts. At this boundary, the sensitivity is exponentially sensitive to the lifetime of the ρ_D^0 meson. The simulation artefacts therefore arise from the interpolation in the Λ-m_{ρ_D} plane.

Figure 6.12 shows the sensitivity of SHiP to mono-, di- and tri-decay events of the ${\rho_D}^0$ meson, obtained using the `EventCalc` module. By comparing the mono-decay sensitivity in Figure 6.12 to that obtained with `SensCalc` in Figure 6.11, we see that the two methods yield very similar results, providing a good cross-check of our findings and confirming our assumption that the sensitivity to multiple decays is highly suppressed at the boundaries of the sensitivity region.

The di- and tri-decay sensitivities are weaker than the mono-decay sensitivity, as expected. They loose sensitivity rapidly at high m_{ρ_D}. We expect this as the probability of producing n number of ρ_D^0 in a single event decreases quickly with increasing m_{ρ_D}, and becomes kinematically forbidden when $n \times m_{\rho_D} > \sqrt{\tilde{s}}$ (which we approximated to be ~ 4 GeV at SHiP). The upper and lower boundaries are also expected to be weaker, as the probability of multiple ρ_D^0 decaying within the decay volume is also lower.

CHAPTER 7

Reinterpreting LHC Dark Shower Searches

In subsection 4.2.3 we introduced the concept of dark showers, which are the result of the hadronization of dark mesons in a strongly-interacting dark sector. In this chapter, we will dive deeper into the signatures of dark showers at the LHC, where we will focus on five existing searches, that together cover three of the four different scenarios that we introduced in subsection 4.2.3 (excluding emerging jets). We summarize these searches in section 7.1. We will then discuss how these searches can be recast in the context of a specific dark shower model, and in section 7.3 we present the case for recasting the CMS EXO-19-020 search for semi-visible jets [129] in MadAnalysis 5 [130, 131].

In recent years, several groups have proposed various benchmark models for dark showers (reviewed in Ref. [3]), but it is clear that it is not possible to encapsulate all the different signatures of dark showers in a single model. This is because the signatures cover a wide range of phenomena and can depend strongly on the details of the dark sector, such as the mass scale of the dark mesons, the nature of the portal, the coupling strength and the mass of the mediator. Therefore, it is important to have a flexible framework that can easily accommodate different dark shower models and allow for the recasting of existing searches in a consistent way. In particular, it would be beneficial to be able to understand how different searches can be complementary, or if they overlap and are redundant, as well as identify what future search strategies are best suited for different scenarios.

MadAnalysis 5 is the most powerful tool for the recasting of LHC searches. It is designed to perform sophisticated analyses on event files, making it possible to reinterpret existing search analyses on any model that the user has simulated with event generators such as Pythia. Thus, we may simulate our chosen dark shower model and then use MadAnalysis 5 to recast several existing LHC searches in the context of this model.

To reinterpret a search, one must implement the original analysis, including its selection cuts and statistical methods. The recast must then be validated by reproducing simulated signals and comparing the results to those of the original to ensure consistency[8].

[8] This is of course only possible if all the necessary information is available from the original search. This is not always the case, but there are active community efforts dedicated to improving awareness and collaboration on this topic [132].

7.1. Dark shower searches at the LHC

We focus on five LHC searches, across both ATLAS and CMS, that are sensitive to either semi-visible jets, dark jets, or invisible jets. Together, these searches touch upon three of the four scenarios of dark showers that we introduced in subsection 4.2.3 - emerging jets or displaced vertices being excluded.

7.1.1. CMS s-channel semi-visible jets search (EXO-19-020)

In 2022, the CMS published the first collider search specifically designed for dark showers with an exclusive focus on semi-visible jets [129]. The benchmark model that they investigated describes a QCD-like dark sector with two dark mesons, π_D and ρ_D, and a leptophobic vector portal, Z', to the SM with a mass in the TeV range. While the basic content is very similar to the dark sector setup we introduced in section 4.1, the details are very different and the model that CMS studied is inconsistent with what we would expect from a realistic dark sector. This makes it very interesting for recasting purposes, as the exclusions to more consistent models may be different from the ones obtained in the original search.

This analysis utilizes data collected by the CMS detector at during the 2015–2018 data-taking period, corresponding to a total integrated luminosity of 138 fb^{-1}.

The CMS signature model assumes for simplicity that the two dark mesons have the same mass, $m_{\pi_D} = m_{\rho_D} = m_{\text{dark}}$, and that the dark quark mass is $m_{q_D} = \frac{1}{2}m_{\pi_D}$. As we've seen in section 4.1, this is not consistent with expectations from the theory of strongly interacting dark sectors. Furthermore, it assumes that both mesons can come in stable or unstable flavors, and the ratio of stable mesons is a varying parameter that is equivalent to the phenomenological parameter r_{inv} and allowed to take on any value between 0 and 1. In a consistent model, we will not be able to vary this parameter freely, as it is a function of the dark sector structure and parameters. Setting $N_{f_D} = 2$, $N_{c_D} = 2$, the model has five free parameters, summarized in Table 7.1.

Table 7.1.: Summary of the CMS-EXO-19-020 dark sector parameters [129].

Parameter	Description	Scan range
$\sigma_{Z'}\mathcal{B}(Z' \to q_D\bar{q_D})$	Effective cross section	limit-setting
$m_{Z'}$	Mass of the Z' vector mediator	2.1 - 5.1 TeV
m_{dark}	Mass of the dark mesons	1 - 100 GeV
α_{dark}	Dark coupling strength	$\alpha_{\text{dark}}^{\text{low}}$ - $\alpha_{\text{dark}}^{\text{high}}$
r_{inv}	Ratio of stable to all dark mesons	0 - 1

The dark coupling is defined as

$$\alpha_{\text{dark}}(\Lambda_{\text{dark}})) = \frac{6\pi}{11N_{c_D} - 2N_{f_D}} \frac{1}{\ln(Q_{\text{dark}}/\Lambda_{\text{dark}})}, \tag{7.1}$$

where Λ_{dark} is the dark coupling scale, and Q_{dark} is chosen to be 1 TeV. The CMS search assumes a peak value of Λ_{dark} at $\Lambda_{\text{dark}}^{\text{peak}} = 3.2(m_{\text{dark}})^{0.8}$. $\alpha_{\text{dark}}^{\text{high}}$ and $\alpha_{\text{dark}}^{\text{low}}$ then take on $\pm 50\%$ of this value.

The search variable is the dijet transverse mass, defined as

$$\begin{aligned} m_T^2 &= [E_{\text{T,JJ}} + E_T^{\text{miss}}]^2 - [\vec{p}_{\text{T,JJ}} + \vec{p}_T^{\text{miss}}]^2 \\ &= m_{JJ}^2 + 2p_T^{\text{miss}}[\sqrt{m_{JJ}^2 + p_{T,JJ}^2} - p_{\text{T,JJ}}\cos(\phi_{\text{JJ,miss}})], \end{aligned} \tag{7.2}$$

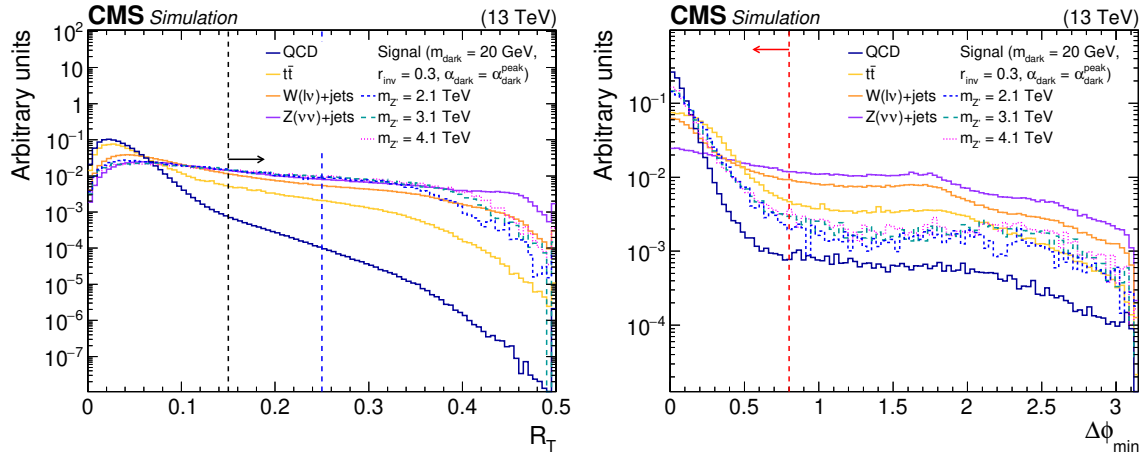

Figure 7.1.: The The normalized distributions of the characteristic variables R_T and $\Delta\phi_{\text{min}}$ for the simulated SM backgrounds and several signal models. For each variable, the requirement on that variable is omitted, but all other preselection requirements are applied. The black (red) vertical dotted line indicates the preselection (final selection) requirement on the variable, if any. The blue vertical dotted line indicates the boundary between different signal regions. For the CMS EXO-19-020 search [129]

where m_{JJ} is the invariant mass of the two jets with the highest p_{T}, $\vec{p}_{\text{T,JJ}}$ is the vector sum of their transverse momenta, and they have assumed $E^2_{\text{T,JJ}} = m^2_{JJ} + |\vec{p}_{\text{T,JJ}}|^2$ and $E^{\text{miss}}_T = p^{\text{miss}}_T$.

The search also utilizes two other important variables, the transverse ratio R_T and the minimum angle $\Delta\phi_{\text{min}}$ variables, which are defined as

$$R_T = \frac{p^{\text{miss}}_{\text{T}}}{m_{\text{T}}}, \tag{7.3}$$

$$\Delta\phi_{\text{min}} = \min[\Delta\phi(\vec{\text{J}}_1, \vec{p}^{\,\text{miss}}_T), \Delta\phi(\vec{\text{J}}_2, \vec{p}^{\,\text{miss}}_T)]. \tag{7.4}$$

These variables are key to eliminating the majority of the SM background, which is dominated by QCD processes. Applying rhe selection cut on $R_T > 0.15$ rejects 99% of the simulated QCD background. The distributions of these two characteristic variables are shown in Figure 7.1 for the simulated SM backgrounds and several signal models.

Table 7.2.: The CMS EXO-19-020 preselection and final selection requirements. The symbol * indicates a selection applied only to the later portion of the 2018 data. [129]

Preselection requirements
$p_{\text{T}}(\text{J}_{1,2}) > 200\,\text{GeV},\ \eta(\text{J}_{1,2}) < 2.4$
$R_{\text{T}} > 0.15$
$\Delta\eta(\text{J}_1, \text{J}_2) < 1.5$
$m_{\text{T}} > 1.5\,\text{TeV}$
$N_\mu = 0$
$N_{\text{e}} = 0$
$p^{\text{miss}}_{\text{T}}$ filters
$\Delta R(\text{j}_{1,2}, c_{\text{nonfunctional}}) > 0.1$
Final selection requirements
veto $f_\gamma(\text{j}_1) > 0.7$ & $p_{\text{T}}(\text{j}_1) > 1.0\,\text{TeV}$
veto $-3.05 < \eta_{\text{j}} < -1.35$ & $-1.62 < \phi_{\text{j}} < -0.82$ *
$\Delta\phi_{\text{min}} < 0.8$

A full summary of the preselection and final selection requirements is given in Table 7.2. The first preselection requirements are designed to select events with two energetic leading jets, $p_T > 200$ GeV, that are back-to-back, $\eta < 2.4$, and have a minimum dijet transverse mass of 1.5 TeV. The search also includes vetos on electrons and muons to reduce the $t\bar{t}$ and $W(\to \ell\nu) +$ jets backgrounds. Additionally, it applies several cuts to reduce the risk of misreconstructed jets, and mitigate known detector defects, such as nonfunctional channels. This will be discussed in more details in subsection 7.3.1 (or see the original paper [129]).

The production of the Z', the decay into a dark quarks and anti-quark pair and the subsequent dark shower are all simulated in Pythia 8 and the Pythia card is available on the HEPData page for the analysis. To simulate the detector effects, the events are passed through the Delphes detector simulation framework [133]. The Delphes card is not available at HEPData, but the original card used was provided upon request. It is a standard HL-LHC delphes card with all dark sector particle PIDs as well as PIDs 51 and 53 defined as invisible states. The PIDs 51 and 53 are used to signify the fraction of stable dark mesons. This is because the Pythia card is written such that all dark mesons decay promptly, but with a branching ratio of r_{inv} into particles with PID 51 or 53.

7.1.2. ATLAS t-channel semi-visible jets search (EXOT-2022-37)

Another LHC search for semi-visible jets was performed by ATLAS in 2023 [134]. This search is based on a t-channel model, where the dark quarks are produced via a t-channel exchange of a scalar mediator that couples to the dark quarks and SM quarks. The t-channel results in non-resonant production of the semi-visible jets, and therefore a bump-hunt search will not do, and the applied search strategy is different from the CMS s-channel search.

This analysis utilizes data collected by the ATLAS detector at during the 2015–2018 data-taking period, corresponding to a total integrated luminosity of 139 fb^{-1}.

The analysis targets events with high missing transverse energy, E_T^{miss}, and at least two jets. The main contribution to the signal is still expected to be from events with two back-to-back semi-visible jets and p_T^{miss} aligned with one of the jets, but also considers the possibility of boosting from additional jets, leading to more complex event topologies. The main SM backgrounds are $W/Z +$ jets, $t\bar{t}$, single top, multijet, and diboson events.

The selection cuts are summarized in Table 7.3, although this is not a complete list of all the cuts. The full description of selection cuts can be found in the original paper [134]. Notably, it does not define the two jets to be analyzed as the two leading jets in p_T, but rather the jets closest (J_1) and farthest (J_2) in azimuthal direction, ϕ, from the p_T^{miss} direction. These must have at least $p_T = 30$ GeV and be within $|\eta| < 2.8$.

The dark sector model applied in this search also suffers from inconsistencies with the theory of strongly interacting dark sectors. Their model assumes $N_{f_D} = 1$, which is a special case that does not give rise to Goldstone bosons, and therefore is not expected to contain a dark pion[9] [135]. Despite this, the model includes both a dark pion and a dark rho meson, and furthermore, it distinguishes between diagonal and off-diagonal mesons - which is only expected from models with $N_{f_D} \geq 2$. This makes the analysis a perfect candidate for recasting the analysis, as the exclusions obtained in the original search may change within a more consistent model.

The diagonal π_D and ρ_D mesons have mass 10 and 20 GeV, respectively, while the off-diagonal mesons have mass 4.99 GeV and 9.99 GeV. The diagonal mesons are expected to decay promptly into either the off-diagonal mesons, which are stable, or SM quarks. The

[9] It was also noted by theorist in Ref. [3] that the special case of $N_{f_D} = 1$ should be treated with extra care.

Table 7.3.: The key selection cuts of the ATLAS EXOT-2022-37 search [134].

Preselection requirements
$E_T^{\text{miss}} > 250$ GeV
$p_T^{\text{leading jet}} > 250$ GeV, $\lvert\eta(J_1)\rvert < 2.8$
$\Delta\phi_{\text{min}} \leq 2.0$
SR selection requirements
$E_T^{\text{miss}} > 600$ GeV
$H_T > 600$ GeV
Veto events with p_T(electron, muon) > 7 GeV

branching fraction of visibly decaying mesons is r_{inv}. The dark quark mass is set to 10 GeV, and the dark confinement scale is set to $\Lambda_D = 6.5$ TeV. Finally, the coupling strength between the dark sector and the SM is chosen to be $\lambda = 1$. The parameters of the model that are varied during the search are summarized in Table 7.4.

Table 7.4.: Summary of varied parameters in the ATLAS EXOT-2022-37 search [134].

Parameter	Description	Scan range
m_ϕ	Mass of the scalar mediator ϕ	1-5 TeV
r_{inv}	Ratio of stable to all dark mesons	0.1 - 0.9

This search simulates the hard process of the signal events in MadGraph5_aMC@NLO, and then passes the events to Pythia 8 for the dark shower using the HV module. The detector effects are simulated with Geant4 [136].

The search employs a binned maximum likelihood to four kinematic distributions, E_T^{miss}, H_T, p_T^{bal} and $|\phi_{\text{max}} - \phi_{\text{min}}|$, to set exclusion limits on r_{inv}, m_ϕ and λ. The p_T balance between the two leading jets is defined as

$$p_T^{\text{bal}} = \frac{|\vec{p}_T(J_1) + \vec{p}_T(J_2)|}{|\vec{p}_T(J_1)| + |\vec{p}_T(J_2)|}. \tag{7.5}$$

The variable $|\phi_{\text{max}} - \phi_{\text{min}}|$ is the azimuthal angle between the two selected jets. These two variables are used to define the 9 SR and CR bins. The distributions of these two variables are shown in Figure 7.2 for the simulated SM backgrounds and several signal models.

A simultaneous binned maximum-likelihood fit is performed across the SR and CR to estimate the signal strength μ and improve background predictions. Systematic uncertainties are included as nuisance parameters with Gaussian constraints, and correlations across bins and regions are taken into account. The signal strength μ, defined as the ratio of observed to predicted signal cross-section, is extracted from the fit, and its uncertainty is determined by considering all correlated uncertainties. Upper limits on new physics contributions are set using the modified frequentist CL_s method at 95% confidence level.

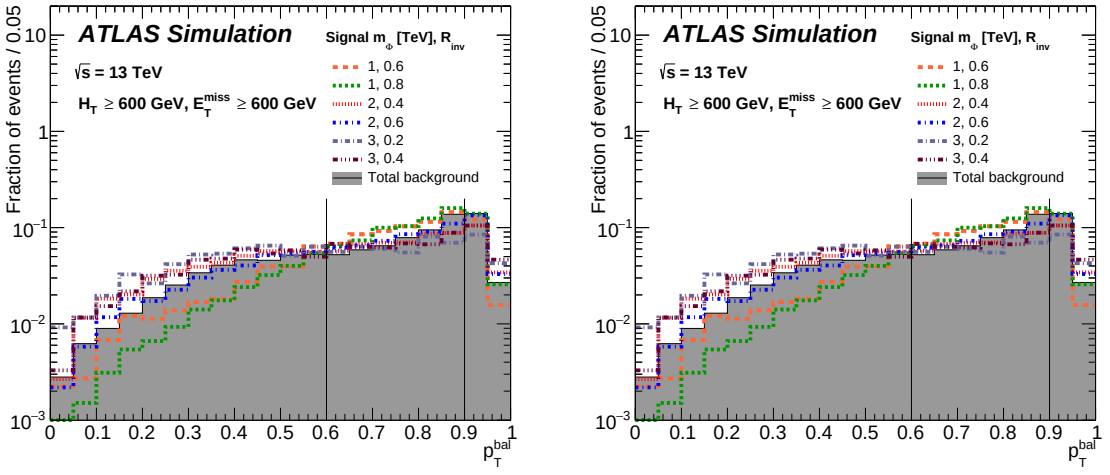

Figure 7.2.: The distributions of p_T^{bal} and $|\phi_{\max} - \phi_{\min}|$ for the simulated SM backgrounds and several signal models in the ATLAS EXOT-2022-37 search. The solid vertical lines indicate the division of the bins. [134]

7.1.3. ATLAS dark jets search (HDBS-2018-45)

Moving away from semi-visible jets, we now consider a search for dark jets performed by ATLAS in 2024 [137]. This search is sensitive to the phenomenology of dark showers where approximately all dark mesons decay promptly into SM particles, leading to dark jet signatures. The search assumes a heavy Z' portal that couples to both dark quarks and SM quarks, producing a dark quark pair resonantly at LHC. The production is analogous to the CMS s-channel semi-visible jet search, however, the parameter choices and decay patterns differ substantially, leading to a distinct phenomenology.

This analysis utilizes data collected by the ATLAS detector at during the 2015–2018 data-taking period, corresponding to a total integrated luminosity of 139 fb^{-1}.

The analysis considers four benchmark models, adapted from [138], and summarized in Table 7.5. Across these four setups, the Z' mass is varied between 1.5 and 3.5 TeV. The dark ρ_D is assumed to always decay via $\rho_D \to \pi_D \pi_D$. In models A and B, the π_D decays directly into SM quarks, while in models C and D, it decays into a pair of dark photons, $\pi_D \to \gamma'\gamma'$, which subsequently decay into SM fermions. The dark photon mass is set to 4 GeV in model C and 0.7 GeV in model D.

Table 7.5.: Benchmark dark sector model parameters and π_D decay modes in the ATLAS HDBS-2018-45 search [137].

Model	N_{f_D}	$\tilde{\Lambda}_D$ (GeV)	$m_{q'}$ (GeV)	m_{π_D} (GeV)	m_{ρ_d} (GeV)	π_D decay mode
A	2	15	20	10	50	$\pi_d \to \bar{c}c$
B	6	2	2	2	4.67	$\pi_d \to \bar{s}s$
C	2	15	20	10	50	$\pi_d \to \gamma'\gamma'$ with $m_{\gamma'} = 4.0$ GeV
D	6	2	2	2	4.67	$\pi_d \to \gamma'\gamma'$ with $m_{\gamma'} = 0.7$ GeV

The search strategy is based on the identification of events with high track multiplicity, which are expected from a dark jet as the parton shower occurring inside the dark sector can

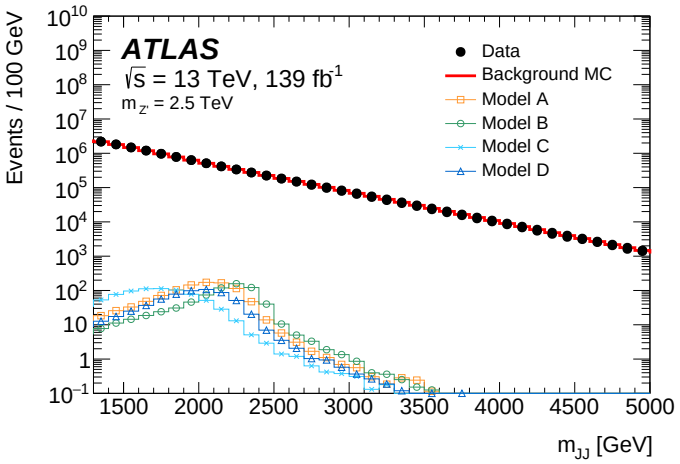

Figure 7.3.: The distributions of m_{JJ} for the ATLAS data, simulated SM backgrounds and the four signal models with $m_{Z'} = 2.5$ TeV in the ATLAS HDBS-2018-45 search. The simulated background is normalised to the data and the signals are normalised to a production cross-section of 10 fb. [137]

lead to high multiplicity of dark mesons that subsequently decay to SM particles. Low-track multiplicity events are used as control regions. It uses relatively "fat" jets, reconstructed with the anti-k_t algorithm with a radius parameter of $R = 1.0$. This is another expected key feature of dark jets, as the dark shower can lead to a broader jet structure compared to standard QCD jets.

The search variable is the invariant mass, m_{JJ}, of the two highest p_T jets. While the invariant mass is not an appropriate search variable for semi-visible jets, as the missing energy from the invisible dark mesons will distort the invariant mass distribution, it is a suitable variable for dark jets. The background distribution is expected to be smooth, whereas a dark jet event originating from a new resonance will introduce an enhancement around the resonance mass. The distributions of m_{JJ} for the ATLAS data, simulated SM backgrounds and the four signal models with $m_{Z'} = 2.5$ TeV are shown in Figure 7.3.

The signal models are simulated in Pythia 8 using the Hidden Valley module, and the detector effects are simulated with Geant4. Using a profile likelihood ratio test, the search sets exclusion limits on the effective production cross section of the Z', $\sigma_{Z'}\mathcal{B}(Z' \to q_D\bar{q_D})$, as a function of its mass.

7.1.4. ATLAS dijet resonance search (EXOT-2019-03)

The ATLAS dijet resonance search [139] is a general search for new resonances in the dijet invariant mass. It is not specifically designed for dark showers, but it is expected to be sensitive to the phenomenology of dark jets, as this could also lead to an excess in the dijet mass spectrum - similar to the situation described above.

This analysis utilizes data collected by the ATLAS detector at during the 2015–2018 data-taking period, corresponding to a total integrated luminosity of 139 fb^{-1}.

The search considers several signal models, including a leptophobic Z' dark matter mediator. However, the dark shower is not simulated in this search, and the Z' is assumed to decay directly into SM quarks. We could imagine that the Z' instead decays into a dark quark pair and produces a dark shower that then decays into SM particles with a low r_{inv} ratio. This would make it highly visible - like the direct Z' to SM case - and would lead to a distinct

Table 7.6.: Selection requirements and signal models being tested in each analysis category, for the ATLAS EXOT-2019-03 search. Full details on the signal models can be found in the original analysis from ATLAS [139]

Category	**Inclusive**		**1b**	**2b**
Jet p_T	> 150 GeV			
$\lvert\Delta\phi(jj)\rvert$	$\lvert\Delta\phi(jj)\rvert > 1.0$			
Jet $\lvert\eta\rvert$	-		< 2.0	
$\lvert y^*\rvert$	< 0.6	< 1.2	< 0.8	
m_{jj}	> 1100 GeV	> 1717 GeV	> 1133 GeV	
b-tagging	no requirement		1 b-tagged jet	2 b-tagged jets
Signal models	DM mediator Z' W' q^* QBH Generic Gaussian	W*	b^* Generic Gaussian	DM mediator Z' $(b\bar{b})$ graviton $(b\bar{b})$ Generic Gaussian

phenomenology. Whether this would lead to a stronger or weaker exclusion is not clear, and it is therefore interesting to recast this search in the context of a dark shower model.

The coupling between the Z' and SM quarks is varied between $g_q = 0.1 - 0.5$, which at the upper limit corresponds to a 12% width to resonance mass ratio, meaning the resonance peak would be rather broad, and is expected to be at the edge of the sensitivity of the search. The production and decay of the Z' is simulated in MadGraph5_aMC@NLO, and the detector effects are simulated with Geant4.

The search is performed in three categories: inclusive, 1 b-tagged jet, and 2 b-tagged jets. The search variable is the dijet invariant mass, m_{jj}, of the two highest p_T jets. The selection requirements and signal models tested for each category are summarized in Table 7.6. The distributions of m_{jj} for the ATLAS data, simulated SM backgrounds and a Z' signal model with $m_{Z'} = 3.5$ TeV are shown in Figure 7.4.

Localized excess in the dijet mass spectrum are analyzed using BumpHunter [140, 141] to search for localized excesses in the dijet invariant mass spectrum over a smoothly falling background. BumpHunter systematically scans the spectrum using sliding mass windows of varying widths, comparing the observed event counts to the background-only expectation in each window. The interval showing the greatest deviation from the smooth background spectrum is identified as the set of bins with the lowest probability of resulting from a Poisson background fluctuation.

7.1.5. CMS monojet search (PAS-EXO-20-004)

The last search that we will consider is the CMS monojet search [142], which is a very different search compared to the previous four, as it targets monojet signatures rather than dijet signatures. It is a general search for excess in events with a highly energetic jet(s) and large missing transverse momentum. This search is not specifically designed for dark showers, but it is expected to be sensitive to the phenomenology of highly invisible dark showers, i.e. with $r_{\text{inv}} \sim 1$.

This analysis utilizes a dataset corresponding to an integrated luminosity of 101 fb^{-1}, collected during 2017–2018 with the CMS detector.

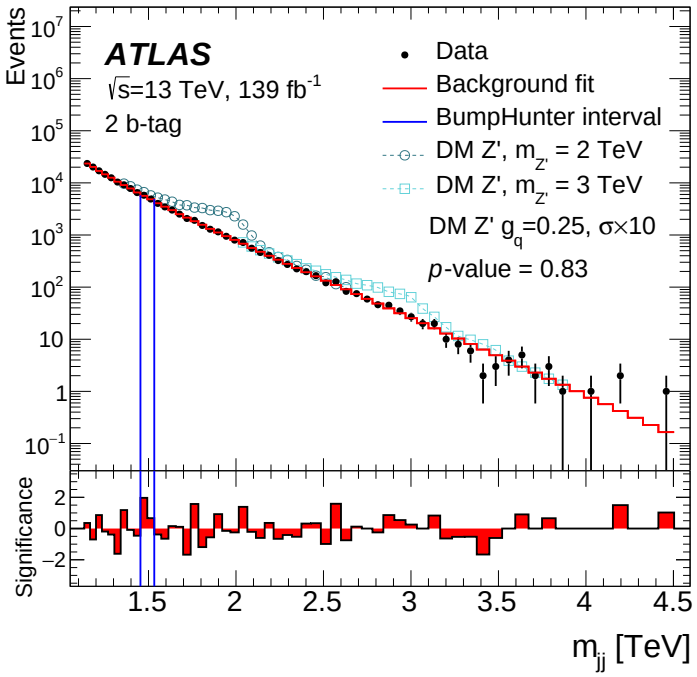

Figure 7.4.: The distributions of m_{jj} for the ATLAS data, simulated SM backgrounds and a Z' signal model with $m_{Z'} = 3.5$ TeV in the ATLAS EXOT-2019-03 search. The distribution is selected from dijet events with both jets b-tagged. The vertical blue lines show the most discrepant interval identified by the BumpHunter test. [139]

The main SM background contributions come from $Z \to \nu\nu$ and $W \to \ell\nu$ processes (where $\ell = e, \mu, \tau$). To constrain these backgrounds, CRs populated with $Z \to \ell\ell$ and $W \to \ell\nu$ events are used, selected via the presence of charged leptons. Additionally, CRs populated with γ+jets events are also defined to support the background estimation. SRs are required to have $p_T^{\text{miss}} > 250$ GeV. Events with $\Delta\phi(\vec{p}_T^{\,\text{jet}}, \vec{p}_T^{\,\text{miss}}) > 0.5$ are rejected to suppress misconstructed jets. This cut is very sensible in this search, where we are looking for monojet events, but excludes exactly the type of events that would be interesting for semi-visible jets. More details on the selection cuts for the different CR and the SR can be found in the original paper [142].

The search variable is $\vec{p}_T^{\,\text{miss}}$. In the signal regions, we expect a large value of p_T^{miss}, as this reflects the momentum carried by the invisible particles. The distributions of the p_T^{miss} in the monojet SR are shown in Figure 7.5. In the control regions, however, the p_T^{miss} is not expected to be large, and instead of using p_T^{miss} in the CR directly, the analysis uses a related quantity called the hadronic recoil. In each event, the hadronic recoil is constructed by summing $\vec{p}_T^{\,\text{miss}}$ with the transverse momentum vectors of the selected charged lepton(s) or photon. This quantity gives an estimate of the momentum carried by the W, Z bosons or the photon in the control regions.

The search sets exclusion limits on the signal strength, which can be translated to the effective production cross section for individual signals. For each signal hypothesis, a fit is performed that includes both signal and background contributions, alongside a separate background-only fit. During the signal fits, nuisance parameters are adjusted for the individual signals. As a result, even if the background-only fit describes the data well, different signal models may still yield nonzero best-fit signal strengths.

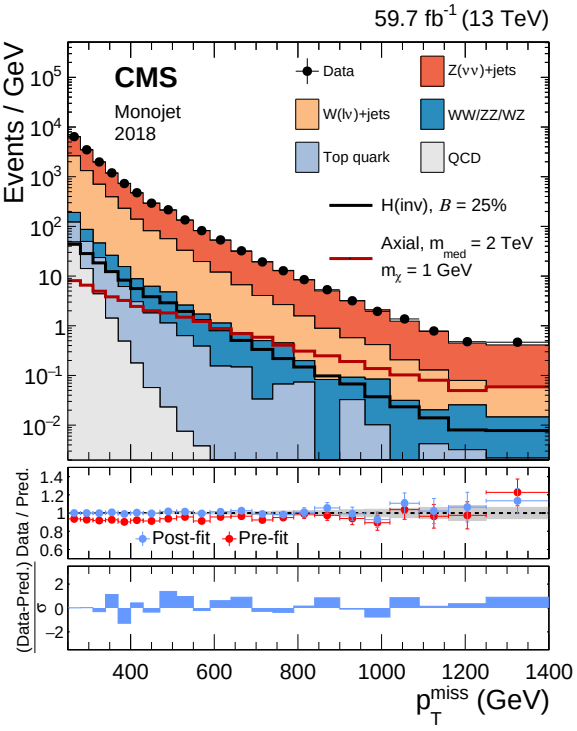

Figure 7.5.: The distributions of p_T^{miss} in the monojet signal region for the 2018 data, simulated SM backgrounds and an example of two signal hypotheses considered in the original analysis, for the CMS PAS-EXO-20-004 search. The fit includes all CRs and the SR and uses data from both 2017 and 2018. [142]

7.2. Complementarity of the searches

While r_{inv} is not a fundamental parameter of the dark sector, it is a phenomenological parameter that is very useful to describe the expected signatures of the dark shower. We can adopt a phenomenological parametrization, in which we take r_{inv} as a free parameter that can be varied independently. With this, we can compare the different searches and see how they complement each other.

This is the goal of a research project conducted in collaboration with with Benjamin Fuks, Marie-Hélène Genest, Mark Goodsell, Felix Kahlhoefer, Sukanya Sinha, Thomas Wojtkowski and myself, which is currently in progress and not yet ready for publication. Here we will briefly discuss our expectations for the different searches.

- Looking at very large values of r_{inv}, close to 1, we expect the CMS monojet search, or other conventional monojet searches, to be most sensitive, as the dark shower is not visible and the ISR monojet signature is most prominent.
- For very small values of r_{inv}, close to 0, we expect the ATLAS dark jets search to perform well. Preliminary results show stronger exclusion powers for $r_{\text{inv}} \in (0.1, 0.3)$ and mediator masses > 1 TeV.
- For intermediate values of r_{inv}, we expect both the ATLAS t-channel semi-visible jets search and the CMS s-channel semi-visible jets search to be sensitive. The ATLAS search is expected to be more sensitive for $r_{\text{inv}} \in (0.5, 0.7)$ and lower mediator masses $\sim 1 - 2$ TeV, while the CMS search is expected to be more sensitive for $r_{\text{inv}} \in (0.1, 0.5)$ and mediator masses $\sim 2 - 5$ TeV. Thus, these two searched are expected to be very complementary in the context of semi-visible jets.

7.3. Recasting the CMS EXO-19-020 analysis in MadAnalysis 5

7.3.1. Implementation

The code in MadAnalysis 5 implements the first four preselection cuts and the last final selection cut listed in Table 7.2, but does not implement the following cuts; $N_e = 0$, $N_\mu = 0$, p_T^{miss} filters, $\Delta R(j_{1,2}, c_{\text{nonfunctional}}) > 0.1$, $f_\gamma(j_1) > 0.7$ & $p_T(j_1) > 1.0$ TeV, and $-3.05 < \eta_j < -1.35$ & $-1.62 < \phi_j < -0.82$. The reasons for this are as follows:

- The $N_e = 0$ and $N_\mu = 0$ cuts are not implemented because these cuts pertain to vetoing any event that contains isolated leptons that pass some kinematic criteria (see *Section 5* of [129] for more details) in order to reduce the backgrounds from $t\bar{t}$ and W($\rightarrow l\nu$)+jets. During the detector simulation stage of this recast, the event information passes through a Delphes built-in electron and muon isolation filter. Although this may not correspond one-to-one with the kinematic and isolation criteria described in [129], the difference of the final results is expected to be insignificant. This expectation is validated in subsection 7.3.3.
- The p_T^{miss} filters are not implemented because they are not relevant for the simulated data, as they are designed to reduce anomalous events due to a variety of reconstruction or detector malfunctions.
- The $\Delta R(j_{1,2}, c_{\text{nonfunctional}}) > 0.1$ cut is not implemented because it requires passing additional information (the narrow jet objects) from Delphes to MA5, which is possible but was deemed unnecessary for this recast due to the very small efficiency of the cut.
- The $f_\gamma(j_1) > 0.7$ & $p_T(j_1) > 1.0$ TeV cut is not implemented because it is expected to have a negligible effect on the efficiency of the analysis, as confirmed by CMS own efficiency studies.
- The $-3.05 < \eta_j < -1.35$ & $-1.62 < \phi_j < -0.82$ cut is not implemented because it is only applied to parts of the data, and CMS has not provided the efficiency of this cut.

MA5 code

Following the guide in [131], we implemented the CMS EXO-19-020 analysis in MadAnalysis 5 as a C++ code that will be integrated with the MA5 analysis dataverse [143], available for public use.

We declare the 2 signal regions, `low-RT SR` and `high-RT SR`, which are defined by $0.15 > R_T \leq 0.25$ and $R_T > 0.25$, respectively. Then we add our cuts. The code for this looks as follows:

```
// =====Declare the signal regions in this analysis=====//
Manager()->AddRegionSelection("low-RT SR");
Manager()->AddRegionSelection("high-RT SR");

//==============Preselection Requirements=================//
Manager()->AddCut("nJets >= 2");
Manager()->AddCut("Leading/subleading jet pT > 200 GeV & eta < 2.4");
Manager()->AddCut("R_T > 0.15");
Manager()->AddCut("dEta(J1, J2) < 1.5");
Manager()->AddCut("m_T > 1.5 TeV");

//============Final Selection Requirements==============//
Manager()->AddCut("dPhi_min <0.8");
```

Following this, we declare our histograms of interest, which in particular is the dijet transverse mass, m_T. Then we define the variables that we want to use in our analysis, and fill the histograms. To end, we apply all cuts in the order of Table 7.2, as this will automatically give us a cutflow table with the cumulative efficiency. For illustrative purposes, we will show the snippet of code that defines the leading jets, which is the first step in the analysis. Note that we pass the reconstructed jet with radius $R = 0.8$ directly from DELPHES to MA5.

```
//======Define reconstructed jets======//
vector<const RecJetFormat*> SignalJets;
for(unsigned int ij=0; ij<event.rec()->jets().size(); ij++)
{
    const RecJetFormat* CurrentJet = &(event.rec()->jets()[ij]);
    SignalJets.push_back(CurrentJet);
}
int  NumSignalJets = SignalJets.size() ;

//=====2 Jets at least cut applied to ALL events====//
if(!Manager()->ApplyCut((NumSignalJets >= 2),"nJets >= 2"))  return true;

//=Leading/subleading jet pT and pseudorapidity cut applied to ALL events=//
SORTER->sort(SignalJets, PTordering); // Ordering jet according to their PT
if (!Manager()->ApplyCut(( SignalJets[0]->pt() > 200
    && SignalJets[1]->pt() > 200 && abs(SignalJets[0]->eta()) < 2.4
    && abs(SignalJets[1]->eta()) < 2.4),
    "Leading/subleading jet pT > 200 GeV & eta < 2.4")) return true;
```

We also provide below here the code that fills the dijet transverse mass histograms and apply the R_T cut that defines the two different signal regions. At this point, all other selection cuts have already been applied. Note that the default energy unit in PYTHIA, DELPHES and MADANALYSIS 5 is GeV, but for the CMS analysis we work with TeV, thus we convert to TeV before filling the histograms.

```
//=======Fill mT histrograms in 2 SR and apply cuts for cutflow======//
if (RT <= 0.25) Manager()->FillHisto("mT low-RT SR",mT/1000);
if (RT > 0.25) Manager()->FillHisto("mT high-RT SR",mT/1000);
if (!Manager()->ApplyCut((RT <= 0.25),"RT <= 0.25")) return true;
if (!Manager()->ApplyCut((RT > 0.25),"RT > 0.25")) return true;
```

7.3.2. Statistical Procedure

The data is described by a product of Poisson probabilities, so the probability of observing n events for a model with parameters $\vec{x}$ is given by the Poisson distribution

$$f_P(n;\vec{x}) = \prod_{i=1}^{N} \frac{u_i(\vec{x})^{n_i}}{n_i!} e^{-u_i(\vec{x})}, \tag{7.6}$$

where we count over N bins, and $u_i(\vec{x})$ is the expected number of events in bin i, and n_i is the number of observed events in bin i, which is a combination of both signal and background events, $n_i = n_i^{\text{sig}} + n_i^{\text{bkg}}$. Similarly, our parameters depend on the both signal model and the background, $\vec{x} = \vec{x}_{\text{sig}}, \vec{x}_{\text{bkg}}$. In this statistical procedure, we are interested in finding the

parameter choices, $\vec{x}$, that gives us the biggest probability of observing n events, i.e. we want to maximize our likelihood function: $L(\vec{x}) = f_P(n; \vec{x})$.

Due to the dependence of the parameters on both the signal and background, we cannot simply maximize the likelihood function with respect to $\vec{x}$, as this could lead to a bias in the exclusion limits, possibly preferring unusually low background yields compensated by high signal yields. Instead, we need to test how each paramater point of the signal model performs against the background-only hypothesis. To do this, we assume some background parameters, so that our likelihood function is now only dependent on the signal. This can be done by choosing the background parameters to be the set that maximizes the likelihood function for the background-only hypothesis, i.e. setting $\mu = 0$, and we get $L_{\hat{x}_{\text{bkg}}}(\mu)$. We may also choose to make the best-fit background a function of μ by repeating the fit of the background parameters for every value of μ, which is called the profile likelihood method. In this case, we would write $L_{\vec{x}_{\text{bkg}}(\mu)}(\mu)$, where $\vec{x}_{\text{bkg}}(\mu)$ is the set of background parameters that maximizes the likelihood function for μ. We implement both methods and confirm our expectations that the profile likelihood method gives slightly weaker bounds on μ than the one where we fit the background parameters to $\mu = 0$.

The maximization of the likelihood function corresponds to minimizing the negative log likelihood function [10], which we define as

$$l_{\hat{x}_b}(\mu) = 2 \sum_i \left[n_{bkg,i} + n_{sig,i} - n_{obs,i} + n_{obs,i} \cdot \log(\frac{n_{obs,i}}{n_{bkg,i} + n_{sig,i}}) \right], \tag{7.7}$$

where the term $n_{obs,i}\log(\frac{n_{obs,i}}{n_{bkg,i}+n_{sig,i}})$ is 0 if $n_{obs,i} = 0$. We then define the test statistic as

$$\text{TS}(\mu) = l_{\vec{x}_b}(\mu) - l_{\vec{x}_b}(0) - 3.84. \tag{7.8}$$

When the test statistic is positive, $l_{\vec{x}_b}(\mu)$ is larger than $l_{\vec{x}_b}(0) + 3.84$, i.e. it is less likely that we are observing the signal hypothesis than the background-only hypothesis. The value of 3.84 corresponds to the 95% confidence level upper bound on the signal strength μ. We therefore exclude the signal strength μ if $\text{TS}(\mu) > 0$ with 95% confidence.

7.3.3. Validation

We validate our implementation of the CMS EXO-19-020 analysis by comparing the cut-flow tables and exclusion limits obtained from our recast with those of the original CMS search. We produce 50.000 simulated events with Pythia 8 and Delphes for three different values of the Z' mass, $m_{Z'} = 2.1, 3.1, 4.1$ TeV, using the same cards as the original CMS search. We then feed the Delphes output through our analysis code in MadAnalysis 5 and obtain the cut-flow tables and exclusion limits. The cut-flow tables are shown in Table 7.7, where we compare our results with those of the original CMS search.

We see a remarkably close agreement of our results with the CMS analysis, in particular for the lowest Z' mass point, $m_{Z'} = 2.1$ TeV, where the differences in the cut-flow efficiencies are all within 1% and the final efficiency agrees to at least one decimal. For the two higher mass points, the differences are slightly larger, but still within 2%. For these two mass points, the small discrepancies in the final $\Delta\phi_{\text{min}}$ cut efficiency is larger than that of the second-last $m_T > 1.5$ TeV cut, which may be due to the fact that we have not implemented all cuts in the MA5 analysis, as discussed in subsection 7.3.1. However, this shows that the efficiency of the cuts that we did not implement is very small, and thus the final efficiency is not significantly affected by omitting these cuts.

In Figure 7.6, we show how the m_T distribution of our simulated events and MA5 analysis compares to the original CMS results. We also show our best-fit function to the experimental data, having used the statistical procedure described in subsection 7.3.2 to obtain the best-fit parameters. We see that our results are in good agreement with the original CMS results.

Table 7.7.: Cumulative cut-flow efficiency from CMS compared to the MA5 analysis results across three different $m_{Z'}$ points. Efficiency is given in percentages [%]. A dash under CMS results indicates that the cut-flow efficiency was not published, and a dash under the MA5 results indicates that the cut was not implemented in the MA5 analysis.

	$m_{Z'} = 2.1$ TeV		$m_{Z'} = 3.1$ TeV		$m_{Z'} = 4.1$ TeV	
Selection cut	**CMS**	**MA5**	**CMS**	**MA5**	**CMS**	**MA5**
$N_{\text{jets}} > 1$	—	99.7	—	99.9	—	99.9
$p_T(J1,2) > 200$ GeV & $\eta(J1,2) < 2.4$	70.4	70.8	83.5	84.4	89.9	90.3
$R_T > 0.15$	26.1	25.8	33.1	32.9	36.1	35.8
$\Delta\eta(J1,J2) < 1.5$	22.2	21.8	26.5	26.3	27.8	27.4
$m_T > 1.5$ TeV	10.5	9.7	21.7	21.0	24.5	24.9
$N_\mu = 0$	10.2	—	21.0	—	24.3	—
$N_e = 0$	10.2	—	20.9	—	24.2	—
p_T^{miss} filters	10.2	—	20.8	—	24.4	—
$\Delta R(j_{1,2}, c_{\text{nonfunctional}}) > 0.1$	9.7	—	19.8	—	23.1	—
veto $f_\gamma(j_1) > 0.7$ & $p_T(j_1) > 1.0$ TeV	9.7	—	19.8	—	23.0	—
veto $-3.05 < \eta_j < -1.35$ & $-1.62 < \phi_j < -0.82$	—	—	—	—	—	—
$\Delta\phi_{\text{min}} < 0.8$	8.8	8.8	17.0	18.5	19.8	21.5

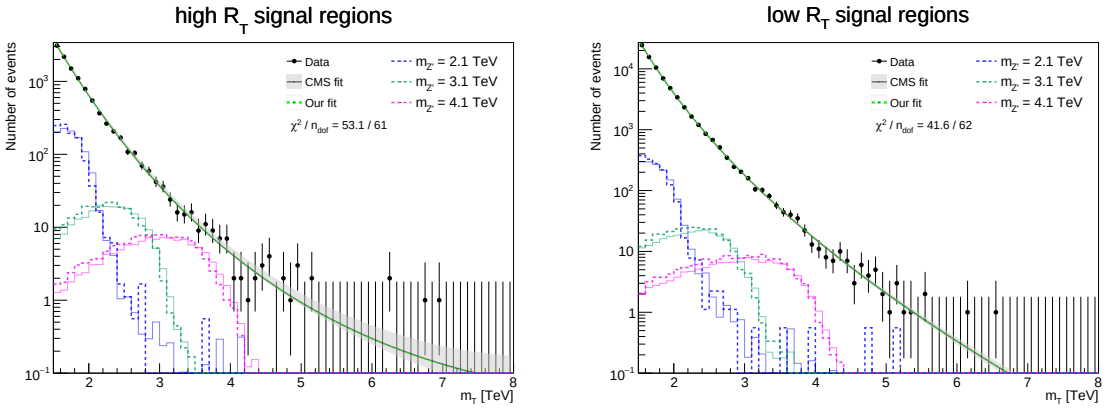

Figure 7.6.: The m_T distribution of our simulated events and MA5 analysis compared to the original CMS results for the three different $m_{Z'}$ mass points. The solid lines are from the CMS analysis [129], and the dashed lines are the results of this work. The left plot shows the high R_T signal region, while the right plot shows the low R_T signal region. The solid grey line and shaded area represents the CMS best-fit function and the uncertainty band. The dashed green line is our best-fit function to the experimental data, and the χ^2 value of the fit is also shown.

CHAPTER 8

Final Conclusion and Outlook

One of the most central questions in particle physics today is the nature of dark matter. While there is overwhelming evidence for its existence from astrophysical and cosmological observations, its nature remains elusive. The lack of conclusive signals in direct and indirect detection experiments, as well as in collider searches, has motivated the exploration of a wide range of theoretical models beyond the traditional weakly interacting massive particle (WIMP) paradigm. We explored these motivations, as well as some of the popular dark matter candidates in Chapter 3. A particularly interesting avenue of this research is that of strongly interacting dark matter (SIMP), which can simultaneously address the dark matter relic abundance and yield novel signatures at collider and accelerator experiments. In Chapter 4, we discussed the theoretical framework for strongly interacting dark sectors, as well as the phenomenology of dark showers at colliders.

In this thesis, we have worked with two opposing approaches to the study of strongly interacting dark sectors. On one hand, we have studied a very specific model of a strongly interacting dark sector, with a well-defined structure and range of parameters. This has allowed us to explore the theoretical aspects of the model in detail, and project the phenomenology onto a range of experimental searches, both current and future. On the other hand, we have also considered the broader context of experimental searches for dark showers at the LHC, which aim to be sensitive to a wide range of models and signatures. This has highlighted the challenges and opportunities in interpreting experimental results in the context of strongly interacting dark sectors, and the need for systematic studies of the impact of model assumptions on the derived limits.

Chapter 4 introduces our theoretical treatment of a strongly interacting dark sector, assuming an $SU(N_{c_D})$ structure with confinement at lower energies. This is directly applicable to our in-depth studies of the model in Chapter 5 and Chapter 6. A key aspect of our approach is the use of effective field theory (EFT) techniques to describe the low-energy dynamics of the dark sector. We employed chiral perturbation theory (ChPT) to model the interactions of the pseudo-scalar dark mesons, and extended this framework to include vector mesons that have a mass lighter than twice that of the pseudo-scalar mesons. This allowed us to capture the essential features of the dark sector dynamics, and make precise calculations of relevant processes.

In Chapter 5, we studied the implications of the model for the dark matter relic abundance through a freeze-out process in the early Universe. We found that the presence of light vector mesons leads to a viable freeze-out mechanism in theories with two dark flavors (or more), which is a scenario that is particularly well-motivated from a theoretical perspective. That is because for even N_{f_D}, we have a mechanism of stabilizing all the dark pions through a dark G-parity, which is not possible for odd N_{f_D}. In fact, even if the dark sector has more than two flavors, we may approximate the dynamics with an effective two-flavor theory, under the assumption that the other flavors are significantly heavier. This is in contrast to the traditional SIMP scenario, which requires at least three flavors to allow a number-changing process, namely the $3\pi_D \to 2\pi_D$ process, that is responsible for achieving the dark pion relic abundance. The inclusion of light vector mesons opens up a new annihilation channel $3\pi_D \to \pi_D \rho_D$ and keeps the dark sector in thermal equilibrium with the SM through (inverse) decays of $\rho_D \to$ SM. The self-interactions of the dark pions, which are constrained by astrophysical observations, are also reduced in this scenario, making it consistent with current bounds.

We explored the parameter space of the model, identifying regions that yield the correct relic abundance while satisfying the astrophysical constraints from the Bullet Cluster constraints. For instance, we found that for a model with $N_{f_D} = 2$, $N_{c_D} = 3$, a dark pion mass of $m_{\pi_D} \sim 230 - 300$ MeV, and dark rho mass $m_{\rho_D} \sim 345 - 570$ MeV, yields the correct relic abundance while evading even the more stringent constraints from the Bullet Cluster.

We continued the study of this type of strongly interacting dark sector in Chapter 6, where we investigated the phenomenology of the model at accelerator experiments. For this, we restricted ourselves to the case of two dark flavors. Crucially, we specified a vector portal coupling between the dark sector and the SM that gave rise to kinetic mixing between the dark vector mesons and the SM fermions. This coupling is analogous to the dark photon model, and allows the dark mesons to be produced through various mechanisms in high-energy collisions of SM particles. While heavy vector mesons may also decay into SM particles, we focused on the light vector meson case, which ensures exclusive decays into SM particles, and results in longer lifetimes that yield displaced vertices, making it a very exciting candidate for experimental searches.

An ideal setting for probing this model is through fixed-target experiments, that include a decay volume is placed downstream to detect the decay products of long-lived particles. A similar model was studied in Ref. [86] in the context of b-factory experiments such as Belle II and LHCb. We extended this work by considering the current and near-future SPS-based beam dump experiments, NA62 and SHiP. We found that these experiments are particularly sensitive to the parameter space of the model that yields the correct relic abundance, and can probe regions that are not accessible to other experiments. The projections are very sensitive to the suppression scale, or the kinetic mixing parameter, as this dictates the lifetime of the vector mesons and the production cross sections. NA62 can already place constraints on the model, despite not being finished with data taking yet. NA62 is expected to finish data taking in the next few years, but the projected sensitivity of the full data is only slightly better than the current constraints. In contrast, SHiP, which is expected to start data taking in the early 2030s, will be able to probe much further into the parameter space, going to both smaller and larger values of the suppression scale, as well as much larger masses of the vector mesons. The projected sensitivity of SHiP extends well into the region that yields the correct relic abundance, making it a very promising experiment for probing this type of strongly interacting dark sector.

A notable feature of the vector meson, which couples to Standard Model fermions via kinetic mixing through a massive vector portal, is that its production mechanisms closely resemble those of dark photons. This means that existing constraints on dark photons can

be reinterpreted in the context of our model, providing additional bounds on the parameter space. However, the dark vector meson differentiates itself from the dark photon in that it can be produced through dark showers, leading to larger production cross sections in certain regimes and multi-decay signatures. We project that SHiP will be sensitive to di-decay and tri-decay, albeit with a limited reach in parameter space. Future experiments with larger decay volumes and higher luminosities could potentially probe even higher multiplicities of decays, offering enhanced discovery potential of this type of strongly interacting dark sectors.

The results of Chapter 6 rely on the simulations dark shower dynamics, for which we used the Monte Carlo machine Pythia. The uncertainties associated with these simulations are not well understood, and represent an important avenue for future work. The showering and hadonization algorithms in Pythia are based on the Lund string model, which is tuned to reproduce the properties of QCD jets. However, it is not clear how well these algorithms perform in the context of a strongly interacting dark sector, where the dynamics may be different from QCD. The Lund string model is, importantly, not the only model for hadronization, and other models, such as the cluster model, may yield different results. The Herwig event generator uses the cluster model for hadronization, and it would be interesting to compare the results obtained using Pythia with those obtained using Herwig. We have only used Pythia in this work, as it is currently the only event generator that can implement a strongly interacting dark sector. However, future developments in Herwig are expected to include this capability, and it would be very interesting to compare the results obtained using the two different showering algorithms. This would provide a better understanding of the uncertainties associated with the simulations, and help to assess the robustness of the results.

In Chapter 7, we change the methodology and consider strongly interacting dark sectors in the broader context of experimental searches for dark showers at the LHC. In these studies, the aim is often to remain model-independent and be sensitive to a wide range of models and signatures. These searches typically rely on simplified models that neglect many details of the dark sector, enabling them to capture the phenomenology of a wide class of scenarios. However, when generating signal predictions through simulation tools, we must specify numerous details of the dark sector, which introduces model-dependent assumptions. The impact of these assumptions on phenomenology and, crucially, on the exclusion limits derived from experiments, remains poorly understood. Addressing this gap is essential for assessing the robustness of current experimental constraints.

A systematic study of how dark sector details influence observable signatures is therefore needed. This highlights the importance of reinterpretation efforts for LHC searches. Furthermore, many of these searches were conducted before the community had developed a coherent framework for constructing strongly interacting dark sector models. Consequently, reinterpretation involves more than simply varying model parameters; it may require modifying parameter relations or even adopting alternative model structures that better align with theoretical expectations. This further emphasizes the need for comprehensive reinterpretation studies to ensure that experimental results are accurately contextualized within the evolving landscape of strongly interacting dark sector theories.

Large collaborative efforts went into formulating a consistent model building framework, comprehensively summarized in Ref. [3]. Efforts to increase and align collaboration between theorists and experimentalists are ongoing, see for example the LHC Reinterpretation forum [132]. This work, as presented in Chapter 7, represents a small step in this direction. We reviewed five LHC searches with discovery potential for dark showers; two searches for semi-visible jets [129, 134], two searches for dark jets [137, 139] and one for invisible dark showers via mono-jet signatures [142]. Not included is searches for emerging jets, but we encapsulate a similar type of phenomenology in Chapter 6 through displaced decay vertex searches.

We focused on the dedicated CMS search for semi-visible jets [129] in this work. We demonstrated how we can recast the results to a specific model of a strongly interacting dark sector using the MadAnalysis 5 framework. The other four searches have also been recast in MadAnalysis 5 by collaborators of this project [144,145] or by the original experimental collaboration [146], and all five searches will be publicly available in the MadAnalysis 5 database in the near future. This allows anyone to easily recast these searches to their own model of interest, and to explore the impact of different model assumptions on the derived limits. Current work is ongoing to perform this exact kind of systematic study. The dark sector models will follow the framework outlined in Ref. [3], and will vary the number of dark colors and flavors as well as the average ratio of stable dark mesons, r_{inv}. The results will provide a better understanding of the robustness of current experimental constraints, and help to guide future searches for strongly interacting dark sectors at the LHC.

Beyond accelerator experiments, there may exist other avenues for probing strongly interacting dark sectors. One of these that are very different from other methods discussed in this thesis is through gravitational wave (GW) observations. If the dark sector undergoes a first-order phase transition in the early Universe, it can produce a stochastic background of GWs that may be detectable by current or future GW observatories [147,148]. The characteristics of the GW signal depend on the details of the phase transition, which in turn depend on the properties of the dark sector. This provides a unique opportunity to probe strongly interacting dark sectors through GW observations, complementing traditional accelerator searches. Future work could explore the implications of our specific model for GW signals, and assess the prospects for detection with current and future GW observatories.

In conclusion, this thesis has explored a specific corner of the vast theoretical landscape of strongly interacting dark sectors, highlighting both the challenges and opportunities in understanding their phenomenology and experimental signatures. While significant progress has been made in recent years in probing these models, the true nature of dark matter remains one of the most profound mysteries in modern physics. As experiments continue to reach further and theoretical frameworks evolve, the search for dark matter will undoubtedly lead to new insights, and hopefully discoveries, in the years to come.

APPENDIX A

Expanding the Dark Chiral Lagrangian

The Dark Chiral Lagrangian is

$$\mathcal{L}_{\mathrm{Ch_{Dark}}} = \frac{f_{\pi_D}^2}{4}\mathrm{Tr}\left(D\mu U D^\mu U^\dagger\right) + \left[\frac{\mu_D^3}{2}\mathrm{Tr}\left(M_{q_D}U^\dagger\right) + \mathrm{h.c.}\right], \tag{A.1}$$

U and $U^\dagger$ can be Taylor expanded to

$$U \simeq 1 + 2i\frac{\pi_D}{f_{\pi_D}} + \frac{1}{2}(2i\tfrac{\pi_D}{f_{\pi_D}})^2 + \tfrac{1}{6}(2i\tfrac{\pi_D}{f_{\pi_D}})^3 \tag{A.2}$$

$$U^\dagger \simeq 1 - 2i\tfrac{\pi_D}{f_{\pi_D}} + \tfrac{1}{2}(2i\tfrac{\pi_D}{f_{\pi_D}})^2 - \tfrac{1}{6}(2i\tfrac{\pi_D}{f_{\pi_D}})^3 \tag{A.3}$$

The first term is expanded to 3rd order:

$$\mathcal{L}_{\mathrm{Ch}} \supset \tfrac{f_{\pi_D}^2}{4}\mathrm{Tr}\Big(D_\mu(1+2i\tfrac{\pi_D}{f_{\pi_D}}+\tfrac{1}{2}(2i\tfrac{\pi_D}{f_{\pi_D}})^2+\tfrac{1}{6}(2i\tfrac{\pi_D}{f_{\pi_D}})^3)D^\mu(1-2i\tfrac{\pi_D}{f_{\pi_D}}+\tfrac{1}{2}(2i\tfrac{\pi_D}{f_{\pi_D}})^2-\tfrac{1}{6}(2i\tfrac{\pi_D}{f_{\pi_D}})^3)\Big) \tag{A.4}$$

We drag D_μ and D^μ into the parentheses:

$$\begin{aligned}\mathcal{L}_{\mathrm{Ch}} \supset \tfrac{f_{\pi_D}^2}{4}\mathrm{Tr}\Big((D_\mu 1 + D_\mu 2i\tfrac{\pi_D}{f_{\pi_D}} + D_\mu\tfrac{1}{2}(2i\tfrac{\pi_D}{f_{\pi_D}})^2 + D_\mu\tfrac{1}{6}(2i\tfrac{\pi_D}{f_{\pi_D}})^3)\times \\ (D^\mu 1 - D^\mu 2i\tfrac{\pi_D}{f_{\pi_D}} + D^\mu\tfrac{1}{2}(2i\tfrac{\pi_D}{f_{\pi_D}})^2 - D^\mu\tfrac{1}{6}(2i\tfrac{\pi_D}{f_{\pi_D}})^3)\Big)\end{aligned} \tag{A.5}$$

We use that $D_\mu 1 = 0$ and pull out the common factor of $\frac{2i}{f_{\pi_D}}$ from each of the parentheses:

$$\mathcal{L}_{\mathrm{Ch}} \supset \tfrac{f_{\pi_D}^2}{4}\left(\tfrac{2i}{f_{\pi_D}}\right)^2\mathrm{Tr}\Big((D_\mu\pi_D+\tfrac{i}{f_{\pi_D}}D_\mu{\pi_D}^2+\tfrac{2i^2}{3f_{\pi_D}^2}D_\mu{\pi_D}^3)(-D^\mu\pi_D+\tfrac{i}{f_{\pi_D}}D^\mu{\pi_D}^2-\tfrac{2i^2}{3f_{\pi_D}^2}D^\mu{\pi_D}^3)\Big) \tag{A.6}$$

The factors in front cancel aside from $i^2 = -1$. We then multiply out the parentheses on the line after:

$$\begin{aligned}\mathcal{L}_{\text{Ch}} \supset & -\operatorname{Tr}\Big((D_\mu\pi_D + \tfrac{i}{f_{\pi_D}} D_\mu\pi_D{}^2 - \tfrac{2}{3f_{\pi_D}^2} D_\mu\pi_D{}^3)(- D^\mu\pi_D + \tfrac{i}{f_{\pi_D}} D^\mu\pi_D{}^2 + \tfrac{2}{3f_{\pi_D}^2} D^\mu\pi_D{}^3)\Big) \\ = & -\operatorname{Tr}\Big(- D_\mu\pi_D D^\mu\pi_D + \tfrac{i}{f_{\pi_D}} D_\mu\pi_D D^\mu\pi_D{}^2 + \tfrac{2}{3f_{\pi_D}^2} D_\mu\pi_D D^\mu\pi_D{}^3 \\ & - \tfrac{i}{f_{\pi_D}} D_\mu\pi_D{}^2 D^\mu\pi_D + \tfrac{i^2}{f_{\pi_D}^2} D_\mu\pi_D{}^2 D^\mu\pi_D{}^2 + \tfrac{2i}{3f_{\pi_D}^3} D_\mu\pi_D{}^2 D^\mu\pi_D{}^3 \\ & + \tfrac{2}{3f_{\pi_D}} D_\mu\pi_D{}^3 D^\mu\pi_D - \tfrac{2i}{3f_{\pi_D}^3} D_\mu\pi_D{}^3 D^\mu\pi_D{}^2 - \tfrac{4}{9f_{\pi_D}^4} D_\mu\pi_D{}^3 D^\mu\pi_D{}^3\Big) \end{aligned} \tag{A.7}$$

We change the signs on both sides of the parentheses and separate any terms with higher than 4 π_D fields:

$$\begin{aligned}\mathcal{L}_{\text{Ch}} \supset & \operatorname{Tr}\Big(D_\mu\pi_D D^\mu\pi_D - \tfrac{i}{f_{\pi_D}} (D_\mu\pi_D D^\mu\pi_D{}^2 - D_\mu\pi_D{}^2 D^\mu\pi_D) \\ & - \tfrac{2}{3f_{\pi_D}^2} (D_\mu\pi_D D^\mu\pi_D{}^3 + D_\mu\pi_D{}^3 D^\mu\pi_D) - \tfrac{i^2}{f_{\pi_D}^2} D_\mu\pi_D{}^2 D^\mu\pi_D{}^2\Big) \\ & + \mathcal{O}(\pi_D{}^5) + \mathcal{O}(\pi_D{}^6) \end{aligned} \tag{A.8}$$

We take the trace of each term individually as the trace is a linear operation:

$$\begin{aligned}\mathcal{L}_{\text{Ch}} \supset & \operatorname{Tr}(D_\mu\pi_D D^\mu\pi_D) - \tfrac{i}{f_{\pi_D}} \operatorname{Tr}(D_\mu\pi_D D^\mu\pi_D{}^2 - D_\mu\pi_D{}^2 D^\mu\pi_D) \\ & - \tfrac{2}{3f_{\pi_D}^2} \operatorname{Tr}(D_\mu\pi_D D^\mu\pi_D{}^3 + D_\mu\pi_D{}^3 D^\mu\pi_D) + \tfrac{1}{f_{\pi_D}^2} \operatorname{Tr}(D_\mu\pi_D{}^2 D^\mu\pi_D{}^2) + \text{h.o.} \end{aligned} \tag{A.9}$$

We see that the first term is present in the form we see in the final Lagrangian in Eq. 4.4. The second term, with $\mathcal{O}(\pi_D{}^4)$ is zero, because we can use the cyclic property of the trace to show that the two terms in the parentheses are equal and therefore cancel once renaming the upper/lower Lorentz indices.

We take a closer look at the last two terms:

$$\begin{aligned} & -\tfrac{2}{3f_{\pi_D}^2} \operatorname{Tr}(D_\mu\pi_D D^\mu\pi_D{}^3 + D_\mu\pi_D{}^3 D^\mu\pi_D) + \tfrac{1}{f_{\pi_D}^2} \operatorname{Tr}(D_\mu\pi_D{}^2 D^\mu\pi_D{}^2) \\ & = -\tfrac{2}{3f_{\pi_D}^2} \operatorname{Tr}(D_\mu\pi_D D^\mu\pi_D\pi_D{}^2 + D_\mu\pi_D\pi_D D^\mu\pi_D\pi_D + D_\mu\pi_D\pi_D{}^2 D^\mu\pi_D \\ & \quad + D_\mu\pi_D\pi_D{}^2 D^\mu\pi_D + \pi_D D_\mu\pi_D\pi_D D^\mu\pi_D + D_\mu\pi_D\pi_D{}^2 D^\mu\pi_D) \\ & \quad + \tfrac{1}{f_{\pi_D}^2} \operatorname{Tr}((D_\mu\pi_D\pi_D + \pi_D D_\mu\pi_D)(\pi_D D^\mu\pi_D + D^\mu\pi_D\pi_D)) \end{aligned} \tag{A.10}$$

We collect the 2 terms that are equal in the first trace and multiply the parentheses in the second trace:

$$\begin{aligned} = & -\tfrac{2}{3f_{\pi_D}^2} \operatorname{Tr}(D_\mu\pi_D D^\mu\pi_D\pi_D{}^2 + D_\mu\pi_D\pi_D D^\mu\pi_D\pi_D \\ & \qquad + 2D_\mu\pi_D\pi_D{}^2 D^\mu\pi_D + D_\mu\pi_D\pi_D{}^2 D^\mu\pi_D + \pi_D D_\mu\pi_D\pi_D D^\mu\pi_D) \\ & + \tfrac{1}{f_{\pi_D}^2} \operatorname{Tr}(D_\mu\pi_D\pi_D\pi_D D^\mu\pi_D + \pi_D D_\mu\pi_D\pi_D D^\mu\pi_D + D_\mu\pi_D\pi_D D^\mu\pi_D\pi_D + \pi_D D_\mu\pi_D D^\mu\pi_D\pi_D) \end{aligned} \tag{A.11}$$

$$\begin{aligned} = & -\tfrac{2}{3f_{\pi_D}^2} \operatorname{Tr}(\pi_D{}^2 D_\mu\pi_D D^\mu\pi_D + \pi_D D_\mu\pi_D\pi_D D^\mu\pi_D \\ & \qquad + 2\pi_D{}^2 D^\mu\pi_D D_\mu\pi_D + \pi_D{}^2 D^\mu\pi_D D_\mu\pi_D + \pi_D D^\mu\pi_D\pi_D D_\mu\pi_D) \\ & + \tfrac{1}{f_{\pi_D}^2} \operatorname{Tr}(\pi_D{}^2 D^\mu\pi_D D_\mu\pi_D + \pi_D D^\mu\pi_D\pi_D D_\mu\pi_D + \pi_D D^\mu\pi_D\pi_D D_\mu\pi_D + \pi_D{}^2 D_\mu\pi_D D^\mu\pi_D), \end{aligned} \tag{A.12}$$

where we have used the cyclic property of the trace. We now rename the Lorentz indices so that all terms have the same order of Lorentz indices:

$$\begin{aligned}
&= -\tfrac{2}{3f_{\pi_D}^2}\mathrm{Tr}\big({\pi_D}^2 D_\mu \pi_D D^\mu \pi_D + \pi_D D_\mu \pi_D \pi_D D^\mu \pi_D \\
&\qquad + 2{\pi_D}^2 D_\mu \pi_D D^\mu \pi_D + {\pi_D}^2 D_\mu \pi_D D^\mu \pi_D + \pi_D D_\mu \pi_D \pi_D D^\mu \pi_D\big) \\
&\quad + \tfrac{1}{f_{\pi_D}^2}\mathrm{Tr}\big({\pi_D}^2 D_\mu \pi_D D^\mu \pi_D + \pi_D D_\mu \pi_D \pi_D D^\mu \pi_D + \pi_D D_\mu \pi_D \pi_D D^\mu \pi_D + {\pi_D}^2 D_\mu \pi_D D^\mu \pi_D\big)
\end{aligned} \tag{A.13}$$

Now we can collect terms that are equal:

$$\begin{aligned}
&= -\tfrac{2}{3f_{\pi_D}^2}\mathrm{Tr}\big(4{\pi_D}^2 D_\mu \pi_D D^\mu \pi_D + 2\pi_D D_\mu \pi_D \pi_D D^\mu \pi_D\big) \\
&\quad + \tfrac{1}{f_{\pi_D}^2}\mathrm{Tr}\big(2{\pi_D}^2 D_\mu \pi_D D^\mu \pi_D + 2\pi_D D_\mu \pi_D \pi_D D^\mu \pi_D\big) &\text{(A.14)} \\
&= -\tfrac{1}{f_{\pi_D}^2}\mathrm{Tr}\big(\tfrac{8}{3}{\pi_D}^2 D_\mu \pi_D D^\mu \pi_D \\
&\quad + \tfrac{4}{3}\pi_D D_\mu \pi_D \pi_D D^\mu \pi_D - 2{\pi_D}^2 D_\mu \pi_D D^\mu \pi_D - 2\pi_D D_\mu \pi_D \pi_D D^\mu \pi_D\big) &\text{(A.15)} \\
&= -\tfrac{1}{f_{\pi_D}^2}\mathrm{Tr}\big(\tfrac{2}{3}{\pi_D}^2 D_\mu \pi_D D^\mu \pi_D - \tfrac{2}{3}\pi_D D_\mu \pi_D \pi_D D^\mu \pi_D\big) \\
&= -\tfrac{2}{3f_{\pi_D}^2}\mathrm{Tr}\left(\pi_D^2 D_\mu \pi_D D^\mu \pi_D - \pi_D D_\mu \pi_D \pi_D D^\mu \pi_D\right) &\text{(A.16)}
\end{aligned}$$

These are exactly the terms we see in the last trace of the final Lagrangian in Eq. 4.4.

The second term of Equation A.1 does not need to be expanded at the odd orders, as it includes sums of U and $U^\dagger$, and these have opposite signs in the new term of the 3rd order expansion and therefore cancel. However, even orders will not cancel, so we will expand the even terms up to 4th order and skip the odd expansions:

$$\begin{aligned}
\mathcal{L}_{\mathrm{Ch}} \supset & \tfrac{\mu_D^3}{2}\left[\mathrm{Tr}\left(M_{q_D}\left(1 + \tfrac{1}{2}(2i\tfrac{\pi_D}{f_{\pi_D}})^2 + \tfrac{1}{24}(2i\tfrac{\pi_D}{f_{\pi_D}})^4\right)\right) + \mathrm{Tr}\left(M_{q_D}\left(1 + \tfrac{1}{2}(2i\tfrac{\pi_D}{f_{\pi_D}})^2 + \tfrac{1}{24}(2i\tfrac{\pi_D}{f_{\pi_D}})^4\right)\right)\right] \\
= & \mu_D^3\left[\mathrm{Tr}(M_{q_D}) + \mathrm{Tr}\left(M_{q_D}\tfrac{1}{2}(2i\tfrac{\pi_D}{f_{\pi_D}})^2\right) + \mathrm{Tr}\left(M_{q_D}\tfrac{1}{24}(2i\tfrac{\pi_D}{f_{\pi_D}})^4\right)\right] \\
= & \mu_D^3\left[N_{f_D} m_{q_D} - \tfrac{2}{f_{\pi_D}^2}\mathrm{Tr}\left(M_{q_D}{\pi_D}^2\right) + \tfrac{2}{3f_{\pi_D}^4}\mathrm{Tr}\left(M_{q_D}{\pi_D}^4\right)\right]
\end{aligned} \tag{A.17}$$

We may ignore the first term, as there are no dynamical fields in this so it would only present a constant and no dynamic physics. We assume mass-degenerate quarks so our mass matrix M_{q_D} is

$$M_{q_D} = \begin{pmatrix} m_{q_D} & 0 & \dots & 0 \\ 0 & m_{q_D} & & \vdots \\ \vdots & & \ddots & \vdots \\ 0 & \dots & \dots & m_{q_D} \end{pmatrix} \tag{A.18}$$

up to the dimension equal to the number of flavors, N_{f_D}. We write out the terms inside the first trace:

$$\tfrac{2\mu_D^3}{f_{\pi_D}^2}\mathrm{Tr}\left(M_{q_D}{\pi_D}^2\right) = \tfrac{2\mu_D^3}{f_{\pi_D}^2}\sum_{i=0}^{N_{f_D}} m_{q_D}({\pi_D}^2)_{ii} = \tfrac{2\mu_D^3}{f_{\pi_D}^2} m_{q_D}\mathrm{Tr}({\pi_D}^2) \tag{A.19}$$

From the Gell-Mann–Oakes–Renner relation, we know that the square of the pion mass scales linearly with the quark masses, so now we can identify the dark pion mass as

$$m_{\pi_D}^2 = \tfrac{2\mu_D^3}{f_{\pi_D}^2} m_{q_D} \tag{A.20}$$

Going back to the Lagrangian we can write it as

$$\mathcal{L}_{\text{Ch}} \supset - m_{\pi_D}^2 \text{Tr}\left({\pi_D}^2\right) + \frac{m_{\pi_D}^2}{3 f_{\pi_D}^2} \text{Tr}\left({\pi_D}^4\right). \tag{A.21}$$

APPENDIX B

Kinetic mixing between the Z' and the neutral/charged dark rho mesons

The kinetic mixing term between the dark photon Z' and the dark rho mesons ρ_D is given by

$$\mathcal{L}_{\text{dark mix}} = -\frac{e_D}{g_{\pi_D\rho_D}} Z'_{\mu\nu}\text{Tr}(Q_D\rho_D{}^{\mu\nu}), \tag{B.1}$$

where $\rho_D{}^{\mu\nu} = \partial^\mu\rho_D{}^\nu - \partial^\nu\rho_D{}^\mu - ig[\rho_D{}^\mu, \rho_D{}^\nu]$. Under the assumption that $N_{f_D} = 2$ and $Q_D = \text{diag}(1, -1)$, we expand this term to find the mixing between the Z' and the individual dark rho mesons, $\rho_D^0, \rho_D^\pm$. For this, we introduce the dark ρ_D matrix as

$$\rho_D = \tfrac{1}{2}\rho_D^a\sigma^a = \frac{1}{\sqrt{2}}\begin{pmatrix} \frac{\rho_D{}^0}{\sqrt{2}} & \rho_D^+ \\ \rho_D^- & -\frac{\rho_D^0}{\sqrt{2}} \end{pmatrix} \tag{B.2}$$

where σ^a are the Pauli matrices. We can then write the kinetic mixing term as

$$\begin{aligned}\mathcal{L}_{Z'-\rho_D} &= -\frac{e_D}{g_{\pi_D\rho_D}} Z'_{\mu\nu}\text{Tr}(Q_D(\partial^\mu\rho_D^\nu - \partial^\nu\rho_D^\mu - ig_{\pi_D\rho_D}[\rho_D^\mu, \rho_D^\nu])) \\ &= -\frac{e_D}{g_{\pi_D\rho_D}} Z'_{\mu\nu}\left(\partial^\mu\rho_D^{0\nu} - \partial^\nu\rho_D^{0\mu}\right) + ie_D Z'_{\mu\nu}(\rho_D^{+\mu}\rho_D^{-\nu} - \rho_D^{-\mu}\rho_D^{+\nu})\end{aligned} \tag{B.3}$$

The first term is the kinetic mixing between the Z' and the neutral dark rho meson ρ_D^0, while the second term is an interaction term between the Z' and the charged dark rho mesons $\rho_D^\pm$. To see how we arrive at this, we expand the commutator in the second term and perform permutations:

$$ie_D Z'_{\mu\nu}\text{Tr}(Q_D[\rho_D^\mu\rho_D^\nu]) = -e_D Z'_{\mu\nu}\text{Tr}(Q_D\epsilon^{abc}(\rho_D^{a,\mu}\rho_D^{b,\nu} + \rho_D^{b,\mu}, \rho_D^{a,\nu})(\sigma^c)) \tag{B.4}$$

The pauli matrices are

$$\sigma^1 = \begin{pmatrix} 0 & 1 \\ 1 & 0 \end{pmatrix}, \quad \sigma^2 = \begin{pmatrix} 0 & -i \\ i & 0 \end{pmatrix}, \quad \sigma^3 = \begin{pmatrix} 1 & 0 \\ 0 & -1 \end{pmatrix}. \tag{B.5}$$

and we use that

$$\begin{aligned}\epsilon^{abc}\rho_D^{a,\mu}\rho_D^{b,\nu}(\sigma^c) = \rho_D^{1,\mu}\rho_D^{2,\nu}(\sigma^3) + \rho_D^{3,\mu}\rho_D^{1,\nu}(\sigma^2) + \rho_D^{2,\mu}\rho_D^{3,\nu}(\sigma^1) \\ -\rho_D^{2,\mu}\rho_D^{1,\nu}(\sigma^3) - \rho_D^{1,\mu}\rho_D^{3,\nu}(\sigma^2) - \rho_D^{3,\mu}\rho_D^{2,\nu}(\sigma^1)\end{aligned} \tag{B.6}$$

such that the term $\epsilon^{abc}(\rho_D^{a,\mu}\rho_D^{b,\nu} + \rho_D^{b,\mu}, \rho_D^{a,\nu})(\sigma^c)$ becomes

$$= (\rho_D^{1,\mu}\rho_D^{2,\nu} - \rho_D^{2,\mu}\rho_D^{1,\nu})\begin{pmatrix}1 & 0\\ 0 & -1\end{pmatrix} + (\rho_D^{3,\mu}\rho_D^{1,\nu} - \rho_D^{1,\mu}\rho_D^{3,\nu})\begin{pmatrix}0 & -i\\ i & 0\end{pmatrix} + (\rho_D^{2,\mu}\rho_D^{3,\nu} - \rho_D^{3,\mu}\rho_D^{2,\nu})\begin{pmatrix}0 & 1\\ 1 & 0\end{pmatrix} \tag{B.7}$$

$$= \begin{pmatrix}\rho_D^{1,\mu}\rho_D^{2,\nu} - \rho_D^{2,\mu}\rho_D^{1,\nu} & -i(\rho_D^{3,\mu}\rho_D^{1,\nu} - \rho_D^{1,\mu}\rho_D^{3,\nu}) + (\rho_D^{2,\mu}\rho_D^{3,\nu} - \rho_D^{3,\mu}\rho_D^{2,\nu}) \\ i(\rho_D^{3,\mu}\rho_D^{1,\nu} - \rho_D^{1,\mu}\rho_D^{3,\nu}) + (\rho_D^{2,\mu}\rho_D^{3,\nu} - \rho_D^{3,\mu}\rho_D^{2,\nu}) & -(\rho_D^{1,\mu}\rho_D^{2,\nu} - \rho_D^{2,\mu}\rho_D^{1,\nu}).\end{pmatrix} \tag{B.8}$$

This means that

$$Q_D\epsilon^{abc}\rho_D^{a,\mu}\rho_D^{b,\nu}(\sigma^c) = \begin{pmatrix}\rho_D^{1,\mu}\rho_D^{2,\nu} - \rho_D^{2,\mu}\rho_D^{1,\nu} & 0\\ 0 & \rho_D^{1,\mu}\rho_D^{2,\nu} - \rho_D^{2,\mu}\rho_D^{1,\nu}\end{pmatrix}, \tag{B.9}$$

$$\mathrm{Tr}(Q_D\epsilon^{abc}\rho_D^{a,\mu}\rho_D^{b,\nu}(\sigma^c)) = 2(\rho_D^{1,\mu}\rho_D^{2,\nu} - \rho_D^{2,\mu}\rho_D^{1,\nu}). \tag{B.10}$$

Using that

$$\rho_D^{\pm} = \frac{1}{\sqrt{2}}(\rho_D^1 \pm i\rho_D^2), \quad \rho_D^0 = \rho_D^3 \tag{B.11}$$

we get that

$$\rho_D^2 = \frac{i}{\sqrt{2}}(\rho_D^- - \rho_D^+), \quad \rho_D^1 = \frac{1}{\sqrt{2}}(\rho_D^+ + \rho_D^-). \tag{B.12}$$

This means that we can write

$$\begin{aligned}\rho_D^{1,\mu}\rho_D^{2,\nu} - \rho_D^{2,\mu}\rho_D^{1,\nu} &= \frac{1}{\sqrt{2}}(\rho_D^+ + \rho_D^-)\frac{i}{\sqrt{2}}(\rho_D^- - \rho_D^+) - \frac{i}{\sqrt{2}}(\rho_D^- - \rho_D^+)\frac{1}{\sqrt{2}}(\rho_D^+ + \rho_D^-) \\ &= \frac{i}{2}(\rho_D^+\rho_D^- - \rho_D^+\rho_D^+ + \rho_D^-\rho_D^- - \rho_D^-\rho_D^+) - \frac{i}{2}(\rho_D^-\rho_D^+ + \rho_D^-\rho_D^- - \rho_D^+\rho_D^+ - \rho_D^+\rho_D^-) \\ &= i(\rho_D^+\rho_D^- - \rho_D^-\rho_D^+)\end{aligned} \tag{B.13}$$

Finally, putting this into the expression, we get

$$ie_D Z'_{\mu\nu}\mathrm{Tr}(Q_D[\rho_D^\mu, \rho_D^\nu]) = ie_D Z'_{\mu\nu} 2i(\rho_D^{+\mu}\rho_D^{-\nu} - \rho_D^{-\mu}\rho_D^{+\nu}) \tag{B.14}$$

References

[1] E. Bernreuther, N. Hemme, F. Kahlhoefer, and S. Kulkarni, "Dark matter relic density in strongly interacting dark sectors with light vector mesons," *Phys. Rev. D* **110** no. 3, (2024) 035009, arXiv:2311.17157 [hep-ph].

[2] E. Bernreuther, N. Hemme, F. Kahlhoefer, S. Kulkarni, and M. Ovchynnikov, "Sub-GeV dark matter and multi-decay signatures from dark showers at beam-dump experiments," arXiv:2510.23696 [hep-ph].

[3] G. Albouy *et al.*, "Theory, phenomenology, and experimental avenues for dark showers: a Snowmass 2021 report," *Eur. Phys. J. C* **82** no. 12, (2022) 1132, arXiv:2203.09503 [hep-ph].

[4] T. A. Collaboration, "Observation of a new particle in the search for the standard model higgs boson with the atlas detector at the lhc," *Physics Letters B* **716** (Sept., 2012) 1–29. http://dx.doi.org/10.1016/j.physletb.2012.08.020.

[5] **The CMS** Collaboration, "Observation of a new boson at a mass of 125 GeV with the cms experiment at the lhc," *Physics Letters B* **716** no. 1, (Sept., 2012) 30–61. http://dx.doi.org/10.1016/j.physletb.2012.08.021.

[6] **ATLAS, CMS** Collaboration, G. Pásztor, "Precision tests of the Standard Model at the LHC with the ATLAS and CMS detectors," *PoS* **FFK2019** (2020) 005. https://cds.cern.ch/record/2713476.

[7] J. Erler and M. Schott, "Electroweak precision tests of the standard model after the discovery of the higgs boson," *Progress in Particle and Nuclear Physics* **106** (May, 2019) 68–119. http://dx.doi.org/10.1016/j.ppnp.2019.02.007.

[8] P. W. Higgs, "Broken symmetries and the masses of gauge bosons," *Phys. Rev. Lett.* **13** (Oct, 1964) 508–509. https://link.aps.org/doi/10.1103/PhysRevLett.13.508.

[9] V. A. Bednyakov, N. D. Giokaris, and A. V. Bednyakov, "On the higgs mass generation mechanism in the standard model," *Physics of Particles and Nuclei* **39** no. 1, (Jan., 2008) 13–36. http://dx.doi.org/10.1134/S1063779608010024.

[10] **Particle Data Group**, "Review of particle physics," *Phys. Rev. D* **110** no. 3, (2024) 030001.

[11] M. Maggiore, *A Modern Introduction to Quantum Field Theory*. Oxford University Press, 2005.

[12] M. Knecht, B. Moussallam, J. Sterna, and N. Fuchs, "The low energy $\pi\pi$ amplitude to one and two loops," *Nuclear Physics B* **457** no. 3, (Dec., 1995) 513–574. http://dx.doi.org/10.1016/0550-3213(95)00515-3.

[13] H. Leutwyler, "Pion physics at low energy and high accuracy," in *AIP Conference Proceedings*, vol. 602, p. 3–13. AIP, 2001. http://dx.doi.org/10.1063/1.1435906.

[14] **BNL-E865** Collaboration, S. Pislak *et al.*, "A New measurement of K+(e4) decay and the s wave pi pi scattering length a0(0)," *Phys. Rev. Lett.* **87** (2001) 221801, arXiv:hep-ex/0106071. [Erratum: Phys.Rev.Lett. 105, 019901 (2010)].

[15] J. Goldstone, A. Salam, and S. Weinberg, "Broken Symmetries," *Phys. Rev.* **127** (1962) 965–970.

[16] M. Gell-Mann, R. J. Oakes, and B. Renner, "Behavior of current divergences under SU(3) x SU(3)," *Phys. Rev.* **175** (1968) 2195–2199.

[17] A. Manohar and H. Georgi, "Chiral Quarks and the Nonrelativistic Quark Model," *Nucl. Phys. B* **234** (1984) 189–212.

[18] S. Weinberg, *The Quantum Theory of Fields. Vol. 2: Modern Applications.* Cambridge University Press, 1996.

[19] J. Wess and B. Zumino, "Consequences of anomalous Ward identities," *Phys. Lett. B* **37** no. 1, (Jan, 1971) 95–97.

[20] E. Witten, "Global Aspects of Current Algebra," *Nucl. Phys. B* **223** no. 2, (May, 1983) 422–432.

[21] Y. Hochberg, E. Kuflik, H. Murayama, T. Volansky, and J. G. Wacker, "Model for thermal relic dark matter of strongly interacting massive particles," *Physical Review Letters* **115** no. 2, (July, 2015) . http://dx.doi.org/10.1103/PhysRevLett.115.021301.

[22] N. Craig, "Naturalness: A snowmass white paper," 2022. https://arxiv.org/abs/2205.05708.

[23] K. Crowther, "Why do we want a theory of quantum gravity?," 2025. https://arxiv.org/abs/2505.04858.

[24] T. Schwetz, M. Tórtola, and J. W. F. Valle, "Global neutrino data and recent reactor fluxes: the status of three-flavour oscillation parameters," *New Journal of Physics* **13** no. 6, (June, 2011) 063004. http://dx.doi.org/10.1088/1367-2630/13/6/063004.

[25] A. D. Sakharov, "Violation of CP Invariance, C asymmetry, and baryon asymmetry of the universe," *Pisma Zh. Eksp. Teor. Fiz.* **5** (1967) 32–35.

[26] D. E. Kharzeev, E. Shuryak, and I. Zahed, "Baryogenesis and helical magnetogenesis from the electroweak transition of the minimal standard model," *Physical Review D* **97** no. 11, (June, 2020) . http://dx.doi.org/10.1103/PhysRevD.97.116009.

[27] **DESI** Collaboration, "DESI 2024 VI: cosmological constraints from the measurements of baryon acoustic oscillations," *Journal of Cosmology and Astroparticle Physics* **2025** no. 02, (Feb., 2025) 021. http://dx.doi.org/10.1088/1475-7516/2025/02/021.

[28] R. Cumming, "Därför glömde alla knut lundmarks stora upptäckt: den mörka materian - populär astronomi," 2015. https://www.popularastronomi.se/2015/06/darfor-glomde-alla-knut-lundmarks-stora-upptackt-den-morka-materian/.

[29] F. Zwicky, "Die Rotverschiebung von extragalaktischen Nebeln," *Helv. Phys. Acta* **6** (1933) 110–127. https://ui.adsabs.harvard.edu/abs/1933AcHPh...6..110Z/abstract.

[30] A. H. G. Peter, "Dark matter: A brief review," 2012. https://arxiv.org/abs/1201.3942.

[31] M. Cirelli, A. Strumia, and J. Zupan, "Dark matter," 2024. https://arxiv.org/abs/2406.01705.

[32] C. Balazs, T. Bringmann, F. Kahlhoefer, and M. White, "A primer on dark matter," 2024. https://arxiv.org/abs/2411.05062.

[33] **NASA / LAMBDA Science Team**, "LAMBDA: Legacy Archive for Microwave Background Data Analysis," 2025. https://lambda.gsfc.nasa.gov. Accessed 2025-09-10.

[34] V. C. Rubin and W. K. Ford, "Rotation of the andromeda nebula from a spectroscopic survey of emission regions," *Astrophysical Journal* **159** (1970) 379–403.

[35] J. Wambsganss, "Gravitational Lensing in Astronomy," *Living Rev. Relativ.* **1** (1998) 12.

[36] ESA/Hubble and NASA, "Close-up of the Einstein ring around galaxy NGC 6505," 2025. https://www.esa.int/ESA_Multimedia/Images/2025/02/Close-up_of_the_Einstein_ring_around_galaxy_NGC_6505. Accessed 2025-09-09.

[37] NASA/CXC/M.Markevitch and others, "Bullet Cluster Composite Image," 2006. https://chandra.harvard.edu/photo/2006/1e0657/. Accessed 2025-09-09.

[38] D. Gilman, X. Du, A. Benson, S. Birrer, A. Nierenberg, and T. Treu, "Constraints on the mass–concentration relation of cold dark matter haloes with 11 strong gravitational lenses," *Monthly Notices of the Royal Astronomical Society: Letters* **492** no. 1, (Oct., 2019) L12–L16. http://dx.doi.org/10.1093/mnrasl/slz173.

[39] H. Hoekstra, H. Yee, and M. D. Gladders, "Current status of weak gravitational lensing," *New Astronomy Reviews* **46** no. 12, (Dec., 2002) 767–781. http://dx.doi.org/10.1016/S1387-6473(02)00245-2.

[40] D. Harvey, R. Massey, T. Kitching, A. Taylor, and E. Tittley, "The nongravitational interactions of dark matter in colliding galaxy clusters," *Science* **347** no. 6229, (Mar., 2015) 1462–1465. http://dx.doi.org/10.1126/science.1261381.

[41] E. Hubble, "A Relation between Distance and Radial Velocity among Extra-Galactic Nebulae," *Proceedings of the National Academy of Science* **15** no. 3, (Mar., 1929) 168–173.

[42] L. Verde, T. Treu, and A. G. Riess, "Tensions between the early and late universe," *Nature Astronomy* **3** no. 10, (Sept., 2019) 891–895. http://dx.doi.org/10.1038/s41550-019-0902-0.

[43] E. Abdalla *et al.*, "Cosmology intertwined: A review of the particle physics, astrophysics, and cosmology associated with the cosmological tensions and anomalies," *Journal of High Energy Astrophysics* **34** (June, 2022) 49–211. http://dx.doi.org/10.1016/j.jheap.2022.04.002.

[44] **Planck** Collaboration, "Planck2015 results: XX. constraints on inflation," *Astronomy & Astrophysics* **594** (Sept., 2016) A20. http://dx.doi.org/10.1051/0004-6361/201525898.

[45] **Planck** Collaboration, "Planck2018 results: VI. cosmological parameters," *Astronomy & Astrophysics* **641** (Sept., 2020) A6. http://dx.doi.org/10.1051/0004-6361/201833910.

[46] T. Tröster, A. G. Sánchez, M. Asgari, C. Blake, M. Crocce, C. Heymans, H. Hildebrandt, B. Joachimi, S. Joudaki, A. Kannawadi, C.-A. Lin, and A. Wright, "Cosmology from large-scale structure - constraining ΛCDM with BOSS," *Astronomy & Astrophysics* **633** (Feb., 2020) L10. http://dx.doi.org/10.1051/0004-6361/201936772.

[47] J. S. Bullock and M. Boylan-Kolchin, "Small-scale challenges to the ΛCDM paradigm," *Annual Review of Astronomy and Astrophysics* **55** no. 1, (Aug., 2017) 343–387. http://dx.doi.org/10.1146/annurev-astro-091916-055313.

[48] A. Robertson, R. Massey, and V. Eke, "What does the bullet cluster tell us about self-interacting dark matter?," *Monthly Notices of the Royal Astronomical Society* **465** no. 1, (Oct., 2016) 569–587. http://dx.doi.org/10.1093/mnras/stw2670.

[49] D. Wittman, N. Golovich, and W. A. Dawson, "The mismeasure of mergers: Revised limits on self-interacting dark matter in merging galaxy clusters," *The Astrophysical Journal* **869** no. 2, (Dec., 2018) 104. http://dx.doi.org/10.3847/1538-4357/aaee77.

[50] P. Gondolo and G. Gelmini, "Cosmic abundances of stable particles: Improved analysis," *Nucl. Phys. B* **360** no. 1, (May, 1991) 145–179.

[51] T. Bringmann and J. Edsjö, "Darksusy 6.3: Freeze-in, out-of-equilibrium freeze-out, cosmic-ray upscattering and further new features," 2022. https://arxiv.org/abs/2203.07439.

[52] M. Drees, F. Hajkarim, and E. R. Schmitz, "The effects of QCD equation of state on the relic density of WIMP dark matter," *Journal of Cosmology and Astroparticle Physics* **2015** no. 06, (Jun, 2015) 025–025. https://doi.org/10.1088%2F1475-7516%2F2015%2F06%2F025.

[53] G. Arcadi, M. Dutra, P. Ghosh, M. Lindner, Y. Mambrini, M. Pierre, S. Profumo, and F. S. Queiroz, "The waning of the WIMP? a review of models, searches, and constraints," *The European Physical Journal C* **78** no. 3, (Mar., 2018) . http://dx.doi.org/10.1140/epjc/s10052-018-5662-y.

[54] M. J. Strassler and K. M. Zurek, "Echoes of a hidden valley at hadron colliders," *Physics Letters B* **651** no. 5–6, (Aug., 2007) 374–379. http://dx.doi.org/10.1016/j.physletb.2007.06.055.

[55] Y. Hochberg, E. Kuflik, T. Volansky, and J. G. Wacker, "Mechanism for thermal relic dark matter of strongly interacting massive particles," *Physical Review Letters* **113** no. 17, (Oct., 2014) . http://dx.doi.org/10.1103/PhysRevLett.113.171301.

[56] A. Kamada, S. Kobayashi, and T. Kuwahara, "Perturbative unitarity of strongly interacting massive particle models," *Journal of High Energy Physics* **2023** no. 2, (Feb., 2023) . http://dx.doi.org/10.1007/JHEP02(2023)217.

[57] M. A. Buen-Abad, R. Emami, and M. Schmaltz, "Cannibal dark matter and large scale structure," *Physical Review D* **98** no. 8, (Oct., 2018) . http://dx.doi.org/10.1103/PhysRevD.98.083517.

[58] J. Smirnov and J. F. Beacom, "New freezeout mechanism for strongly interacting dark matter," *Physical Review Letters* **125** no. 13, (Sept., 2020) . http://dx.doi.org/10.1103/PhysRevLett.125.131301.

[59] P. Braat and M. Postma, "Simply add a dark photon," *Journal of High Energy Physics* **2023** no. 3, (Mar., 2023) . http://dx.doi.org/10.1007/JHEP03(2023)216.

[60] B. Sadoulet, "Forty years of dark matter searches," *Nuclear Physics B* **1003** (Aug., 2024) 116509. http://dx.doi.org/10.1016/j.nuclphysb.2024.116509.

[61] **LUX-ZEPLIN** Collaboration, "First dark matter search results from the lux-zeplin (lz) experiment," *Physical Review Letters* **131** no. 4, (July, 2023) . http://dx.doi.org/10.1103/PhysRevLett.131.041002.

[62] **XENON** Collaboration, "Constraining the spin-dependent wimp-nucleon cross sections with XENON1T," *Physical Review Letters* **122** no. 14, (Apr., 2019) . http://dx.doi.org/10.1103/PhysRevLett.122.141301.

[63] **PandaX** Collaboration, "Search for light dark matter from the atmosphere in PandaX-4T," *Physical Review Letters* **131** no. 4, (July, 2023) . http://dx.doi.org/10.1103/PhysRevLett.131.041001.

[64] **XENON** Collaboration, "First indication of solar ^{8}B neutrinos via coherent elastic neutrino-nucleus scattering with XENONnT," *Physical Review Letters* **133** no. 19, (Nov., 2024) . http://dx.doi.org/10.1103/PhysRevLett.133.191002.

[65] **PandaX** Collaboration, "First indication of solar ^{8}B neutrino flux through coherent elastic neutrino-nucleus scattering in PandaX-4T," 2024. https://arxiv.org/abs/2407.10892.

[66] R. Bernabei, B, *et al.*, "The DAMA project: Achievements, implications and perspectives," *Progress in Particle and Nuclear Physics* **114** (Dec., 2020) 103810. http://dx.doi.org/10.1016/j.ppnp.2020.103810.

[67] M. Misiaszek and N. Rossi, "Direct detection of dark matter: A critical review," *Symmetry* **16** no. 2, (Feb., 2024) 201. http://dx.doi.org/10.3390/sym16020201.

[68] G. Adhikari, , *et al.*, "Strong constraints from cosine-100 on the dama dark matter results using the same sodium iodide target," *Science Advances* **7** no. 46, (2021) eabk2699, https://www.science.org/doi/pdf/10.1126/sciadv.abk2699. https://www.science.org/doi/abs/10.1126/sciadv.abk2699.

[69] E. Barberio, R. Bernabei, P. Belli, F. Cappella, R. Cerulli, C. Dai, A. d'Angelo, A. Di Marco, A. Incicchitti, X. Ma, A. Mattei, V. Merlo, F. Montecchia, X. Sheng, and Z. Ye, "The sabre experiment,". https://doi.org/10.1088/1748-0221/20/04/T04001.

[70] **AMS** Collaboration, "Antiproton Flux, Antiproton-to-Proton Flux Ratio, and Properties of Elementary Particle Fluxes in Primary Cosmic Rays Measured with the Alpha Magnetic Spectrometer on the International Space Station," *Phys. Rev. Lett.* **117** no. 9, (Aug, 2016) 091103.

[71] J. Heisig, M. Korsmeier, and M. W. Winkler, "Revisiting the AMS-02 antiproton excess: The role of correlated errors," 2021. https://arxiv.org/abs/2107.14606.

[72] T. F. L. collaboration, "Limits on dark matter annihilation signals from the Fermi LAT 4-year measurement of the isotropic gamma-ray background," *Journal of Cosmology and Astroparticle Physics* **2015** no. 09, (Sept., 2015) 008–008. http://dx.doi.org/10.1088/1475-7516/2015/09/008.

[73] **ATLAS** Collaboration, "Dark matter summary plots for s-channel mediators,".

[74] **CMS** Collaboration, "CMS Exotica Summary Plots," 2024. https://twiki.cern.ch/twiki/bin/view/CMSPublic/SummaryPlotsEXO13TeV?sortcol=1;table=19;up=0#sorted_table.

[75] **The ALEPH, DELPHI, L3, OPAL, SLD Collaborations, LEP Electroweak Working Group, SLD Electroweak, Heavy Flavour Groups** Collaboration, "Precision electroweak measurements on the z resonance," *Physics Reports* **427** no. 5-6, (Feb., 2006) 257–454. http://dx.doi.org/10.1016/j.physrep.2005.12.006.

[76] **Belle-II** Collaboration, J. Kahn, "The Belle II Experiment," in *CERN-BINP Workshop for Young Scientists in e+e- Colliders*, pp. 45–54. 2017.

[77] **Belle II** Collaboration, L. Aggarwal, , *et al.*, "Snowmass white paper: Belle II physics reach and plans for the next decade and beyond," 2022. https://arxiv.org/abs/2207.06307.

[78] Y. M. Andreev *et al.*, "Search for light dark matter with NA64 at CERN," 2023. https://arxiv.org/abs/2307.02404.

[79] **SHiP** Collaboration, "SHiP experiment at the SPS Beam Dump Facility,". https://arxiv.org/abs/2504.06692.

[80] J. J. Sakurai, *Currents and Mesons*. The University of Chicago Press, 1969.

[81] Riazuddin and Fayyazuddin, "Algebra of current components and decay widths of ρ and K^* mesons," *Phys. Rev.* **147** (Jul, 1966) 1071–1073. https://link.aps.org/doi/10.1103/PhysRev.147.1071.

[82] S. Li, J. M. Yang, M. Zhang, Y. Zhang, and R. Zhu, "Can a secluded self-interacting dark sector generate detectable gravitational waves?," 2025. https://arxiv.org/abs/2502.04108.

[83] T. G. Rizzo, "Kinetic mixing and portal matter phenomenology," *Phys. Rev. D* **99** no. 1, (2019) 015037, arXiv:1902.11246 [hep-ph].

[84] E. Stueckelberg, "Die Wechselwirkungskräfte in der Elektrodynamik und in der Feldtheorie der Kernkräfte," *Helv. Phys. Acta* **11** (1938) 299–328.

[85] B. Holdom, "Two U(1)'s and ϵ charge shifts," *Phys. Lett. B* **166** no. 2, (May, 1986) 196–198.

[86] E. Bernreuther, K. Böse, T. Ferber, C. Hearty, F. Kahlhoefer, A. Morandini, and K. Schmidt-Hoberg, "Forecasting dark showers at Belle II," *JHEP* **12** (2022) 005, arXiv:2203.08824 [hep-ph].

[87] A. Berlin, N. Blinov, S. Gori, P. Schuster, and N. Toro, "Cosmology and accelerator tests of strongly interacting dark matter," *Physical Review D* **97** no. 5, (Mar., 2018) . http://dx.doi.org/10.1103/PhysRevD.97.055033.

[88] E. Bernreuther, F. Kahlhoefer, M. Krämer, and P. Tunney, "Strongly interacting dark sectors in the early universe and at the LHC through a simplified portal," *Journal of High Energy Physics* **2020** no. 1, (Jan., 2020) . http://dx.doi.org/10.1007/JHEP01(2020)162.

[89] P. Maris and P. Tandy, "QCD modeling of hadron physics," *Nuclear Physics B - Proceedings Supplements* **161** (Nov., 2006) 136–152. http://dx.doi.org/10.1016/j.nuclphysbps.2006.08.012.

[90] M. Hansen, K. Langæble, and F. Sannino, "SIMP model at NNLO in chiral perturbation theory," *Phys. Rev. D* **92** (Oct, 2015) 075036. https://link.aps.org/doi/10.1103/PhysRevD.92.075036.

[91] M. Faber and R. Höllwieser, "Chiral symmetry breaking on the lattice," *Progress in Particle and Nuclear Physics* **97** (Nov., 2017) 312–355. http://dx.doi.org/10.1016/j.ppnp.2017.08.001.

[92] C. S. Fischer, "Infrared properties of QCD from Dyson–Schwinger equations," *Journal of Physics G: Nuclear and Particle Physics* **32** no. 8, (June, 2006) R253–R291. http://dx.doi.org/10.1088/0954-3899/32/8/R02.

[93] H. Kolešová, D. Krichevskiy, and S. Kulkarni, "NLO observables for QCD-like theories and application to pion dark matter," 2025. https://arxiv.org/abs/2509.07102.

[94] S. K. Acharya and R. Khatri, "CMB anisotropy and BBN constraints on pre-recombination decay of dark matter to visible particles," *Journal of Cosmology and Astroparticle Physics* **2019** no. 12, (Dec., 2019) 046–046. http://dx.doi.org/10.1088/1475-7516/2019/12/046.

[95] M. Kawasaki, K. Kohri, T. Moroi, and Y. Takaesu, "Revisiting big-bang nucleosynthesis constraints on long-lived decaying particles," *Phys. Rev. D* **97** (Jan, 2018) 023502. https://link.aps.org/doi/10.1103/PhysRevD.97.023502.

[96] C. Xu, W. Qin, and T. R. Slatyer, "CMB limits on decaying dark matter beyond the ionization threshold," 2024. https://arxiv.org/abs/2408.13305.

[97] F. Zierler, S. Kulkarni, A. Maas, S. Mee, M. Nikolic, and J. Pradler, "Strongly interacting dark matter from Sp(4) gauge theory," *EPJ Web of Conferences* **274** (2022) 08014. http://dx.doi.org/10.1051/epjconf/202227408014.

[98] N. A. Dondi, F. Sannino, and J. Smirnov, "Thermal history of composite dark matter," *Physical Review D* **101** no. 10, (May, 2020) . http://dx.doi.org/10.1103/PhysRevD.101.103010.

[99] T. Cohen, M. Lisanti, and H. K. Lou, "Semivisible jets: Dark matter undercover at the lhc," *Physical Review Letters* **115** no. 17, (Oct., 2015) . http://dx.doi.org/10.1103/PhysRevLett.115.171804.

[100] C. Bierlich, S. Chakraborty, N. Desai, L. Gellersen, I. Helenius, P. Ilten, L. Lönnblad, S. Mrenna, S. Prestel, C. T. Preuss, T. Sjöstrand, P. Skands, M. Utheim, and R. Verheyen, "A comprehensive guide to the physics and usage of PYTHIA 8.3," 2022. https://arxiv.org/abs/2203.11601.

[101] J. Alwall, R. Frederix, S. Frixione, V. Hirschi, F. Maltoni, O. Mattelaer, H.-S. Shao, T. Stelzer, P. Torrielli, and M. Zaro, "The automated computation of tree-level and next-to-leading order differential cross sections, and their matching to parton shower simulations," *Journal of High Energy Physics* **2014** no. 7, (July, 2014) . http://dx.doi.org/10.1007/JHEP07(2014)079.

[102] C. Degrande, C. Duhr, B. Fuks, D. Grellscheid, O. Mattelaer, and T. Reiter, "UFO – the Universal FeynRules Output," *Computer Physics Communications* **183** no. 6, (June, 2012) 1201–1214. http://dx.doi.org/10.1016/j.cpc.2012.01.022.

[103] W. Liu, J. Lockyer, and S. Kulkarni, "Hidden valleys in the CMS muon endcap detector," 2025. https://arxiv.org/abs/2505.03058.

[104] R. Mertig, M. Böhm, and A. Denner, "Feyn Calc - Computer-algebraic calculation of Feynman amplitudes," *Comput. Phys. Commun.* **64** no. 3, (Mar, 1991) 345–359.

[105] V. Shtabovenko, R. Mertig, and F. Orellana, "New developments in FeynCalc 9.0," *Computer Physics Communications* **207** (Oct., 2016) 432–444. http://dx.doi.org/10.1016/j.cpc.2016.06.008.

[106] V. Shtabovenko, R. Mertig, and F. Orellana, "FeynCalc 9.3: New features and improvements," *Comput. Phys. Commun.* **256** (2020) 107478, arXiv:2001.04407 [hep-ph].

[107] P. Virtanen *et al.*, "SciPy 1.0: Fundamental Algorithms for Scientific Computing in Python," *Nature Methods* **17** (2020) 261–272.

[108] J. Edsjö and P. Gondolo, "Neutralino relic density including coannihilations," *Physical Review D* **56** no. 4, (Aug., 1997) 1879–1894. http://dx.doi.org/10.1103/PhysRevD.56.1879.

[109] M. Ovchynnikov, J.-L. Tastet, O. Mikulenko, and K. Bondarenko, "Sensitivities to feebly interacting particles: Public and unified calculations," *Physical Review D* **108** no. 7, (Oct., 2023) . http://dx.doi.org/10.1103/PhysRevD.108.075028.

[110] M. Ovchynnikov and Y. Kyselov, "Searches for long-lived dark photons at proton accelerator experiments," 2024. https://arxiv.org/abs/2409.11096.

[111] **SHiP** Collaboration, "BDF/SHiP at the ECN3 high-intensity beam facility," tech. rep., CERN, Geneva, 2023. https://cds.cern.ch/record/2878604.

[112] **SHiP** Collaboration, "SHiP progress report 2024,". https://cds.cern.ch/record/2917226.

[113] **SHiP** Collaboration, "Neutrino physics with the SHiP experiment at CERN," *Journal of Physics: Conference Series* **1690** no. 1, (1, 2019) 012171. https://doi.org/10.1088/1742-6596/1690/1/012171.

[114] **NA62** Collaboration, E. C. Gil *et al.*, "The beam and detector of the NA62 experiment at cern," *Journal of Instrumentation* **12** no. 05, (May, 2017) . http://dx.doi.org/10.1088/1748-0221/12/05/P05025.

[115] **NA62** Collaboration, J. Jerhot, "Projection of finalized NA62 beam-dump analyses to the full 2021-2026 statistics," tech. rep., CERN, Geneva, 2025. https://cds.cern.ch/record/2936260.

[116] **NA62** Collaboration, E. C. Gil *et al.*, "Search for dark photon decays to $\mu^+\mu^-$ at NA62," *Journal of High Energy Physics* **2023** no. 9, (Sept., 2023) . http://dx.doi.org/10.1007/JHEP09(2023)035.

[117] **Belle II** Collaboration, J. Kahn, "The Belle II experiment," 2017. https://e-publishing.cern.ch/index.php/CP/article/view/377.

[118] **Belle II** Collaboration, "Search for a dark photon and an invisible dark higgs boson in $\mu^+\mu^-$ and missing energy final states with the belle ii experiment," *Physical Review Letters* **130** no. 7, (Feb., 2023) .

[119] Christian Bierlich and others, "Pythia 8.3 Update History," 2025. https://pythia.org/history/. Accessed 2025-08-20.

[120] A. Buckley, J. Ferrando, S. Lloyd, K. Nordström, B. Page, M. Rüfenacht, M. Schönherr, and G. Watt, "LHAPDF6: parton density access in the LHC precision era," *The European Physical Journal C* **75** no. 3, (Mar., 2015) . http://dx.doi.org/10.1140/epjc/s10052-015-3318-8.

[121] M. Ovchynnikov and A. Zaporozhchenko, "Advancing the phenomenology of GeV-scale axionlike particles," *Phys. Rev. D* **112** no. 1, (2025) 015001, arXiv:2501.04525 [hep-ph].

[122] Y. Kyselov, S. Mrenna, and M. Ovchynnikov, "New physics particles mixing with mesons: production in the fragmentation chain," arXiv:2504.06828 [hep-ph].

[123] G. D. V. Garcia and M. Ovchynnikov, "Di-decay signature of new physics particles at intensity frontier experiments," 2025. https://arxiv.org/abs/2503.01760.

[124] M. Duerr, T. Ferber, C. Garcia-Cely, J. Heisig, F. Kahlhoefer, K. Schmidt-Hoberg, T. Schwetz, P. Stengel, and M. W. Winkler, "Long-lived dark higgs and inelastic dark matter at Belle II," *Journal of High Energy Physics* **2021** no. 4, (Apr., 2021) . http://dx.doi.org/10.1007/jhep04(2021)146.

[125] **BEBC** Collaboration, A. Cooper-Sarkar *et al.*, "Search for heavy neutrino decays in the BEBC beam dump experiment," *Physics Letters B* **160** no. 1-3, (Nov., 1985) 207–211. http://dx.doi.org/10.1016/0370-2693(85)91493-5.

[126] **BEBC** Collaboration, H. Grässler *et al.*, "Prompt neutrino production in 400 GeV proton copper interactions," *Nuclear Physics B* **273** no. 2, (Jan., 1986) . http://dx.doi.org/10.1016/0550-3213(86)90246-4.

[127] **CHARM** Collaboration, F. Bergsma *et al.*, "A search for decays of heavy neutrinos," *Physics Letters B* **128** no. 5, (Nov., 1983) 361–366. http://dx.doi.org/10.1016/0370-2693(83)90275-7.

[128] **CHARM** Collaboration, F. Bergsma *et al.*, "Search for axion-like particle production in 400 GeV proton-copper interactions," *Physics Letters B* **157** no. 5-6, (Nov., 1985) 458–462. http://dx.doi.org/10.1016/0370-2693(85)90400-9.

[129] **CMS** Collaboration, "Search for resonant production of strongly coupled dark matter in proton-proton collisions at 13 TeV," *Journal of High Energy Physics* **2022** no. 6, (June, 2022) . http://dx.doi.org/10.1007/JHEP06(2022)156.

[130] E. Conte, B. Fuks, and G. Serret, "MadAnalysis 5, a user-friendly framework for collider phenomenology," *Computer Physics Communications* **184** no. 1, (Jan., 2013) 222–256. http://dx.doi.org/10.1016/j.cpc.2012.09.009.

[131] E. Conte and B. Fuks, "Confronting new physics theories to LHC data with MADANALYSIS 5," *International Journal of Modern Physics A* **33** no. 28, (Oct., 2018) 1830027. http://dx.doi.org/10.1142/S0217751X18300272.

[132] S. Kraml, "Interpreting LHC results," 2025. https://twiki.cern.ch/twiki/bin/view/LHCPhysics/InterpretingLHCresults. Accessed: 2025-08-19.

[133] J. de Favereau, C. Delaere, P. Demin, A. Giammanco, V. Lemaître, A. Mertens, and M. Selvaggi, "Delphes 3: a modular framework for fast simulation of a generic collider experiment," *Journal of High Energy Physics* **2014** no. 2, (Feb., 2014) . http://dx.doi.org/10.1007/JHEP02(2014)057.

[134] **ATLAS** Collaboration, "Search for non-resonant production of semi-visible jets using Run 2 data in ATLAS," *Physics Letters B* **848** (Jan., 2024) 138324. http://dx.doi.org/10.1016/j.physletb.2023.138324.

[135] M. Creutz, "One flavor qcd," *Annals of Physics* **322** no. 7, (July, 2007) 1518–1540. http://dx.doi.org/10.1016/j.aop.2007.01.002.

[136] S. Agostinelli *et al.*, "GEANT4: A Simulation toolkit," *Nucl. Instrum. Meth. A* **506** no. 3, (Jul, 2003) 250–303.

[137] **ATLAS** Collaboration, "Search for resonant production of dark quarks in the dijet final state with the atlas detector," *Journal of High Energy Physics* **2024** no. 2, (Feb., 2024) . http://dx.doi.org/10.1007/JHEP02(2024)128.

[138] M. Park and M. Zhang, "Tagging a jet from a dark sector with jet substructures at colliders," *Physical Review D* **100** no. 11, (Dec., 2019) . http://dx.doi.org/10.1103/PhysRevD.100.115009.

[139] **ATLAS** Collaboration, "Search for new resonances in mass distributions of jet pairs using 139 fb^{-1} of pp collisions at $\sqrt{s}$ 13 TeV with the ATLAS detector," *Journal of High Energy Physics* **2020** no. 3, (Mar., 2020) . http://dx.doi.org/10.1007/JHEP03(2020)145.

[140] G. Choudalakis, "On hypothesis testing, trials factor, hypertests and the BumpHunter," 2011. https://arxiv.org/abs/1101.0390.

[141] **CDF Collaboration** Collaboration, "Global search for new physics with 2.0/fb at CDF," *Physical Review D* **79** no. 1, (Jan., 2009) . http://dx.doi.org/10.1103/PhysRevD.79.011101.

[142] **CMS Collaboration** Collaboration, "Search for new particles in events with energetic jets and large missing transverse momentum in proton-proton collisions at $\sqrt{s} = 13$ TeV," *Journal of High Energy Physics* **2021** no. 11, (Nov., 2021) . http://dx.doi.org/10.1007/JHEP11(2021)153.

[143] B. Fuks, D. Sengupta, M. Goodsell, *et al.*, "Madanalysis 5 dataverse," 2025. https://dataverse.uclouvain.be/dataverse/madanalysis. Accessed: 2025-08-20.

[144] T. Wojtkowski and S. Sinha, "Implementation of a search for semi-visible jet production (139/fb; ATLAS-EXOT-2022-37)," 2024. https://doi.org/10.14428/DVN/AFYF5Y.

[145] T. Wojtkowski, "Implementation of a search for new dijet resonances (139 fb-1; ATLAS-EXOT-2019-03)," 2023. https://doi.org/10.14428/DVN/KHJ1MW.

[146] A. Albert, "Implementation of a search for new phenomena in events featuring energetic jets and missing transverse energy (137 fb-1; 13 TeV; CMS-EXO-20-004)," 2021. https://doi.org/10.14428/DVN/IRF7ZL.

[147] R. Pasechnik, M. Reichert, F. Sannino, and Z.-W. Wang, "Gravitational waves from composite dark sectors," 2023. https://arxiv.org/abs/2309.16755.

[148] A. Belyaev, M. Bertenstam, J. Gonçalves, A. P. Morais, R. Pasechnik, and N. Thongyoi, "Gravitational waves from dark gauge sectors," 2025. https://arxiv.org/abs/2508.04912.